

**T.R.
SAKARYA UNIVERSITY
GRADUATE SCHOOL OF NATURAL AND APPLIED SCIENCES**

**COMPUTATIONAL INVESTIGATION OF BATTERY
MATERIALS USING DENSITY FUNCTIONAL THEORY**

PhD THESIS

Doaa Aasef Ahmed AHMED

Nanoscience and Nanoengineering Department

NOVEMBER 2023

**T.R.
SAKARYA UNIVERSITY
GRADUATE SCHOOL OF NATURAL AND APPLIED SCIENCES**

**COMPUTATIONAL INVESTIGATION OF BATTERY
MATERIALS USING DENSITY FUNCTIONAL THEORY**

PhD THESIS

Doaa Aasef Ahmed AHMED

Nanoscience and Nanoengineering Department

Thesis Advisor: Assoc. Prof. Dr. Tuğrul ÇETİNKAYA

NOVEMBER 2023

The thesis work titled “Doaa Aasef Ahmed Ahmed” prepared by COMPUTATIONAL INVESTIGATION OF BATTERY MATERIALS USING DENSITY FUNCTIONAL THEORY was accepted by the following jury on 17/11/2023 by unanimously/majority of votes as a PhD THESIS in Sakarya University Institute of Natural Sciences, Nanoscience and Nanoengineering department.

Thesis Jury

Head of Jury :

Jury Member :

Jury Member :

Jury Member :

Jury Member :

STATEMENT OF COMPLIANCE WITH THE ETHICAL PRINCIPLES AND RULES

I declare that the thesis work titled " COMPUTATIONAL INVESTIGATION OF BATTERY MATERIALS USING DENSITY FUNCTIONAL THEORY", which I have prepared in accordance with Sakarya University Graduate School of Natural and Applied Sciences regulations and Higher Education Institutions Scientific Research and Publication Ethics Directive, belongs to me, is an original work, I have acted in accordance with the regulations and directives mentioned above at all stages of my study, I did not get the innovations and results contained in the thesis from anywhere else, I duly cited the references for the works I used in my thesis, I did not submit this thesis to another scientific committee for academic purposes and to obtain a title, in accordance with the articles 9/2 and 22/2 of the Sakarya University Graduate Education and Training Regulation published in the Official Gazette dated 20.04.2016, a report was received in accordance with the criteria determined by the graduate school using the plagiarism software program to which Sakarya University is a subscriber, I accept all kinds of legal responsibility that may arise in case of a situation contrary to this statement.

17.11.2023

Doaa Aasef Ahmed Ahmed

To my family

ACKNOWLEDGMENTS

First and foremost, I express my gratitude to God for bestowing upon me the strength, perseverance, and guidance that enabled me to navigate the challenges of this scholarly pursuit.

I am extremely grateful to my supervisor Assoc. Prof. Dr. Tuğrul ÇETİNKAYA for steering me towards the intriguing research topic that forms the crux of this thesis.

My deep appreciation extends to Dr. Abdulkadir KIZILASLAN, for his generosity in sharing his vast knowledge, providing valuable guidance, and offering constructive feedback has played a pivotal role in refining my research.

My gratitude to Dr. Gregor VONBUN-FELDBAUER and Dr. Wernfried MAYR-SCHMOLZER whose insights and expertise in the field have enriched the perspectives presented within this work.

My gratitude extends to my first teachers, my mother Intisar mahmood and my father Asif AHMED, who instilled in me a love for learning and provided unwavering support throughout my academic journey. Your belief in me has been a constant source of motivation.

I express heartfelt thanks to my amazing siblings, Sally, Mohammed, and Omer AHMED for their support, encouragement, and motivation.

Furthermore, my big thanks to my colleague and friend, Mustafa ÇELİK, who deserves special mention for their unwavering assistance, especially in navigating the complexities of online procedures.

I am deeply grateful for the unwavering companionship and support of my dear friends, Shahad LUAY and Sarah ATHEER, throughout this endeavour, standing by me steadfastly through all circumstances.

Appreciate the chance to meet smart people in SARGEM lab whose collaborative spirit and shared passion for research created an inspiring atmosphere.

Doaa Aasef Ahmed Ahmed

TABLE OF CONTENTS

	<u>Page</u>
ACKNOWLEDGMENTS	ix
TABLE OF CONTENTS	xi
ABBREVIATIONS	xiii
LIST OF TABLES	xv
LIST OF FIGURES	xvii
SUMMARY	xix
ÖZET	xxiii
1. INTRODUCTION	1
1.1. Next Generation of Rechargeable Batteries	2
1.1.1. All solid state battery	3
1.1.1.1. Solid electrolyte	4
1.1.2. Li-O ₂ battery	5
1.1.2.1. Cathode materials.....	5
1.2. Using Density Functional Theory as a Tool to Investigate Battery Materials ..	7
2. METHOD	9
2.1. Density Functional Theory	9
2.1.1. Exchange-correlation approximations in DFT.....	11
2.1.1.1. Local density approximation (LDA).....	11
2.1.1.2. Generalized gradient approximation (GGA).....	11
2.1.2. Plane wave	12
2.1.3. Brillouin zone.....	13
2.1.4. Irreducible Brillouin zone (IBZ)	16
2.1.5. . K-points.....	17
2.1.5.1. Monkhorst–Pack method	18
2.1.5.2. Γ -point method.....	18
2.1.6. DFT+U method	19
2.2. Computational Surface Science	20
2.2.1. Surface energy.....	20
2.2.2. Surface reactivity	21
2.2.3. First principles thermodynamics	21
2.2.4. Nudged elastic band method (NEB)	22
2.2.5. Ionic diffusion prediction.....	25
2.2.6. The slab creation	26
2.2.7. Surface termination	27
2.2.7.1. Symmetric and stoichiometric termination	27
2.2.7.2. Symmetric and non-stoichiometric termination.....	29
2.2.7.3. Asymmetric and non-stoichiometric termination.....	30
2.3. Computational Details	32
2.3.1. LATP.....	32
2.3.2. TiMn ₂	32
2.3.3. MnO ₂	33

3. RESULT AND SUGGESTIONS.....	35
3.1. LiAlTi(PO ₃) ₄ as a Solid Electrolyte	35
3.1.1. Structure stability	35
3.1.2. Lithium-ion migration profile for bare LATP	41
3.1.3. Lithium-ion migration profile for sulfur doped LATP.....	42
3.1.4. Polyhedral volume analysis.....	45
3.1.5. Electronic state analysis	48
3.2. TiMn ₂ as a Carbon Free Cathode for Li-O ₂ Battery	52
3.2.1. Bulk and electronic properties.....	52
3.2.2. Surface stability of TiMn ₂	54
3.2.3. ORR/OER mechanism	56
3.3. MnO ₂ -(211) as a Carbon Free Cathode for Li-O ₂ Battery	61
3.3.1. Using DFT+U to predict the bulk properties and band gap	61
3.3.2. Surface stability of MnO ₂	64
3.3.3. The effect of DFT+U on adsorption properties.....	66
4. CONCLUSIONS.....	71
4.1. LiAlTi(PO ₃) ₄	71
4.2. TiMn ₂	71
4.3. MnO ₂	72
REFERENCES	73
CURRICULUM VITAE	83

ABBREVIATIONS

LIBs	: Lithium-ion batteries
LABs	: Lithium-Air batteries
ASSBs	: All-solid-state batteries
DFT	: Density functional theory
ORR	: Oxygen reduction reaction
OER	: Oxygen evolution reaction
NASICON	: Sodium superionic conductor
XC	: Exchange-correlation functional
LDA	: Local density approximation
GGA	: Generalized gradient approximation
U	: Hubbard term
SCAN	: Strongly constrained and appropriately normed
LTP	: $\text{Li}_{1+x}\text{Ti}_{2-x}\text{Al}_x(\text{PO}_4)_3$
BZ	: Brillouin zone
IBZ	: Irreducible Brillouin zone
NEB	: Nudged elastic band method
DOS	: Density of states
PDOS	: Partial density of states
VB	: Valence band
CB	: Conduction band
U_{eq}	: Equilibrium potential
UDC	: Discharge voltage
UC	: Charge voltage
η_{ORR}	: Overpotential of oxygen reduction reaction
η_{OER}	: Overpotential of oxygen evolution reaction

LIST OF TABLES

	<u>Page</u>
Table 3.1. Lattice constants (a, b and c), volume (V), and the total energy (E_{tot}) for bare and sulfur doped LATP unit cell.	38
Table 3.2. Comparing the bond length (in Å) in the first and second regions between LATP (S0) and Sulfur doped LATP (S1, S2, S3, and S4).	39
Table 3.3. Bader charge values for bare LATP (S0) and S@LATP for the first region.	50
Table 3.4. The adsorption energies of the O and Li atoms on TiMn_2 (0 0 1)-D4 surface at (eV).	57
Table 3.5. Comparison of theoretical ORR overpotential (η_{ORR}) and OER overpotential (η_{OER}) in our study with previous works.	60
Table 3.6. The band gap value (in eV) and the lattice constants (a, b and c) for α - MnO_2 bulk structure with three different DFT-based methods GGA+U, SCAN, and SCAN+U	63
Table 3.7. The adsorption energies of the O and Li atoms on MnO_2 (211)-Mn surface termination at (eV)	66

LIST OF FIGURES

	<u>Page</u>
Figure 2.1. (a) Reciprocal lattice points near the point O at the origin of the reciprocal lattice. (b) Square reciprocal lattice with reciprocal lattice vectors shown as fine black lines	15
Figure 2.2. Reduction of the first BZ into what is termed the irreducible Brillouin zone (IBZ)	16
Figure 2.3. a) Principle of NEB method showing the initial position of intermediate images, nudging toward the minimum energy path. b) Digram showing how to calculate the activation energy from images energy	24
Figure 2.4. Illustration diagram of the given material, depicting (a) the bulk structure, (b) the supercell configuration, (c) specific Miller indices (hkl), and (d) the constructed slab model.....	27
Figure 2.5. Illustration diagram Showing a slab with symmetric and stoichiometric termination of the given material	28
Figure 2.6. Illustration diagram Showing a slab with symmetric and non-stoichiometric terminations of the given materia.....	29
Figure 2.7. Illustration diagram Showing a slab with asymmetric and nonstoichiometric terminations of the given material.....	31
Figure 3.1. (a) The skeleton of (LATP) depicts its crystal structure. (b) The migration path of Li ions within the LATP structure c)the 6b, 36f, and 18e Wyckoff positions within the LATP crystal lattice.....	36
Figure 3.2. The substitution of O atoms with S atoms in the LATP lattice	37
Figure 3.3. The change in the bond lengths of Li-ion in the first and second regions	40
Figure 3.4. (a) Computed activation energy barriers of Li ⁺ ion diffusion path along diffusion channels (1., 2., and 3. regions) in bare (LATP). (b) A comparison of the barrier energy in the second region with two different	42
Figure 3.5. Comparison of the energy barriers calculated by NEB for the Li ⁺ diffusion in the first region. Bare and sulfur doped LATP are shown by red and purple colours respectively.....	44
Figure 3.6. Comparison of the energy barriers calculated by NEB for the Li ⁺ diffusion in the second region. Bare and sulfur doped LATP are shown by blue and green colours respectively	45
Figure 3.7. (a) LiO ₆ polyhedrons in the diffusion path of first and second regions, (b-e) diffusion activation energy barriers along the diffusion paths. Numbers denoted by the red and purple colours are the polyhedral volumes of LiO ₆ in the accompanied Wyckoff positions of lithium atoms given in (a).	47
Figure 3.8. (ahv) ² – hv curves of the (a) Bare LATP, (b) S@LATP and the corresponding absorption spectra in the insets, (c) partial density of states of bare LATP (S0) and S@LATP (S1-S4), (d) charge density distributions in bare LATP and S@LATP.	49
Figure 3.9. (a-d) the core level shift between LATP and S@LATP (S1-S4)	51

Figure 3.10. (a-d) charge density distributions, between LATP and S@LATP (S1-S4)	52
Figure 3.11. a) The crystal structure of TiMn_2 , b) Simulated X-ray diffraction (XRD) pattern of TiMn_2 c) Band structure and partial density of states (PDOS) analysis for TiMn_2	54
Figure 3.12. The (112) surface plane of TiMn_2 with two different terminations, b) the (001) surface plane of TiMn_2 with four different terminations c) Surface energy comparison of all terminations as a function of the number of layers in the TiMn_2 crystal	55
Figure 3.13. Schematic representations of the TiMn_2 (0 0 1)-D4 surface, illustrating (a) all symmetric possible adsorption sites, (b) O atoms adsorption sites, and (c) Li atoms adsorption sites.....	57
Figure 3.14. Summary of the ORR overpotentials on TiMn_2 (0 0 1)-D4 surface with the adsorption energy for intermidate reacts. (a) the TiMn_2 (0 0 1)-D4 clean surface befor reaction. b) O_2 molecue adsorption c) first Li atom adsorption d) second Li atom adsorption	58
Figure 3.15. The Gibbs free energy diagrams for the ORR/OER on TiMn_2 (0 0 1)-D4 surface	59
Figure 3.16. The crystal structure of MnO_2 , b) Band structure and partial density of states (PDOS) analysis for $\alpha\text{-MnO}_2$	63
Figure 3.17. The (211) surface plane of MnO_2 with two different four terminations, b) Surface energy comparison of all terminations as a function of the number of layers in the MnO_2 crystal	65
Figure 3.18. Schematic representations of the MnO_2 (211)-Mn surface, illustrating (a) all symmetric possible adsorption sites, (b) O atoms adsorption sites, and (c) Li atoms adsorption sites.....	67
Figure 3.19. Summary of the ORR overpotentials on MnO_2 (211)-Mn surface with the adsorption energy for intermidate reacts using GGA+U method (a) the MnO_2 (211)-Mn clean surface befor reaction. b) First Li atom adsorption c) O_2 molecue adsorption d) second Li atom adsorption	67
Figure 3.20. Summary of the ORR overpotentials on MnO_2 (211)-Mn surface with the adsorption energy for intermidate reacts using SCAN+U method (a) the MnO_2 (211)-Mn clean surface befor reaction. b) First Li atom adsorption c) O_2 molecue adsorption d) second Li atom adsorption	68
Figure 3.21. The Gibbs free energy diagrams for the ORR/OER on MnO_2 (211)-Mn surface termination using a) GGA+U method, b) SCAN+U method.	69

COMPUTATIONAL INVESTIGATION OF BATTERY MATERIALS USING DENSITY FUNCTIONAL THEORY

SUMMARY

Lithium-ion rechargeable batteries have revolutionized the world of portable electronics and electric vehicles. However, as the demand for high-performance, sustainable energy storage solutions grows, there is an increasing need to explore and optimize the materials used in these batteries.

The use of Density Functional Theory (DFT) first-principle calculations is pivotal in rechargeable battery research. DFT enables precise exploration of atomic and electronic interactions in battery materials, offering insights into properties, electrochemical behavior, and the design of new materials. It accelerates battery development, ultimately shaping the future of energy storage technology.

This thesis represents a comprehensive investigation into the application of first-principle calculations based on DFT to advance our understanding of two distinct classes of lithium rechargeable batteries: all-solid-state batteries (ASSBs) and Li-O₂ batteries.

The first major segment of this study is dedicated to investigating the intricacies of all-solid-state batteries, with a specific emphasis on LiAlTi(PO₃)₄ (LATP) and Sulfur doped LATP (S@LATP) as a solid electrolyte. Solid-state batteries hold immense promise as they offer a safer alternative to conventional liquid electrolyte batteries while potentially delivering higher energy densities.

Solid electrolytes offer improved safety, higher energy density, and longer cycle life compared to liquid electrolytes. These electrolytes come in various forms, including ceramics, polymers, and composites, each with unique characteristics. Challenges like low ionic conductivity and complex manufacturing persist but are being addressed through computational modeling and material synthesis. Notable materials like (LATP) show potential in all-solid-state batteries due to their high ionic conductivity, stability, and safety.

To unlock their full potential, a deep understanding of the solid electrolyte's properties is essential.

Our inquiry begins with a meticulous examination of the structural properties of LATP and S@LATP. Our study provides an explanation about the effect of Sulfur doping on the lattice parameters, stability, and atomic bond length of LATP.

Leveraging the first-principle calculations and the Nudged Elastic Band (NEB) method, we embark on a detailed exploration of lithium ion diffusion mechanisms within both LATP and sulfur-doped LATP.

The results not only reveal the energetically favored diffusion paths but also provide insights into the activation energy barriers, critical information for optimizing ionic

conductivity in solid electrolytes. Our results showed sulfure doping caused a locally inhance the ionic diffution in LATP.

Beside the structural properties and lithium ion diffusion, We delve into the charge distribution and electrochemical environment within LATP. Employing techniques such as charge transfer analysis, Bader charge analysis, and core level shifting, we gain insights into the change in the electrochemical behavior of LATP solid electrolyte.

These findings not only contribute to the fundamental understanding of LATP but also lay the groundwork for strategies aimed at improving the ionic diffution in LATP liked electrolytes, such as LAGP. The second pivotal segment of this thesis pivots towards the realm of Li-O₂ batteries.

Li-O₂ batteries, or lithium-oxygen batteries, show potential for high-energy applications like electric vehicles and energy storage due to their high theoretical energy density. These batteries consist of a lithium metal anode, a Li⁺ conducting electrolyte, and a porous oxygen (O₂) cathode. The choice of cathode materials is crucial. Common types include noble metals, carbon-based materials, transition metal compounds, and perovskite oxides. Researchers are actively exploring these materials and employing advanced techniques like density functional theory (DFT) simulations to optimize Li-O₂ battery performance. This research focuses on TiMn₂, a transition metal compound, and MnO₂, a transition metal oxide, as potential carbon-free cathode materials for Li-O₂ batteries.

While carbon-based cathodes have been the norm, the transition to carbon-free alternatives is imperative for improving overall battery performance. Carbon-free cathodes play a pivotal role in the advancement of Li-O₂ batteries due to their paramount importance in improving battery performance and sustainability.

Two noteworthy candidates, Titanium Manganese (TiMn₂) and Manganese Dioxide (MnO₂) was selectedt as a carbon free cathod materials.

In this thesis, TiMn₂ was selecteted for the first time to be an exciting cathode material, and its examination in this thesis represents a promessing potential as a carbon free cathod.

The study delves into the surface stability of TiMn₂, analyzing different atomic surface terminations. Moreover, our investigations involve the oxygen redaction/evolution reactions ORR/OER mechanism to form the final product of li-O₂ battery reaction, Li₂O₂.

The Gibbs free energy diagram further elucidates the ORR/OER process, and the calculated overpotential values for ORR and OER demonstrate.

We invistigate the With an overpotential of approximately 1.16 V, TiMn₂ showcases promising results, making it a strong contender for future Li-O₂ batteries.

Manganese dioxide (MnO₂) underwent a comprehensive investigation employing two distinct Density Functional Theory (DFT) methodologies, namely, the Generalized Gradient Approximation with Hubbard U term (GGA+U) and the Strongly Constrained and Appropriately Normed with Hubbard U term (SCAN+U). Both GGA+U and SCAN+U methodologies exhibited significant variations in lattice parameters and calculated band gap values. Furthermore, an examination of MnO₂'s surface stability was conducted to identify the most stable termination. This study also furnished insights into surface reactivity toward lithium (Li) and oxygen (O)

atoms in the surrounding environment. Subsequently, the Oxygen Reduction Reaction (ORR) and Oxygen Evolution Reaction (OER) were investigated using both GGA+U and SCAN+U approaches. The results demonstrated that the selected computational approach significantly influenced adsorption energy values and the positions of adsorbed reaction intermediates. Additionally, Gibbs free energy diagrams were simulated, enabling the calculation of charge and discharge potentials as well as overpotential. Notably, the outcomes revealed that each approach, GGA+U and SCAN+U, provided distinct values. This comparative analysis not only facilitated the assessment of the accuracy of initial structural predictions but also yielded valuable insights into the surface properties of the material.

Overall, this thesis demonstrates the use of first-principle calculations as a powerful tool for understanding and optimizing the performance of advanced lithium rechargeable batteries.

YOĞUNLUK FONKSİYONEL TEORİSİ KULLANILARAK PİL MALZEMELERİNİN HESAPLAMALI İNCELENMESİ

ÖZET

Lityum-iyon şarj edilebilir piller, taşınabilir elektronik cihazlar ve elektrikli araçlar dünyasında devrim yaratmıştır. Ancak yüksek performanslı, sürdürülebilir enerji depolama çözümlerine olan talep arttıkça, bu pillerde kullanılan malzemeleri keşfetme ve optimize etme ihtiyacı da artmaktadır.

Yoğunluk Fonksiyonel Teorisi (DFT) ilk prensip hesaplamalarının kullanımı, şarj edilebilir pil araştırmalarında hayati bir öneme sahiptir. DFT, pil malzemelerindeki atomik ve elektronik etkileşimleri hassas bir şekilde inceleyerek özellikler, elektrokimyasal davranış ve yeni malzemelerin tasarımına dair öngörüler sunar. Bu, pil gelişimini hızlandırarak enerji depolama teknolojisinin geleceğini şekillendirmektedir.

Bu tez, DFT temelli ilk prensip hesaplamalarının uygulanmasıyla lityum şarj edilebilir pillerin iki farklı sınıfı olan tamamen katı hal piller (ASSB'ler) ve Li-O₂ pillerini düzeyde anlaşılması amacıyla kapsamlı bir incelemeyi temsil etmektedir. Bu çalışmanın ilk büyük bölümü, özellikle katı bir elektrolit olarak LiAlTi(PO₃)₄ (LATP) ve kükürt katkılı LATP (S@LATP) üzerinde vurgu yaparak, tamamen katı hal pillerin özelliklerini araştırmaya adanmıştır. Katı hal piller, geleneksel sıvı elektrolit pillere göre daha güvenli bir alternatif sunarken potansiyel olarak daha yüksek enerji yoğunlukları sunmayı vadederler.

Katı elektrolitler, sıvı elektrolitlere kıyasla artırılmış güvenlik, daha yüksek enerji yoğunluğu ve daha uzun döngü ömrü sunarlar. Bu elektrolitler seramikler, polimerler ve kompozitler gibi çeşitli biçimlerde bulunabilirler ve her biri benzersiz özelliklere sahiptir. Düşük iyonik iletim ve karmaşık üretim gibi zorluklar hesaplamalı modelleme ve malzeme sentezi yoluyla ele alınmaktadır. LATP gibi dikkate değer malzemeler, yüksek iyonik iletkenlikleri, stabilite ve güvenlikleri nedeniyle tamamen katı hal piller için güçlü bir potansiyel oluşturmaktadır.

Bu potansiyeli tam anlamak için katı elektrolitin özelliklerini derinlemesine anlamak gereklidir. Araştırmamız, LATP ve S@LATP'nin yapısal özelliklerinin titiz bir incelemesi ile başlar; çalışmamız, kükürt katkısının LATP'nin örgü sabitleri, kararlılık ve atomik bağ uzunluğu üzerindeki etkisini açıklar.

İlk prensip hesaplamaları ve Düzeltme Elastik Bant (NEB) yöntemini kullanarak, hem LATP hem de kükürt katkılı LATP içindeki lityum iyonu difüzyon mekanizmalarının detaylı bir şekilde incelenmiştir. Sonuçlar sadece enerji açısından tercih edilen difüzyon yollarını ortaya çıkarmakla kalmaz, aynı zamanda katı elektrolitlerde iyonik iletkenliği optimize etmek için kritik aktivasyon enerji bariyerleri hakkında öngörüler sunar.

Sonuçlarımız, sülfür katkısının LATP içinde iyonik difüzyonu yerel olarak artırabileceğini gösterir. Yapısal özellikler ve lityum iyon difüzyonunun yanı sıra,

LATP içindeki yük dağılımı ve elektrokimyasal çevre ile ilgili olarak yük transfer analizi, Bader yük analizi ve çekirdek seviye kayma gibi teknikler kullanarak öngörüler elde edilir.

Bu bulgular, sadece LATP'nin temel anlayışına katkıda bulunmakla kalmaz, aynı zamanda LAGP gibi LATP benzeri elektrolitlerde iyonik iletimi iyileştirmeye yönelik stratejilerin temelini oluşturur.

Bu tezin ikinci önemli bölümü Li-O₂ pil alanına yönelmesidir. Li-O₂ piller veya lityum-oksijen piller, yüksek teorik enerji yoğunlukları nedeniyle elektrikli araçlar ve enerji depolama gibi yüksek enerjili uygulamalar için büyük bir potansiyele sahiptir. Bu piller, bir lityum metal anot, bir Li⁺ iletken elektrolit ve gözenekli bir oksijen (O₂) katottan oluşur.

Katot malzemelerinin seçimi son derece önemlidir. Yaygın türler arasında soy metaller, karbon bazlı malzemeler, geçiş metal bileşikleri ve perovskit oksitleri bulunmaktadır. Araştırmacılar bu malzemeleri aktif bir şekilde araştırmakta ve Li-O₂ pil performansını optimize etmek için Yoğunluk Fonksiyonel Teorisi (DFT) simülasyonları gibi gelişmiş teknikler kullanmaktadır. Bu araştırma, Li-O₂ pilleri için potansiyel karbon içermeyen katot malzemeleri olarak TiMn₂ adlı bir geçiş metal bileşiği ve MnO₂ adlı bir geçiş metal oksitine odaklanmaktadır.

Karbon bazlı katotlar şu anda yaygın olarak kullanılsa da, genel pil performansını iyileştirmek için karbonsuz alternatiflere geçmek gereklidir. Karbonsuz katotlar, Li-O₂ pillerin genel performansını ve sürdürülebilirliğini artırmada önemli bir role sahiptir.

Bu çalışma, karbon içermeyen katot malzemeleri olarak dikkat çeken iki aday Titanyum Manganez (TiMn₂) ve Manganez Dioksit (MnO₂) üzerine odaklanılmıştır.

Bu tezde, TiMn₂'nin karbon içermeyen bir katot malzemesi olarak heyecan verici bir şekilde seçilmesi ve incelenmesi, gelecekteki Li-O₂ piller için güçlü bir rakabetçi potansiyeli temsil etmektedir. Çalışma, TiMn₂'nin yüzey stabilitesini farklı atomik yüzey sonlandırmalarını analiz ederek araştırılmaktadır. Ayrıca, Li-O₂ pil reaksiyonunun nihai ürünü olan Li₂O₂'yi oluşturmak için oksijen redüksiyon/oksidasyon reaksiyonlarını (ORR/OER) içermektedir. Gibbs serbest enerji diyagramı, ORR/OER sürecini daha ayrıntılı bir şekilde açıklamaktadır ve ORR ve OER için hesaplanan aşırı potansiyel değerlerini göstermektedir.

Yaklaşık 1.16 V'lık bir aşırı potansiyele sahip olan TiMn₂, umut verici sonuçlar sergileyerek gelecekteki Li-O₂ piller için güçlü bir rakip olarak öne çıkmaktadır. Manganez dioksit (MnO₂) ise, Genelleştirilmiş Gradyan Yaklaşımı (GGA+U) ile Güçlü Kısıtlanmış ve Uygun Şekilde Normlanmış (SCAN+U) olmak üzere iki farklı Yoğunluk Fonksiyonel Teorisi (DFT) metodolojisi kullanılarak kapsamlı bir şekilde araştırılmıştır. Hem GGA+U hem de SCAN+U metodolojileri, kafes parametrelerinde ve hesaplanan bant aralığı değerlerinde önemli farklılıklar göstermiştir. Ayrıca, MnO₂'nin yüzey kararlılığını belirlemek için yapılan çalışma, çevresindeki lityum (Li) ve oksijen (O) atomlarına karşı yüzey reaktivitesini anlama konusunda da bilgiler sunmaktadır. Daha sonra, Oksijen İndirgeme Reaksiyonu (ORR) ve Oksijen Evrim Reaksiyonu (OER), hem GGA+U hem de SCAN+U yaklaşımları kullanılarak incelenmiştir. Sonuçlar, seçilen hesaplamalı yaklaşımın adsorpsiyon enerjisi değerlerini ve adsorbe edilen reaksiyon ara ürünlerinin konumlarını önemli ölçüde etkilediğini göstermiştir. Ayrıca Gibbs serbest enerji diyagramları simüle edilerek şarj ve deşarj potansiyellerinin yanı sıra aşırı

potansiyelin hesaplanmasına da imkan tanımıştır. Bu çalışmanın karşılaştırmalı analizi, başlangıçta yapılan yapısal tahminlerin doğruluğunu değerlendirmenin yanı sıra malzemenin yüzey özellikleri hakkında değerli bilgiler sunmaktadır.

Genel olarak, bu tez birinci prensip hesaplamalarının, yeni nesil lityum şarj edilebilir pillerin performansını anlama ve optimize etme açısından güçlü bir araç olarak kullanıldığını göstermektedir. Bu çalışma, şarj edilebilir pillerin elektrokimyasal reaksiyon mekanizmalarını anlama konusundaki teorik ve deneysel boşluğu kapatmaya yönelik öncü çalışmaların temellerini oluşturmaktadır.

1. INTRODUCTION

Energy storage technology is a major barrier to clean energy. Today, rechargeable lithium-ion batteries (LIBs) have been considered as the most promising power sources in a wide range of applications from small electronic devices to the large scale application like electric vehicles (Ji, 2011; Goodenough, 2013). However, the adherence to conventional intercalation chemistries, energy density and safety concerns represented in the flammable liquid electrolytes have limited their commercialization for many applications (Wang, 2021; Dai, 2019; Boev, 2021).

Therefore, many years of effort have been put into proposing solutions to the above problems. Lithium-Air batteries (LABs) could be a favourable alternative to LIBs, due to their extremely higher theoretical specific energy (3500 Wh/kg) compared to (600–800 Wh/kg) for LIBs (Mehri 2021; Boev, 2021). On the other side, the use of all-solid-state batteries (ASSBs) is a promising alternative that would address the concerns over safety and energy density (DeWees, 2019; Liu, 2018).

In the quest for discovering new materials, substantial laboratory resources are typically required. However, an appealing solution lies in materials modeling, a powerful tool that can effectively reduce the costs and time associated with the discovery process. The accuracy in modeling battery materials has been significantly advanced by employing a cutting-edge quantum-mechanical theory called density functional theory (DFT) (Harper et al, 2020). Through DFT, we gain deep insights into the atomic-level behavior of materials, enabling us to make valuable predictions about their performance as vital battery components. Notably, DFT outcomes serve a dual purpose by not only guiding experimental design but also facilitating the interpretation of experimental results (Ells et al, 2022).

The main aim of this thesis is to present a detailed investigation of promising materials for lithium-based batteries using computational approaches based on Density Functional Theory (DFT). The First part of the research is dedicated to exploring all-solid-state Li-ion batteries (ASSLB), with a particular focus on studying LATP ($\text{LiAlTi}(\text{PO}_3)_4$) as a solid electrolyte. The investigation involves the

influence of sulfur doping on structure properties, lithium ion migration, and electronic structure in LATP. In the second part, the focus shifts to evaluating the efficiency of TiMn_2 and MnO_2 as carbon-free cathode materials for Li- O_2 batteries. The performance assessment involves calculating the Oxygen Reduction Reaction (ORR) and Oxygen Evolution Reaction (OER) diagrams, derived from Gibbs free energy calculations. Moreover, by precisely assessing the performance of both cathodes, we can gain valuable insights into the efficiency of these materials as cathode materials.

1.1. Next Generation of Rechargeable Batteries

Next-generation rechargeable batteries have emerged as a promising avenue to address the limitations of conventional lithium-ion batteries, such as energy density, cycle life, and environmental sustainability.

Among these contenders batteries, The landscape of metal-air batteries, including lithium-air, zinc-air, magnesium-air, and aluminum-air configurations, holds promise for future EVs by capitalizing on ambient oxygen as a vital battery reactant, consequently ameliorating battery weight and augmenting energy storage capacity. Notably, lithium-air batteries manifest the highest theoretical energy density, akin to gasoline engines ($13,000 \text{ Whkg}^{-1}$). However, the road to practical realization is rife with multifarious challenges. These encompass incomplete discharge due to the impediment posed by porous carbon cathodes obstructed by discharge products, anode instability in the presence of atmospheric moisture, inadequate understanding of catalyst influences, and electrical inefficiency attributed to higher charge overpotential in contrast to discharge overpotential. Furthermore, carbonate-based electrolytes tend to undergo decomposition during discharge, engendering lithium alkyl-carbonates and Li_2CO_3 , culminating in a pronounced impact on the rechargeability and cycle life of lithium-air batteries (Rahman et al, 2013).

Lithium-sulfur (Li-S) batteries have garnered substantial attention for their theoretically anticipated specific capacity (1675 mAh g^{-1}), energy density (2600 Wh kg^{-1}), and exploitation of abundant and environmentally benign sulfur. Nonetheless, the realization of these potentials is marred by a set of significant challenges. These challenges encompass the constrained conversion of polysulfides, inadequate sulfur utilization due to the non-conductive nature of sulfur and the formation of solid

products (Li_2S_2 and Li_2S), substantial capacity fade, low Coulombic efficiency (CE) driven by the shuttle effect of soluble polysulfides, electrode structural degradation arising from volumetric fluctuations (80%), and the safety concern of lithium dendrite formation during charge and discharge processes (Manthiram et al, 2014).

The purview of advanced sodium-ion batteries (SIBs) and potassium-ion batteries (PIBs) is characterized by their potential to emerge as leading candidates for grid-scale energy storage systems, attributed to the wide distribution and economic viability of sodium and potassium resources. However, the higher redox potential of Na/Na^+ (-2.71 V vs. standard hydrogen electrode) in contrast to Li/Li^+ (-3.04 V) translates to lower discharge voltage plateaus and energy densities. Conversely, K/K^+ systems exhibit a lower standard redox potential (-2.93 V), promising augmented energy density. Nevertheless, the sizeable ion radius of K^+ (1.38 Å) imparts a sluggish diffusion kinetics, yielding suboptimal capacity, rate performance, and cycling stability during the insertion and deinsertion process (Huang, 2020; Ye, 2021).

The domain of aqueous zinc (Zn) batteries, encompassing both Zn-ion batteries and Zn-air batteries, has recently emerged as a focal point of interest owing to their projected high theoretical capacity (820 mAh g^{-1}), inherent safety, low toxicity, and cost-effectiveness. Nonetheless, this promise is offset by a series of challenges that necessitate resolution. The development of aqueous Zn-ion batteries (ZIBs) is beleaguered by the absence of suitable cathode materials tailored for Zn-ion storage. In the context of Zn-air batteries, the sluggish kinetics of oxygen electrocatalysis often engender excessive overpotential and compromised cycling stability. Additionally, dendrite formation in the anode, attributed to irregular charge distribution and side reactions during plating and stripping, precipitates issues of poor cycle life, capacity degradation, and safety concerns (Jia, 2020; Ye, 2021).

The drive to address the multifaceted challenges intrinsic to each next-generation battery paradigm has spurred a robust body of research endeavors aimed at exploring novel materials characterized by heightened electrochemical performance.

1.1.1. All solid-state battery

All-solid-state batteries ASSBs use solid electrodes and a solid electrolyte instead of liquid or gel electrolytes. They offer several advantages over traditional lithium-ion

batteries, including higher energy density, better safety, and longer lifespan. All-solid-state batteries are made with a solid electrolyte, which allows for the elimination of liquid or gel-like electrolytes that can leak, causing safety issues and reducing the battery's performance over time. The development of all-solid-state batteries is important for meeting the increasing demand for energy storage in various applications, including electric vehicles, portable electronics, and renewable energy systems (Yang, 2018; Dubarry, 2017; Wu, 2017).

1.1.1.1. Solid electrolyte

Solid electrolytes have gained significant attention in the domain of energy storage technologies due to their promise to transform traditional lithium-ion batteries fundamentally. Solid electrolytes are materials with the ability to conduct ions, such as lithium ions, without relying on liquid electrolytes. This unique property offers several advantages over liquid electrolytes, including improved safety, increased energy density, and longer cycle life. However, solid electrolytes also pose challenges such as low ionic conductivity and difficulties in their synthesis and processing (Janek & Zeier, 2016).

There are several types of solid electrolytes, including ceramics, polymers, and composite materials. Ceramic electrolytes are characterized by their high ionic conductivity, Nevertheless, their brittleness and high processing temperatures present significant challenges. Polymer electrolytes, on the other hand, exhibit lower ionic conductivity, however they offer flexibility and ease of processing. Composite electrolytes, which combine the advantages of both ceramics and polymers, are a promising alternative that can achieve higher ionic conductivity while retaining their flexibility and ease of processing (Janek & Zeier, 2016).

One of the most critical challenges in the development of solid electrolytes is the optimization of their ionic conductivity while maintaining their mechanical properties. Additionally, the development of cost-effective and scalable manufacturing processes remains a significant challenge. However, recent advances in computational modelling and material synthesis have shown promise in addressing these challenges (Yu, 2017; Chen, 2019).

One type of solid electrolyte that has received significant attention is NASICON (Sodium superionic conductor), which has a crystalline structure consisting of

alternating layers of rigid anionic frameworks and mobile cations (Zhang, 2020; DeWees, 2019).

One of the most studied NASICON materials is Lithium Aluminum Titanium Phosphate (LATP), which has shown promising results in all-solid-state batteries. LATP solid electrolyte has several advantages over traditional liquid electrolytes, including high ionic conductivity of approximately 10^{-3} S/cm at room temperature, Stability and, Safety (Rosenberger et al, 2015).

1.1.2. Li-O₂ battery

A Li-O₂ battery is a type of rechargeable battery that uses lithium metal as the anode and oxygen as the cathode. Li-O₂ batteries are considered as a promising technology for high-energy applications, such as electric vehicles and energy storage, due to their high theoretical energy density (Gao, 2017; Luo, 2016).

A Li-O₂ typically comprises a Li metal anode, a Li⁺ conducting electrolyte and a porous O₂ cathode. During discharge, O₂ reduces with Li⁺ from the anode to Li₂O₂ through an oxygen reduction reaction (ORR). During charge, the lithium peroxide decomposes to release oxygen and lithium ions through an oxygen evolution reaction (OER) (Ma, 2018).

One of the main challenges in developing Li-O₂ batteries is to increase their cycle life and efficiency, as well as to reduce their tendency to produce side reactions, such as the formation of lithium dendrites, which can short-circuit the battery (T. Liu et al, 2020).

Despite these challenges, Li-O₂ batteries have the potential to be a valuable energy storage technology, and much research is ongoing to improve their performance and overcome the technical challenges associated with their development.

1.1.2.1. Cathode materials

Overall, the development of effective cathode materials is a key challenge in the advancement of Li-O₂ batteries and a critical area of research in the field of energy storage. The cathode in a Li-O₂ battery serves as the host for the oxygen reduction reaction (ORR). The choice of cathode material can affect the battery's efficiency, safety, and stability (Balaish et al, 2020).

There are several types of cathode materials that have been studied commonly for use in Lithium-Oxygen (Li-O₂) batteries, including:

Noble metals: such as gold (Au), platinum (Pt), and palladium (Pd) have been investigated as potential carbon-free cathode materials for lithium-oxygen (Li-O₂) batteries. These metals have high electrical conductivity and can catalyze the electrochemical reactions that occur during the charge and discharge cycles of the battery. One of the advantages of using noble metals as cathode materials is that they can facilitate the reduction and oxidation of oxygen without forming carbon-based intermediates, which can improve the overall efficiency of the battery. Additionally, noble metals can offer high capacity and long cycle life, making them a promising option for Li-O₂ batteries. However, there are still some challenges associated with using noble metals as cathode materials. For example, these metals can be expensive and scarce, which can make them less practical for large-scale commercial applications. Additionally, the stability and durability of these materials over long-term cycling is still an area of active research (Xu, 2015; Liao, 2015; Zhao, 2023).

Carbon-based cathodes: (such as graphene, carbon nanotubes, activated carbon, and carbon black) have been a subject of interest in the development of lithium-oxygen (Li-O₂) batteries due to their high surface area, good electrical conductivity, and relatively low cost (Kim, 2015; Nie, 2016). However, there are still challenges to be overcome in the development of carbon-based cathodes for Li-O₂ batteries. One major challenge is the formation of unwanted side products during electrochemical reactions, which can degrade the performance and reduce the overall efficiency of the battery. Another challenge is the limited capacity of the cathode, which is a result of the limited amount of oxygen that can be stored in carbon-based materials (Yi, 2022; Wang, 2019).

Transition metal compounds: such as (Co₃O₄), (Fe₃O₄), (MnO₂), These materials have a unique crystal structure and can catalyze the electrochemical reactions that occur during the charge and discharge cycles of the battery (Zhu, 2015; Zhan, 2021). Transition metal compounds have several properties that make them attractive as cathode materials. They have high electrical conductivity and can facilitate the electrochemical reactions that occur during the charge and discharge cycles of the battery. Additionally, they can offer high capacity and long cycle life, making them a promising option for Li-O₂ batteries (Karuppasamy et al, 2020).

Perovskite oxides: such as LaCoO_3 (LCO). Perovskite oxides have a unique crystal structure and a general formula of ABO_3 , where A is a large cation, such as lanthanum (La), and B is a transition metal, such as cobalt (Co), iron (Fe), or manganese (Mn) (Bhalla, 2000; Ahmed, 2018; He, 2023). Perovskite materials have several properties that make them attractive as cathode materials. They have high electrical conductivity and can catalyze the electrochemical reactions that occur during the charge and discharge cycles of the battery. They also have a unique crystal structure that can facilitate the reversible oxygen reduction and evolution reactions that are central to the operation of a Li-O₂ battery (J. Zhang et al, 2014).

Despite the potential advantages of perovskite oxide materials as cathode materials, there are still challenges that need to be addressed. For example, the synthesis and processing of these materials can be complex and expensive, and there is still much research needed to improve their performance and stability over long-term cycling. Nonetheless, the use of perovskite oxide materials as carbon-free cathode materials for Li-O₂ batteries represents a promising area of research with the potential to significantly improve the energy density and efficiency of next-generation batteries (Y. Zhao et al, 2017a).

In order to optimize the performance of Li-O₂ batteries, researchers are actively exploring new cathode materials and improving the existing ones. This involves using advanced techniques such as density functional theory (DFT) simulations to understand the behavior of the materials at the atomic and molecular scale, as well as experimenting with different synthesis methods to improve the performance and stability of the materials. This work focuses on a comprehensive study of two materials as potential carbon-free cathodes, namely TiMn_2 , a transition metal compound, and MnO_2 , a transition metal oxide.

1.2. Using Density Functional Theory as a Tool to Investigate Battery Materials

Efforts towards the commercialization of novel battery systems have encountered considerable technical challenges. One such obstacle lies in the intricate atomic and molecular-level reaction mechanisms of these batteries, which are arduous to probe experimentally despite rapid advances in characterization techniques. A comprehensive comprehension of battery material operational mechanisms is imperative for advancing these materials for industrial applications. The foundational

electronic structure and inter-nuclear repulsion in solid materials, governed by the Born-Oppenheimer approximation of the Schrödinger equation, dictate various material properties. These include lattice constants, cohesive energies, band structures, surface reactivity, thermochemistry, and rate constants. In this regard, the Kohn-Sham density functional theory (DFT) has emerged as a predominant computational tool for solving the Schrödinger equation in materials science. The accuracy of DFT calculations relies on the quality of the exchange-correlation (XC) functional. The evolution of XC density functionals spans three generations, including the local spin density approximation (LSDA), the generalized gradient approximation (GGA), and meta-GGAs. While LSDA demonstrates efficacy in predicting lattice constants, its limitations in modeling chemical reactions necessitate more advanced functionals. GGA and meta-GGAs exhibit improved accuracy for chemical bond energies, although they still underperform for certain properties. Hybrid functionals, incorporating nonlocal Hartree-Fock exchange, enhance accuracy for band gap predictions, albeit with higher computational costs (He, 2019; Shi-Qi, 2002; Åvall, 2018).

In recent years, DFT has found increasing application in simulating and understanding energy storage materials, with GGA functionals such as Perdew-Burke-Ernzerhof (PBE) GGA being commonly employed in battery materials research. DFT enables the calculation of thermodynamic properties, electronic structures, reaction kinetics, and ion transport pathways, offering advantages in exploring atomic-level reaction mechanisms and screening new battery materials compared to experimental methods. While experimental studies dominate this research field, DFT serves as a supplementary tool for validation. Certain studies focus solely on theoretical analyses of battery materials using DFT, while others balance experimental and computational approaches.

2. METHODE

The present thesis relies exclusively on the Density Functional Theory (DFT) for all calculations. This fundamental theory forms the basis for material modelling using quantum mechanics. The ensuing chapter provides a succinct introduction to DFT, highlighting its essential features. Subsequently, the chapter explains the application of DFT-based calculations in solving rechargeable battery problems. The chapter concludes by presenting a summary of the software employed in carrying out the calculations.

2.1. Density Functional Theory

Density functional theory (DFT) is a computational method used in condensed matter physics, materials science, and chemistry to understand the electronic structure of molecules, atoms, and solids. DFT was introduced in the 1960s by Walter Kohn and Pierre Hohenberg, and it won them the Nobel Prize in Chemistry in 1998 (Jungwirth, 2010; Koch, 2001; Koch, 2001). DFT used to solve the Schrödinger equation for a many-electron system (Engel & Dreizler, 2011).

The Schrödinger equation describes the behavior of quantum mechanical systems, such as atoms and molecules. However, the equation is too complex to solve for most systems analytically. This led to the development of computational methods to solve the equation numerically. The Schrödinger equation takes the form:

$$H\Psi = E\Psi \quad (2.1)$$

Where H is the Hamiltonian operator, Ψ is the wavefunction of the system, and E is the energy eigenvalue associated with that wavefunction.

DFT is based on the idea that the total energy of a many-electron system can be expressed in terms of the electron density rather than the wave function. This is known as the Hohenberg-Kohn theorem, which states that the ground-state energy of a system is uniquely determined by its electron density.

$$\rho(r) = \Psi^*(r)\Psi(r) \quad (2.2)$$

Where $\rho(r)$ is the electron density at point r , and $\Psi(r)$ is the wave function.

The electron density $\rho(r)$ at a point in space (r) is defined as the probability of finding an electron at that point, summed over all the electrons in the system. Mathematically, we can write:

$$n(r) = \int \rho(r) dr = N \int \Psi(r, r_2, \dots, r_n)^2 dr^2 \dots dr_n \quad (2.3)$$

Where N is a normalization constant, Ψ is the wavefunction of the system, and the integral is taken over all possible positions of the other electrons in the system (r_2, \dots, r_n). The ground state energy of the system for one-electron can be express as:

$$E = E_{kin} + E_{ext} + E_H + E_x \quad (2.4)$$

Where E , E_{kin} , E_{ext} , E_H and, E_x is the total, kinetic, external, Hartree and exchange energies respectively.

For the interacting n -electron system, Kohn and Sham mapped the n -electron system (interacting) on the one-electron system (non-interacting) under the given external energy. As following:

$$E = E_{kin}^{non} + E_{kin}^{int} + E_{ext} + E_H + E_x + E_c^{int} \quad (2.5)$$

where E_{kin}^{non} and E_{int}^{non} represent noninteracting and interacting (correlating)

kinetic energies, respectively.

Equation (2.5) can be reformate as

$$E = E_{kin}^{non} + E_{ext} + E_H + E_{xc} \quad (2.6)$$

$$E = F[\rho(r)] + E_{ext} \quad (2.7)$$

Here, E_{xc} is the exchange-correlation energy and given by the sum of E_x , E_{int} and, E_{kin} .

The above Kohn-Sham energy equation can be rewritten in the corresponding Hamiltonian as Lee (2016),:

$$H_{KS} = H_{kin}^{non} + U_{ext} + U_H + U_{xc} \quad (2.8)$$

2.1.1. Exchange-correlation approximations in DFT

In Density Functional Theory (DFT), the exchange-correlation (XC) potential is a key component that accounts for the exchange and correlation effects that arise due to the Pauli exclusion principle. These effects arise due to the fact that electrons are indistinguishable and cannot occupy the same quantum state.

The exchange-correlation potential can be split into two parts: the exchange potential, V_x , which accounts for the exchange effects, and the correlation potential, V_c , which accounts for the correlation effects. In practice, it is difficult to compute the exact exchange-correlation potential, so various approximations are used (Kohn, 1965; Hohenberg, 1964).

2.1.1.1. Local density approximation (LDA)

The most widely used approximation is the Local Density Approximation (LDA), which assumes that the exchange-correlation energy at any point in space depends only on the electron density at that point:

$$E_{XC}^{LDA}[\rho(r)] = E_X^{LDA}[\rho(r)] + E_C^{LDA}[\rho(r)] \quad (2.9)$$

where $E_X[\rho(r)]$ is the exchange energy and $E_C[\rho(r)]$ is the correlation potential, both of which are functionals of the electron density, $\rho(r)$.

The LDA approximation for the exchange potential is given by:

$$E_x^{LDA}[\rho(r)] = \int \rho(r) \left[\varepsilon_x^{hom}[\rho(r)] + \varepsilon_c^{hom}[\rho(r)] \right] dr \quad (2.10)$$

$$E_x^{LDA}[\rho(r)] = -3/4(3/\pi\rho(r))^{(1/3)} \quad (2.11)$$

where the factor $-3/4$ comes from the exchange energy of the homogeneous electron gas and the $(3/\pi n(r))^{(1/3)}$ factor is the radius of a sphere containing one electron in the electron gas (Lee, 2016).

2.1.1.2. Generalized gradient approximation (GGA)

Another widely used approximation is the Generalized Gradient Approximation (GGA), which takes into account the gradient of the electron density in addition to the local density itself:

$$V_{XC}[n(r)\nabla n(r)] = V_X[n(r)\nabla n(r)] + V_C[n(r)\nabla n(r)] \quad (2.12)$$

The GGA approximation for the exchange energy is given by:

$$E_x^{GGA}[\rho(r)] = \int \rho(r) \varepsilon_{xc}^{GGA}[\rho(r)\rho(r)] dr \quad (2.13)$$

The general form of GGA in practice is expressed based on the LDA with an additional enhancement factor $F(s)$ that directly modifies the LDA energy:

$$E_x^{GGA}[\rho(r), s] = \int \varepsilon_{xc}^{LDA}[\rho(r)]\rho(r)F(s) dr \quad (2.14)$$

Here, the s depends on both electron density and its gradient (Lee, 2016).

$$s = C \frac{(\rho(r))}{\rho^{3/4}(r)} \quad (2.15)$$

2.1.2. Plane wave

A plane wave is a type of wave characterized by a consistent frequency and parallel, unending wave fronts. This specific wave form is commonly employed to represent functions with periodic behaviour. When it comes to the representation of electronic wave functions within the framework of Density Functional Theory (DFT), a basis set is utilized. This basis set can be constructed using either atomic orbitals or plane waves. Given those materials used in batteries exhibit inherent lattice structures and repeating unit cells, reflecting their periodic nature, the use of a plane wave basis set becomes particularly relevant for investigating these materials.

The plane wave basis set encompasses an infinite number of wave fronts, but practical calculations require a finite representation. In order to truncate the basis set, only plane waves with kinetic energy below a predetermined cut-off energy are considered. This cut-off energy value (E_{cutoff}) plays a critical role in determining the accuracy of the calculations. The formula for calculating E_{cutoff} is given as Tanner (1995):

$$E_{\text{cutoff}} = \frac{\hbar^2}{2m} |k|^2 \quad (2.16)$$

where k represents a wave vector, and m is an integer. The selection of an appropriate E_{cutoff} value is crucial to ensure that the calculated properties of interest converge reliably.

Within the context of periodic systems, the Bloch theorem Kronig & Penney (1931) is a foundational principle employed to express a wave function as a combination of a plane wave and a function that captures the lattice's periodicity. Mathematically, this is expressed as:

$$\Psi(r) = u(r)e^{ikr} \quad (2.17)$$

Where $u(r)$ signifies the periodic function, and $e^{(ik \cdot r)}$ denotes the plane wave component. In this equation, k symbolizes the wave vector (Ladha, 2019).

2.1.3. Brillouin zone

A plane wave is a type of wave characterized by a consistent frequency and parallel, Brillouin's statement of the diffraction condition, which is widely employed in solid state physics, was given, encompassing the description of electron energy band theory and various types of elementary excitations.

A definition of the Brillouin zone (BZ) is provided as a Wigner-Seitz primitive cell within the reciprocal lattice. When an attempt is made to illustrate a wave function in real (direct) space, the realization that it is not an easy task becomes immediate. However, in reciprocal space, the task is simplified to the construction of a grid, given that the unit of the reciprocal lattice matches that of wave vectors (1/length).

Consequently, the lattice points within this space are what define the permissible wave vectors, necessitating the construction of an unconventional structure known as the reciprocal lattice, which is derived from the real lattice. The reciprocal lattice and BZ are where electron waves can inhabit and be folded. These particular coordinate systems have been devised to enable the more straightforward capturing of electron behaviour.

The diffraction condition's vivid geometric interpretation is afforded by the Brillouin zone, with the next equation:

$$2k * G = G^2 \quad (2.18)$$

where G represents a reciprocal lattice vector and k is a wave vector serving as its basis. Both sides of the equation are divided by 4, yielding:

$$k * \left(\frac{1}{2}G\right) = \left(\frac{1}{2}G\right)^2 \quad (2.19)$$

Operating within reciprocal space, which encompasses the k's and G's, a vector G is selected, connecting the origin to a point within the reciprocal lattice. The vector G is chosen, originating from the origin and extending to a reciprocal lattice point. At this juncture, a plane is meticulously crafted, perpendicular to the vector G, and positioned exactly at its midpoint. This plane assumes the role of a zone boundary, a fundamental aspect depicted in Figure 2.1.a.

In the visual representation of Figure 2.1.a., one encounters reciprocal lattice points clustered around point O the origin of the reciprocal lattice. Notably, two distinct reciprocal lattice vectors, G-C and G-D, connect points OC and OD, respectively. Here, planes designated as (1) and (2) are meticulously drawn, each meticulously positioned as the perpendicular bisector of the vectors G-C and G-D. These planes hold a unique property: any vector originating from the origin and reaching plane (1), denoted as k1, inherently satisfies the diffraction condition. Likewise, for plane (2), characterized by vector k2, the diffraction condition as given in equation (2.19) is satisfied.

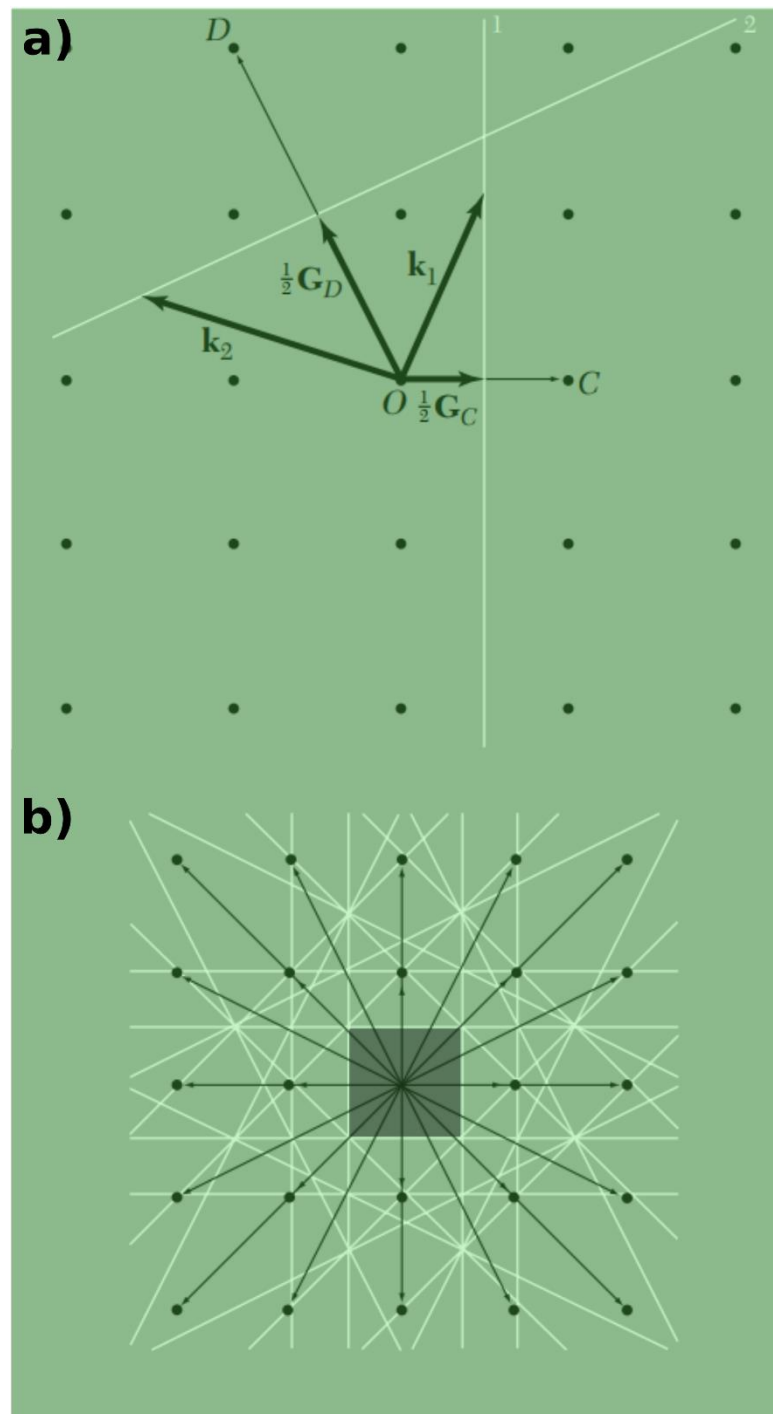


Figure 2.1. (a) Reciprocal lattice points near the point O at the origin of the reciprocal lattice. (b) Square reciprocal lattice with reciprocal lattice vectors shown as fine black lines.

The ensemble of planes constituted by the perpendicular bisectors of reciprocal lattice vectors acquires paramount significance in the realm of wave propagation theory within crystals. These planes fundamentally partition the Fourier space of the crystal, resulting in a profound impact. Waves with wavevectors extending from the origin and culminating on these planes invariably satisfy the diffraction condition.

This partitioning is visibly depicted in Figure 2.1.b., where the crystal's Fourier space is distinctly compartmentalized.

An emblematic feature arising from this partitioning is the emergence of the central square, assuming the role of a primitive cell within the reciprocal lattice. This square, representative of a Wigner-Seitz cell, possesses special attributes within the broader context of solid-state theory. Designated as the first Brillouin zone, it holds the distinction of being the smallest volume entirely enveloped by planes orthogonal to the reciprocal lattice vectors originating from the origin. Its significance resonates profoundly within the theoretical framework of crystalline systems (Kittel, 2005).

2.1.4. Irreducible Brillouin zone (IBZ)

A notable concept comes to light when contemplating the impact of symmetry operations, particularly rotations and inversions, on the initial Brillouin zone (BZ). These operations introduce a compelling perspective: the reduction of the first BZ into what is termed the irreducible Brillouin zone (IBZ), a phenomenon vividly portrayed in Figure 2.2.

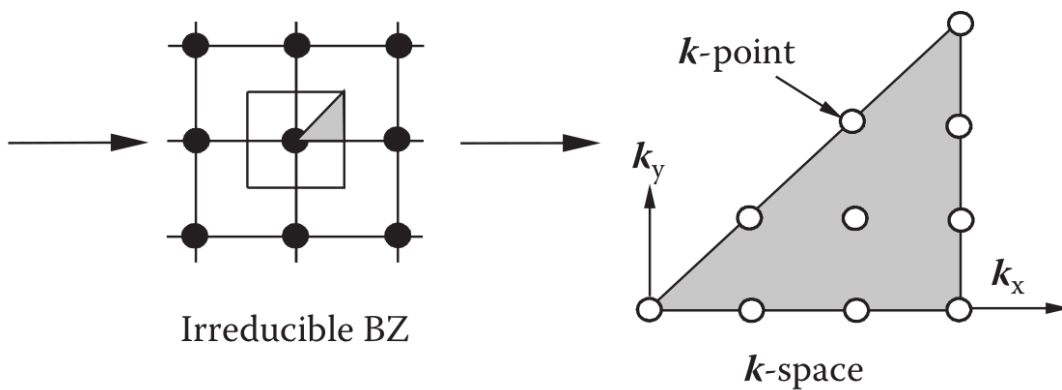


Figure 2.2. Reduction of the first BZ into what is termed the irreducible Brillouin zone (IBZ).

Taking an illustrative example from the domain of FCC lattices, envision a $10 \times 10 \times 10$ grid encapsulated within the first BZ. This grid encompasses a substantial array of 1000 k-points. However, with a skilful application of symmetry-based manipulations, this expansive realm condenses into a concise assemblage of only 35 distinct k-points within the confines of the IBZ. Importantly, it is worth acknowledging that each k-point carries a distinct weight, contingent upon the frequency of its occurrence during symmetry-driven operations (Lee, 2016).

2.1.5. K-points

Within the context of the irreducible Brillouin zone (IBZ), an intriguing observation emerges: any point residing within the IBZ holds the potential to signify a k-point. This intriguing prospect begets an infinite array of discrete k-vectors that possess the inherent attributes necessary to function as wave functions. Remarkably, the variations encompassed by the wave function and other related properties tend to exhibit smooth transitions across the expanse of the IBZ. This propitious characteristic allows for the selective sampling of a finite assortment of k-points, strategically chosen to represent distinct small regions within the IBZ.

This strategic selection has a significant purpose: it facilitates the evaluation of electronic energy and various other properties solely for occupied KS eigenstates. This evaluation is restricted to the chosen k-points, thereby contributing to computational efficiency. The process of sampling this specific ensemble of k-points in the IBZ stands as a crucial step in the dynamic flow of density functional theory (DFT). This endeavour adheres to a dual mandate: minimizing the selection to reduce computation time, while simultaneously ensuring that an adequate number of k-points are chosen to effectively represent the prevailing quantities.

In scenarios involving extensive systems—such as those encompassing hundreds of atoms—the volume of the IBZ becomes notably compact. Consequently, a judicious selection of a few k-points aptly captures the nuanced variations prevalent across the zone. Another illustrative instance surfaces when contemplating the usage of a supercell, often employed to explore surface studies. Typically extending in the z-direction (perpendicular to the surface), such a configuration involves a substantial vacuum layer a feature discussed in Figure 2.4. in section 2.2.6. Within this vacuum layer, wave functions progressively diminish to zero, warranting the selection of a solitary k-point along the z-direction.

Notably, each k-point houses a wealth of intricate information regarding the corresponding wave's attributes at that specific juncture. The profound implication of this selection process is that the extensive bulk material intricacies now narrow down to a succinct compilation of sampled k-points, ready for computational analysis.

2.1.5.1. Monkhorst–Pack method

One noteworthy strategy for effectively sampling k-points within the irreducible Brillouin zone (IBZ) is the Monkhorst–Pack method. This technique is designed to orchestrate the generation of a well-distributed grid of k-points spanning the expanse of the IBZ (Kittel, 2005).

To illustrate, consider the scenario of constructing a $4 \times 4 \times 4$ grid, encompassing a total of 64 k-points, within an FCC supercell. Upon the application of the Monkhorst–Pack method, the resulting outcome is quite intriguing. While the original grid might comprise 64 k-points, the method streamlines this to a mere 10 k-points discreetly nestled within the boundaries of the IBZ. This outcome is achieved by astutely distributing the k-points in a manner that optimally represents the underlying characteristics of the IBZ.

It is pertinent to note that contemporary density functional theory (DFT) codes offer a seamless solution for automating the generation of these specialized k-points. Upon inputting grid information, these codes are designed to promptly generate the requisite k-points tailored to the Monkhorst–Pack method. This automated process expedites the setup and execution of computational analyses, enhancing both accuracy and efficiency.

In essence, the Monkhorst–Pack method stands as a fundamental approach in the realm of k-point sampling. By strategically spacing k-points throughout the IBZ, this technique contributes to the precision and reliability of calculations in the domain of solid-state physics and material properties.

2.1.5.2. Γ -point method

In the context of substantial supercell configurations, a notable phenomenon arises, highlighting the significance of the Γ -point as a pivotal k-point. When dealing with these sizable supercells, it becomes evident that a solitary k-point could aptly encapsulate the entire essence of the irreducible Brillouin zone (IBZ) and succinctly describe various properties.

Of paramount importance is the Γ -point, which emerges as the foremost candidate among k-points due to its exceptional weight factor. Situated at the origin of the reciprocal space ($k = 0$), the Γ -point carries a high degree of significance. This k-

point holds a unique property where the real and reciprocal coordinates coincide, rendering the wave functions inherently real. The exclusion of complex numbers in this context streamlines computations and obviates the need for complex-valued considerations.

Moreover, the Γ -point enjoys the privilege of high symmetry in its vicinity. This symmetry enhancement augments computational efficiency and substantially reduces the requisite computation time—often by half. These advantages are exceedingly noteworthy, particularly when considering computationally intensive analyses.

Owing to these compelling attributes, the Γ -point-exclusive calculation method has garnered widespread acclaim for its utility in extensive computational endeavours. This approach, which leverages the unique attributes of the Γ -point, has been embraced as a preferred choice for conducting large-scale calculations. Its efficiency, symmetry advantages, and realism of wave functions converge to solidify the Γ -point as a cornerstone in the realm of material property simulations and extensive studies in solid-state physics (Lee, 2016).

2.1.6. DFT+U method

GGA+U is an extension of the generalized gradient approximation (GGA) in DFT. This method is particularly useful for materials with the effects of strong electron-electron interactions in materials with partially filled 3d, 4d, and 5d orbitals, such as transition metal oxides (Anisimov, 1991; Himmetoglu, 2014; Cococcioni, 2005).

The GGA+U method introduces an additional term to the total energy functional, known as the Hubbard U term. The Hubbard U term describes the energy cost of double occupancy of a given orbital on a given atom, and is given by:

$$U = \int d^3 r \rho(r)U(r) \quad (2.20)$$

where $U(r)$ is the on-site Coulomb interaction, and $\rho(r)$ is the electron density at position r .

The modified exchange-correlation functional includes the Hubbard U term, as shown below:

$$E_{XC}[n] = E_{XC, GGA}[n] + E_C, U[n] \quad (2.21)$$

Where $E_{xc, GGA}[n]$ is the exchange-correlation energy calculated using the GGA approximation, and $E_C, U[n]$ is the correction term due to the Hubbard U term. The correction term is given by:

$$E_{X, U}[n] = - \int d^3r U_{eff}(r) \sum N_i (n_i \uparrow (r))(n_i \downarrow (r)) \quad (2.22)$$

2.2. Computational Surface Science

Computational Surface Science is an interdisciplinary field that integrates principles of physics, chemistry, and materials science to investigate the properties and behavior of surfaces and interfaces. This field utilizes computer simulations and theoretical modelling to study the atomic and electronic structures of surfaces, their interactions with molecules and other materials, and the effects of external stimuli such as temperature, pressure, and electric fields (Oura et al, 2003). The development of powerful computational tools and algorithms has revolutionized the field of surface science, enabling researchers to simulate complex phenomena with unprecedented accuracy and detail. Computational techniques such as density functional theory (DFT) Sholl & Steckel (2009), molecular dynamics (MD) Tunega et al. (2002), and Monte Carlo (MC) Verma et al. (2018) simulations have become integral to the study of surface phenomena, providing valuable insights into processes such as catalysis, adhesion, and corrosion.

In addition, computational surface science has practical applications in fields such as nanotechnology, materials science, and energy research. By predicting the behavior of surfaces and interfaces, computational simulations can guide the design of new materials with specific properties and functions (Nolan et al, 2016).

Computational surface science deals with a wide range of surface properties, including atomic and electronic structure, surface energetics, surface reactivity, and surface dynamics (Groß, 2009).

2.2.1. Surface energy

Computational surface science can be used to calculate the surface energy or surface stability of materials. Surface energy is the energy required to create a unit area of a clean surface, while surface stability refers to the tendency of a surface to undergo structural changes or reconstruction (Groß, 2009).

The method used in this thesis to calculate the surface energy of a material is the slab model approach (Zuo et al, 2021). In this approach, a thick slab of the material is modelled with a vacuum layer above and below to mimic a clean surface. The total energy of the slab is calculated using electronic structure methods such as density functional theory (DFT). The surface energy is obtained by subtracting the bulk energy from the total energy of the slab as illustrated in the following equation;

$$E_{surface} = (E_{slab} - E_{bulk})/2A \quad (2.23)$$

Here, $E_{surface}$, E_{slab} , E_{bulk} , and A are the surface energy, slab energy, bulk energy, and cross area of slab respectively.

2.2.2. Surface reactivity

Computational surface science can be used to investigate the chemical reactions that occur on surfaces. This includes the study of adsorption, desorption, and reaction mechanisms. Adsorption energies and reaction barriers can be calculated using computational methods such as DFT, which can provide insights into surface reactivity and catalysis (Matz & Calatayud, 2017). The desorption energy was calculated according to the next equation:

$$E_{ads} = E_{a+b} - (E_b - E_a) \quad (2.24)$$

Where E_{a+b} , E_b and E_a is the total DFT energy of total system, slab and adsorbate molecule or atom respectively.

2.2.3. First-principles thermodynamics

First-principles thermodynamics is widely used in materials science, solid-state physics, and other fields to study the properties and the behavior of materials under different conditions. The calculated properties can then be used to predict the

thermodynamic properties of the material, such as energy, entropy, and free energy (Mai, 2021; Colmenero, 2019).

Gibbs free energy is a thermodynamic quantity that represents the potential energy available to do work in a system. It can be used to determine whether a reaction is spontaneous or not. A Gibbs free energy diagram shows the change in Gibbs free energy as a function of a reaction coordinate, which is often taken to be the fraction of a particular chemical species that has reacted (Lu et al, 2021).

To figure out the Gibbs free energy diagrams using DFT, one typically uses a combination of electronic structure calculations and thermodynamic modelling. Thermodynamic modelling involves calculating the enthalpy and entropy changes associated with the reaction. The enthalpy change can be calculated from the energy differences between the electronic states, while the entropy change can be calculated from the vibrational modes of the system (Fromsejer et al, 2023).

In our work, Gibbs free energy diagrams were used to study the Oxygen Reduction Reaction (ORR) and Oxygen Evolution Reaction (OER) in Lithium-Oxygen (Li-O₂) batteries.

The Gibbs free energy diagram for a given electrochemical reaction can be constructed by calculating the Gibbs free energy change (ΔG) at different potentials (E) using density functional theory (DFT) calculations. The Gibbs free energy of a reaction is given by the equation:

$$\Delta G = \Delta H - T\Delta S \quad (2.25)$$

where ΔH is the enthalpy change, T is the temperature in Kelvin, and ΔS is the entropy change. The enthalpy and entropy changes can be calculated using DFT calculations, which provide a detailed description of the electronic and geometric structures of the reactants and products.

The Gibbs free energy diagram can then be plotted as ΔG versus E , where E is the applied potential (Figure 3.13.).

2.2.4. Nudged elastic band method (NEB)

The principle that particles or matter tend to adopt configurations with the lowest energy when influenced by external forces is a well-established phenomenon. Understanding how a system undergoes configuration changes and identifying the path of minimum energy, known as the Minimum Energy Path (MEP), holds significant importance in materials research. In this section, our focus centers on harnessing the Nudged Elastic Band (NEB) method to pinpoint the MEP and its corresponding barrier energy.

The NEB methodology commences by establishing the initial and final states through customary electronic and ionic relaxations. At these configurations, energy is at a minimum, (and forces reflecting the first energy derivatives) are all zero.

Given that the MEP lies between the initial and final states, we begin by depicting a linear band connecting these states. This linear band is essentially a trial path, punctuated by multiple equidistant points known as images, depicted in Figure x. Each image represents an intermediate configuration along the path. The number of images chosen depends on the path's complexity, with 3 to 7 images typically proving sufficient for most materials. However, a straightforward interpolation of atomic positions between initial and final images can yield positions far removed from the MEP. This leads to heightened atomic forces and convergence challenges, necessitating manual adjustments to bring the images closer to the MEP (Lee, 2016).

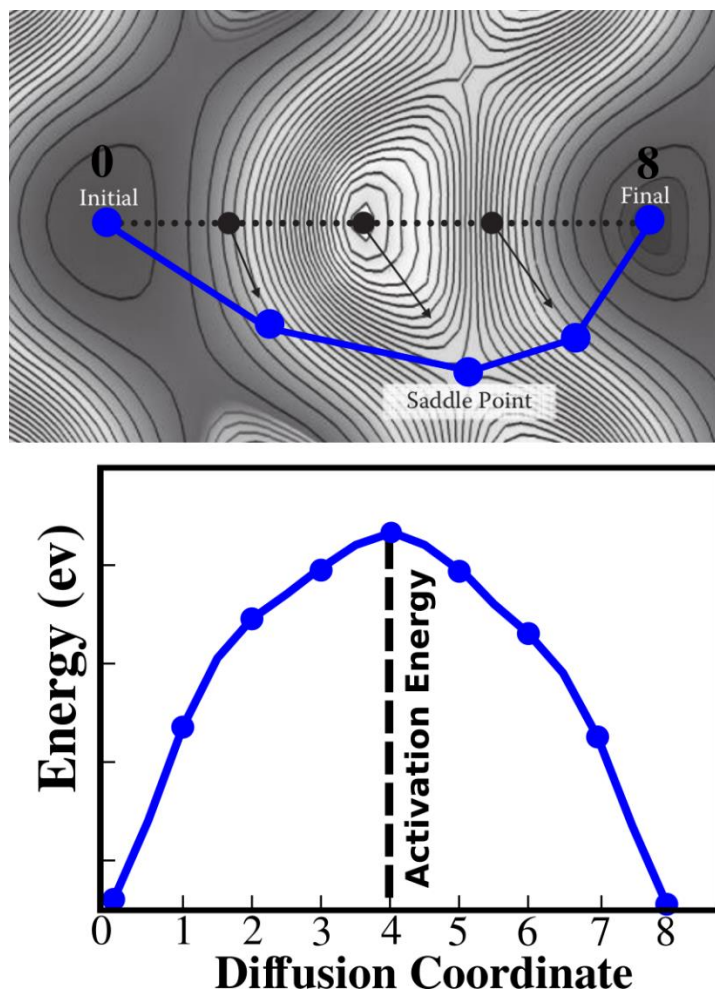


Figure 2.3. a) Principle of NEB method showing the initial position of intermediate images, nudging toward the minimum energy path. b) Digram showing how to calculate the activation energy from images energy.

The journey to uncover the MEP involves gradually adjusting the initial band towards configurations with zero net forces. To ensure controlled band adjustments and maintain uniform spacing between images, a theoretical spring force is applied to each image, directed parallel to the band. This orchestration guides each image toward a configuration where atomic forces balance, akin to a caravan navigating sand dunes.

The NEB approach leverages force projection – rather than energy – to steer images towards the MEP, encompassing saddle points along the path. Each image on the initial band experiences the composite impact of two forces: spring forces and interatomic forces. To steer the band toward the MEP, only the component of spring forces projected along the band's local tangent and interatomic forces projected perpendicular to the band are considered. By excluding other force components,

images along the linear path gradually shift towards the MEP path. With each nudged configuration, standard Density Functional Theory (DFT) calculations are performed to reach electronic equilibrium, and atomic forces are calculated to determine the optimal directions for further adjustments. This iterative process continues until atomic forces converge to a predetermined small value close to zero, signifying alignment with the MEP (Henkelman et al, 2000).

2.2.5. Ionic diffusion prediction

Ionic diffusion is the movement of ions through a solid-state material due to concentration gradients. It plays a critical role in many electrochemical processes, such as batteries and fuel cells. Computational methods (DFT) have been widely used to study ionic diffusion in materials (Elbaz et al, 2020).

In DFT, the total energy of a system is calculated based on the electron density of the system, which is determined by the electronic wavefunction. This allows for the calculation of various properties related to the atomic and electronic structure of materials, including diffusion coefficients. One common approach to calculating diffusion coefficients in DFT is the nudged elastic band (NEB) method (Henkelman et al, 2000).

The NEB method involves calculating the minimum energy pathway (MEP) between two points on an energy surface, in this case, the positions of the ions in the material. The MEP is calculated using a series of images, or intermediate structures, that are placed between the initial and final points. The energy and forces acting on each image are calculated using DFT, and the images are then optimized along the MEP until the diffusion barrier, or activation energy, is minimized.

The diffusion coefficient can then be calculated using the Arrhenius equation:

$$D = D_0 \exp(-E_a/RT) \quad (2.26)$$

where D_0 is a pre-exponential factor, E_a is the activation energy or diffusion barrier, R is the gas constant, and T is the temperature (Sagotra et al, 2019).

Here, we used the NEB method to investigate Li-ion diffusion in LATP bulk, as a solid electrolyte for ASSBs.

2.2.6. The slab creation

A slab, in the context of computational surface calculations, refers to a two-dimensional representation of a surface within a three-dimensional periodic crystal lattice.

Creating a slab from a bulk crystal structure involves selecting a specific Miller plane and adjusting the vacuum spacing. First, choose the bulk crystal structure of a certain material (Figure 2.4.a). After building a super cell in the 3 dimensions (Figure 2.4.b), identify the required surface plane by Miller indices (k h l), defining the orientation of the crystal surface relative to the lattice (Figure 2.4.c). Create a new bulk structure with the chosen Miller plane using crystallographic software (in our work we used VESTA (Momma & Izumi, 2011)). Next, generate a supercell by replicating the new bulk structure along the z-lattice vectors. Cleaving atoms from one side of the new bulk structure within the supercell creates the slab surface with the desired orientation. then we added a sufficient vacuum layer to prevent interactions between periodic slabs (Figure 2.4.d).The slab model can be used for various computational surface calculations, offering insights into surface properties, reactions, and interactions, with applications in fields like catalysis and materials design.

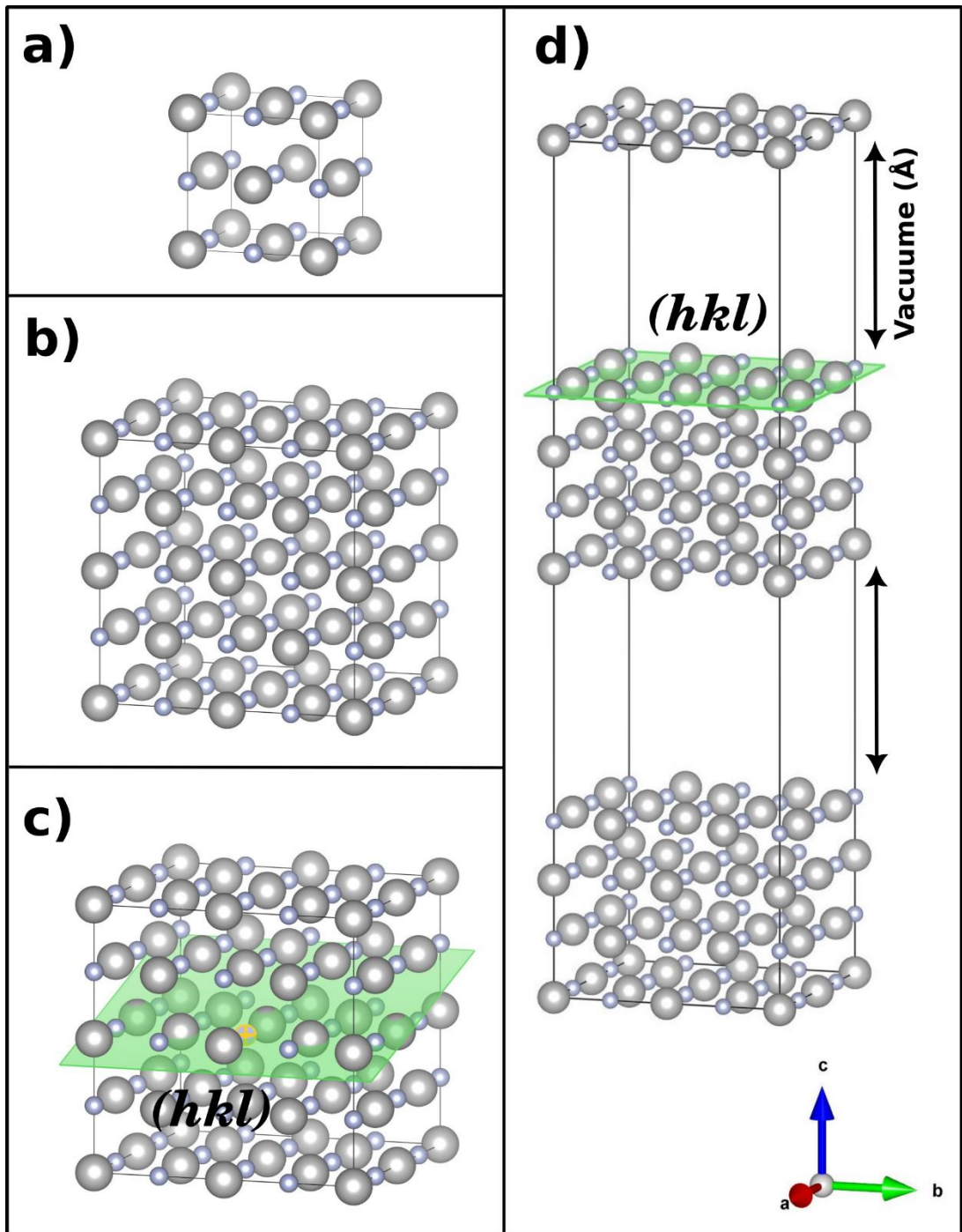


Figure 2.4. Illustration diagram of the given material, depicting (a) the bulk structure, (b) the supercell configuration, (c) specific Miller indices (hkl) , and (d) the constructed slab model.

2.2.7. Surface termination

Exploring the optimal surface structure presents a formidable challenge due to the multifaceted nature of slab configurations, each composed of multiple atomic layers. Each individual layer can signify a distinct termination. The task at hand involves discerning the viable termination candidates. In this context, a taxonomy of termination types, attainable through the cleavage of slabs, is outlined (X. Tian et al, 2018).

2.2.7.1. Symmetric and stoichiometric termination

Derived from bulk crystalline material, these slabs exhibit uniform atomic orientation within the z-axis atomic layers. Equidistant spacing between adjacent atomic strata is maintained (depicted in Figure 2.5). Notably, all cleavage planes yield identical terminations. Consequently, the computation of surface energy follows a straightforward route, adhering to the conventional approach stipulated by Equation (2.23)

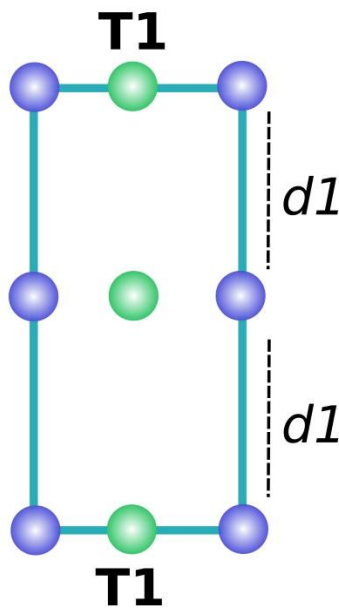


Figure 2.5. Illustration diagram Showing a slab with symmetric and stoichiometric termination of the given material.

2.2.7.2. Symmetric and non-stoichiometric termination

Slabs stemming from bulk cells manifest multiple z-axis atomic orientations concurrently while maintaining uniform interlayer distances (as illustrated in Figure 2.6.). In this scenario, the number of atomic layers corresponds to the number of terminations post cleavage (e.g., in Figure 2.6. b-c), a dual-layer slab encompasses purple and green atomic layers, engendering T1 and T2 terminations).

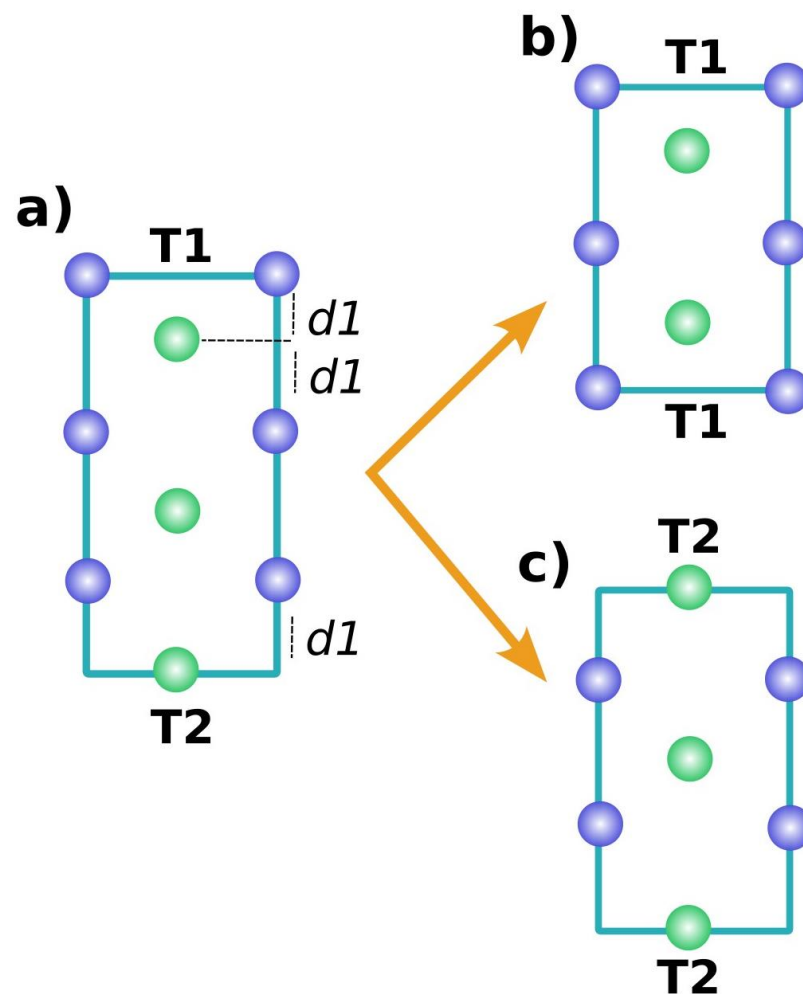


Figure 2.6. Illustration diagram Showing a slab with symmetric and non-stoichiometric terminations of the given material.

Surface energy is intrinsically composed of cleavage energy (E_{cle}) and relaxation energy (E_{rel}). The aggregate surface energy amalgamates E_{cle} and E_{rel}

$$E_{\text{surface}} = (E_{\text{cle}} + E_{\text{rel}})/A \quad (2.27)$$

The act of cleaving the bulk simultaneously yields two distinct terminations, each sharing an equitable division of cleavage energy. Consequently, the cleavage energies of terminations resulting from a single cleave event are deemed equal. Thus, for a stoichiometric slab, E_{cle} can be ascertained from the formula:

$$E_{\text{clv}} = (E_{\text{unrelax}} + nE_{\text{bulk}})/2 \quad (2.28)$$

Here, E_{unrelax} signifies the aggregate energy of the unrelaxed surface slab. In the context of a symmetric slab (showed in Figure 2.6. a-c), E_{rel} can be directly deduced from the equation:

$$E_{\text{rel}} = (E_{\text{total}} + nE_{\text{unrelax}})/2 \quad (2.29)$$

2.2.7.3. Asymmetric and non-stoichiometric termination

Incorporating additional complexities, this category of slabs demonstrates multiple z-axis atomic orientations alongside disparate interlayer spacings (as presented in Figure 2.7). Notably, although terminations conclude with identical atomic species (e.g., T1 and T2 in Figure 2.7.b), the intervals between said terminations and their adjacent atomic strata vary (e.g., d_1 for T1 and d_2 for T2). In consequence, a diverse array of non-stoichiometric terminations emerges post cleavage.

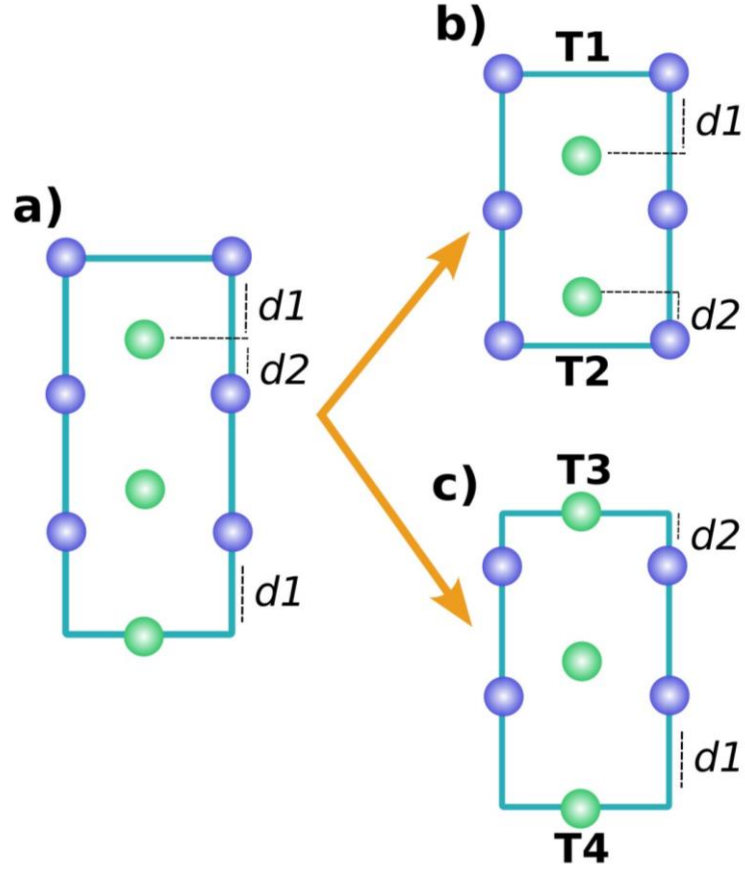


Figure 2.7. Illustration diagram Showing a slab with asymmetric and non-stoichiometric terminations of the given material.

Quantifying the relaxation energy of upper and lower terminations for these asymmetric slabs proves intricate and necessitates a bespoke approach. The relaxation energy of terminations such as T1 or T2 can be inferred from the following expressions:

$$E_{\text{rel(T1)}} = E_{\text{T1-rel}} + E_{\text{unrelax}} \quad (2.30)$$

and

$$E_{\text{rel(T2)}} = E_{\text{T2-rel}} + E_{\text{unrelax}} \quad (2.31)$$

Here, $E_{\text{T1-rel}}$ and $E_{\text{T2-rel}}$ signify the energy levels of slabs with exclusively the upper or lower halves relaxed, respectively.

To ensure precision, the relaxed segment must exhibit sufficient thickness to mitigate potential inaccuracies. Through the integration of computed relaxation and cleavage energies for each termination, surface energies can be ascertained using the equation (2.27), as predicated on the aforementioned considerations.

2.3. Computational Details

2.3.1. LATP

All calculations were performed using the Vienna Ab-initio Simulation Package (VASP) code based on density functional theory (DFT) (Kresse, 1993; Kresse, 1996a; Kresse, 1996b). For both bare LATP and S@LATP, a plane wave basis set with an energy cut-off of 520 eV and projector augmented wave (PAW) pseudopotentials were utilized. The exchange-correlation functional was described using the generalized-gradient approximation (GGA) with the Perdew-Burke-Ernzerhof (PBE) parametrization (Perdew et al, 1996). To sample the Brillouin zone, Monkhorst-Pack scheme with $4 \times 4 \times 2$ k-points and the Gaussian smearing model with $\text{SIGMA} = 0.05$ eV were employed.

The LATP unit cell, consisting of 110 atoms, was fully relaxed until the force on each ion and energy difference in subsequent iterations were less than $0.01 \text{ eV } \text{\AA}^{-1}$ and 10^{-6} eV, respectively. The migration barrier energy for the Li^+ diffusion path in both bare and sulfur-doped LATP was calculated using the climbing-image nudged elastic band (CI-NEB) method (Henkelman, 2000; JÓNSSON, 1998).

For Density of States (DOS) calculations, a denser k-point grid of $11 \times 11 \times 1$ was used. In addition to the GGA method, Hubbard U corrections were incorporated into the exchange-correlation potential (GGA+U) to explore crystal geometric relaxation and band structure calculations. Various values of Hubbard U (2, 3, and 4 eV) were tested for the Ti-3d orbital (Anisimov, 1991; Liechtenstein, 1995).

Bader charge analysis was utilized to analyze the effective net charge on each atom in the diffusion path (Bader, 1991).

Finally, visualizations of the structures were generated using VESTA, and spin-polarized calculations were included in the electronic structure computations.

2.3.2. TiMn₂

The Vienna Ab initio Simulation Package (VASP), employing pseudopotentials for Ti (3p4s3d) and Mn (3p4s3d), was utilized in this study. The exchange-correlation interaction functional used was the Perdew-Burke-Ernzerhof (PBE) functional, a generalized gradient approximation (GGA) (Perdew et al, 1996).

A cutoff energy of 520 eV was found to yield convergence. For bulk calculations, the Fermi surface smearing was implemented using the tetrahedron method with a width of 0.01 eV. The Brillouin zone was sampled using the Gamma-centered Monkhorst-Pack scheme with KSPACING = 0.4, generating k-point grids.

Surface calculations were conducted using a 2x2 supercell with a slab thickness of 19 atomic layers. To achieve convergent surface energies, the density of gamma k-point was set to 4x4x1. The bottom 10 layers of the slab (approximately 0.3 nm thick) were kept fixed, while the remaining 9 top layers were allowed to relax freely. All calculations were performed at constant volume, and a 28 Å vacuum region was included in the slab model to avoid interactions between layers in the normal direction.

The stability of the surface was evaluated by considering the surface energy, where lower surface energy indicates greater stability (Y.-H. Zhao et al, 2012). For Density of States (DOS) calculations, a KSPACING of 0.1 was used.

2.3.3. MnO₂

The electronic structure calculations were performed utilizing the Vienna Ab initio Simulation Package (VASP). The investigation treated the electron XC interactions using the GGA+U, the SCAN, and the SCAN+U functionals (Sun et al, 2015).

For GGA+U and SCAN+U calculations, Hubbard U correction, as proposed by Dudarev et al. (1998) was applied. The U values were examined for Mn 3d orbital. U values were set as 2.5, 3, 3.5, 4, and 4.5 eV.

To ensure computational convergence, a cutoff energy of 520 eV was chosen for bulk calculations from converge test. The Fermi surface smearing was achieved via the tetrahedron method with a width of 0.01 eV. The Brillouin zone was sampled utilizing the Gamma-centered Monkhorst-Pack scheme with KSPACING = 0.4, generating k-point grids.

The investigation of surfaces was carried out using a 10.4*11.6 (for a and b direction) slab comprising 22 atomic layers. An 18 Å vacuum was set to avoid interactions between the layers in the z-direction. Convergent surface energies were attained by using a Monkhorst k-point density of 4x4x1. During the relaxation process, the bottom 10 layers of the slab were constrained, while the remaining 12 top layers were allowed to relax freely.

3. RESULTS AND SUGGESTIONS

3.1. LiAlTi(PO₃)₄ as a Solid Electrolyte

3.1.1. Structure stability

The NASICON-type LiAlTi(PO₃)₄ (LATP) structure comprises a three-dimensional (3D) framework constructed of [MO₆] octahedra (where M represents the 12c Wyckoff position, occupied by Al and Ti), [PO₄] tetrahedra, and [LiO₆] octahedra, as illustrated in Figure 3.1.a. The LATP crystal structure adopts a rhombohedral symmetry with a space group of R-3c (Arbi et al, 2002). The (6b) Wyckoff positions within the structure are occupied by Li ions, indicated in Figure 3.1.b, with a light green color, while there are two additional Wyckoff positions, 18e and 36f, that can be occupied by Li ions. The 18e position is positioned midway between two 6b positions, and two of the 36f positions are situated between the 18e and 6b positions, as demonstrated in Figure 1.1.d., (Rossbach et al, 2018). In our model, Li_{1+x}Ti_{2-x}Al_x(PO₄)₃, with x=0.33, two Ti atoms in the original LiTi₂(PO₄)₃ (LTP) crystal structure are replaced with Al atoms. The optimal Al/Ti substitution configuration was selected based on a prior study reported in the literature (B. Zhang et al, 2020). To compensate for the charge of the framework, two additional Li⁺ ions are introduced into the unit cell, occupying two different 18e Wyckoff positions along the chosen diffusion pathway, as shown in Figure 3.1.b.

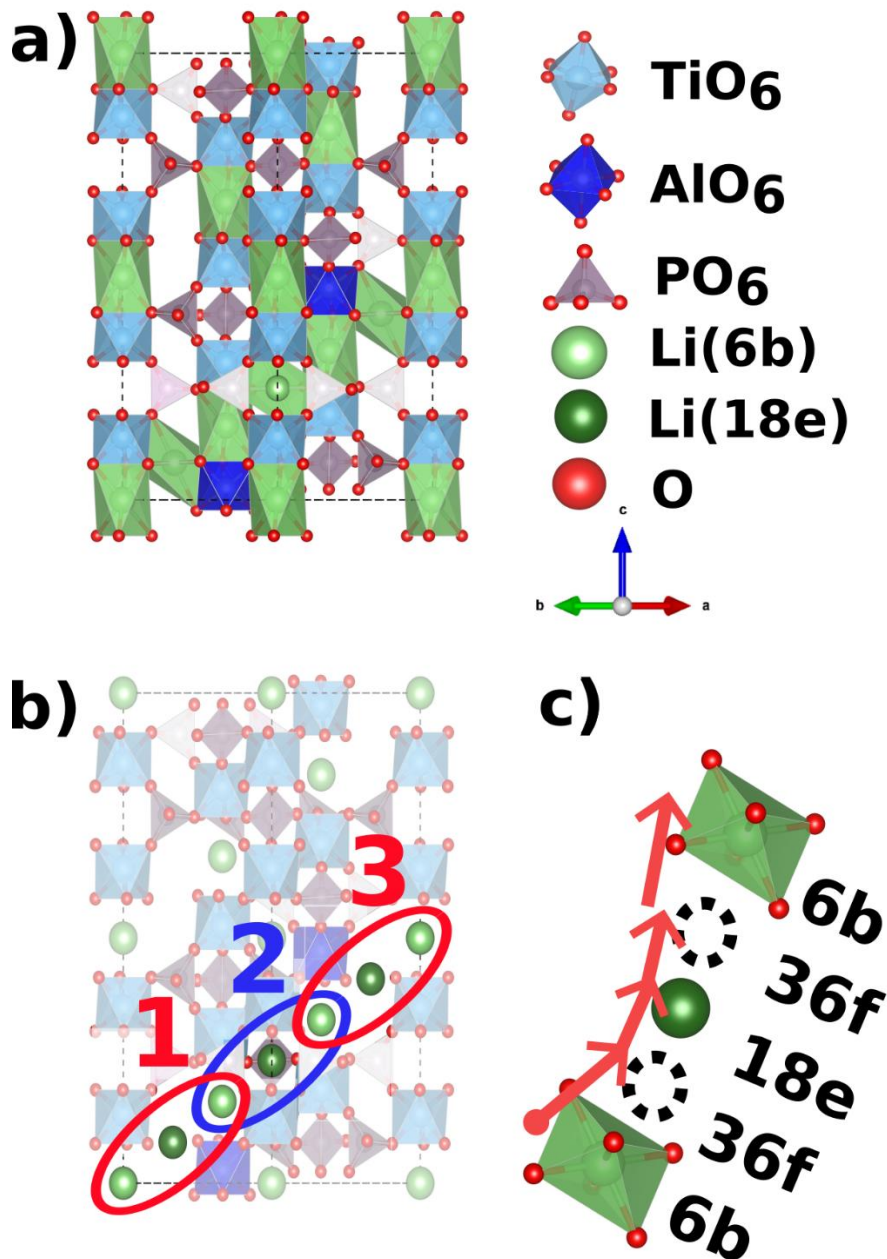


Figure 3.1. (a) The skeleton of (LATP) depicts its crystal structure. (b) The migration path of Li ions within the LATP structure. (c) the 6b, 36f, and 18e Wyckoff positions within the LATP crystal lattice.

To simulate the effects of sulfur substitution, one oxygen atom out of a total of 72 is replaced with sulfur, as reported in our previous experimental study (Kızılaslan et al, 2020). Based on the hexagonal crystal symmetry and atomic environment of the LATP structure, four possible substitution configurations can be obtained, namely S0: bare LATP, S1: LiO₆-AlO₆-PO₄, S2: TiO₆-PO₄, S3: LiO₆-TiO₆-PO₄, and S4: AlO₆-PO₄, as illustrated in Figure 3.2.c. It is important to note that all substitutions

occur within the first and second neighbors of the Li-ion diffusion pathway, as depicted in Figure 3.2.

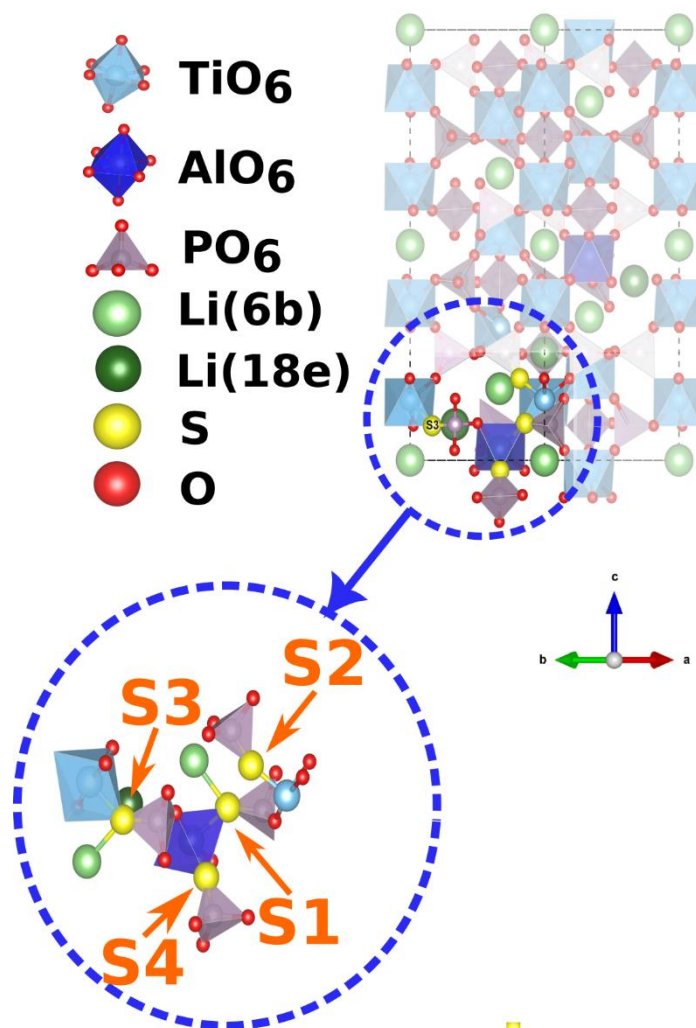


Figure 3.2. The substitution of O atoms with S atoms in the LATP lattice.

To investigate the impact of sulfur doping on the stability of LATP, we first examined the energy perspective. Since all configurations involve the substitution of only a single sulfur atom, we compared the total energies of the doped structures to the original system, rather than the formation energy. Regardless of the configuration, sulfur doping resulted in a decrease in the stability of the structure from the energy perspective, which can be attributed to the stronger affinity of metal ions to oxygen compared to sulfur atoms. Table 1 summarizes the calculated total energies of all the sulfur-doped configurations, with S3 exhibiting the highest stability among them.

Furthermore, the structural optimization of the bare and sulfur-doped LATP was conducted by fully relaxing the lattice and atomic positions. The results, presented in Table 3.1., demonstrate that all configurations result in increased lattice parameters and unit cell volume due to the larger ionic radius of sulfur relative to oxygen (184 pm for S and 140 pm for oxygen).

Table 3.1. Lattice constants (a, b and c), volume (V), and the total energy (E_{tot}) for bare and sulfur doped LATP unit cell.

Structures	Lattice Parameter		Volume (\AA^3)	Etot (eV)
	a=b (\AA)	c (\AA)		
S0	8.62	21.05	21.05	-831.28
S1	8.64	21.29	21.29	-823.26
S2	8.26	21.35	21.35	-826.46
S3	8.63, 8.7	21.18	21.18	-826.92
S4	8.64	21.45	21.45	-826.82

It has been observed that the sulfur substitution changed the atomic bond lengths in the vicinity of the Li diffusion path. The bond lengths were compared before and after S atom substitution. From Figure 3.3. It is seen that bond length shows a similar tendency to changes in lattice parameters. From the observation, it can be said that the bond lengths are also responsible for the change of lattice parameters unit cell volume. The effect of S substitution on the bond length is also summarized in Table 3.2.

Table 3.2. Comparing the bond length (in Å) in the first and second regions between LATP (S0) and Sulfur doped LATP (S1, S2, S3, and S4).

Bond	S0 (A0)	S1(A0)	S2(A0)	S3(A0)	S4(A0)
A	2.2	2.19	2.29	2.3	2.18
B	2.19	2.12	2.36	2.18	2.2
C	3	2.97	3.16	3.1	2.97
D	2.22	2.39	2.23	2.24	2.44
E	2.99	2.94	3.64	3.16	2.88
F	2.17	2.14	2.26	2.22	2.15
G	2.88	2.85	2.94	2.95	2.84
H	2.96	3.29	3.09	2.96	2.96
K	2.23	2.4	2.34	2.47	2.12
L	2.22	2.4	2.49	2.22	2.2
M	3.01	3.09	3.07	2.98	3.08
N	2.85	3.07
Q	2.93	3.09
I	2.22	2.37

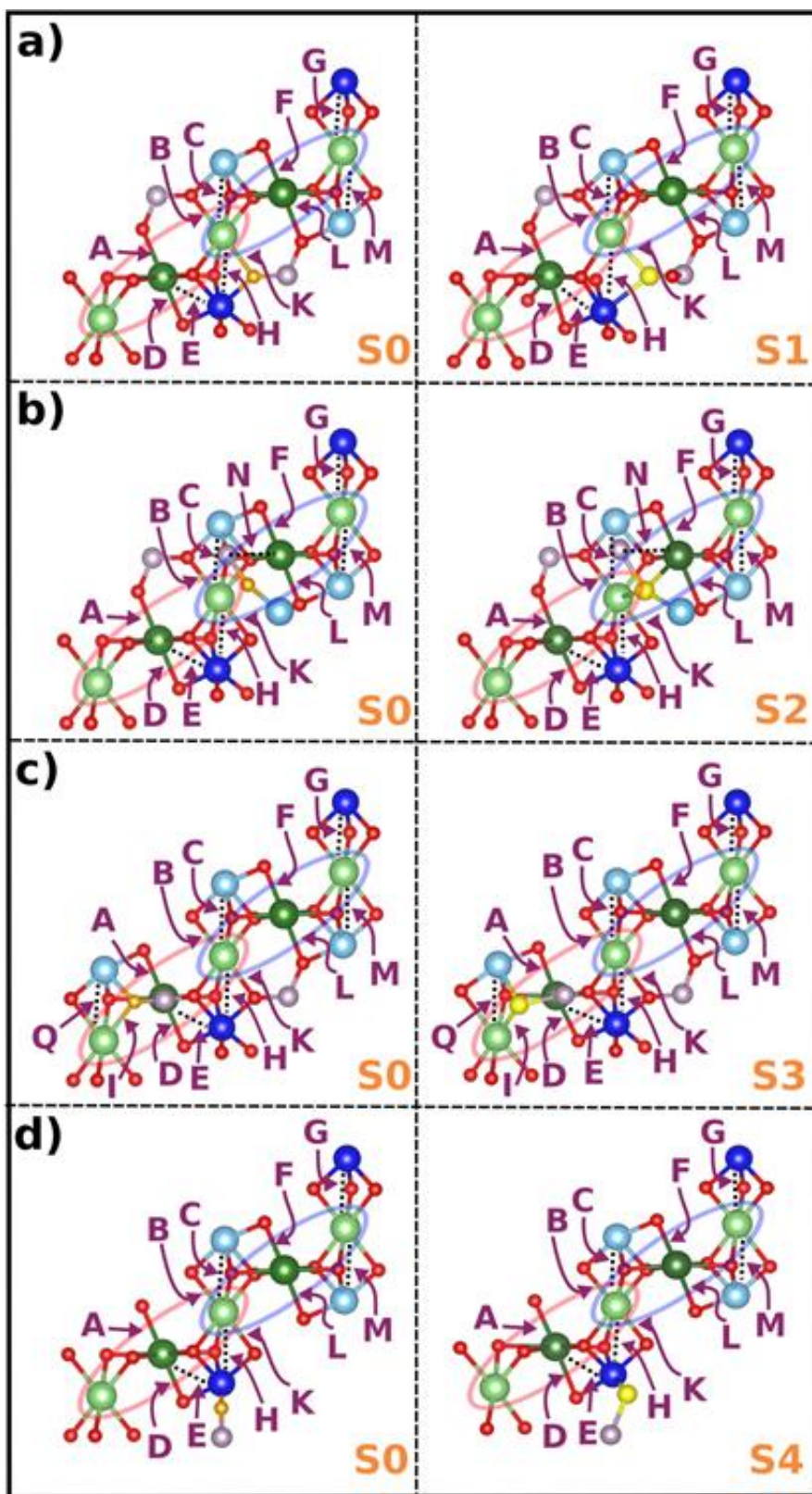


Figure 3.3. The change in the bond lengths of Li-ion in the first and second regions.

3.1.2. Lithium-ion migration profile for bare LATP

The present study investigates the migration of Li-ions in NASICON-type $\text{Li}_{1+x}\text{Ti}_{2-x}\text{Al}_x(\text{PO}_4)_3$ (LATP) material using the climbing image nudged elastic band (CI-NEB) method. The migration path follows the Wyckoff positions 6b-36f-18e-36f-6b, which is divided into three sections denoted as 1, 2 and 3 based on the symmetrized topology of the structure as illustrated in Figure 3.4.a. The Li-ion diffusion energy barrier displays a symmetric curve with an energy barrier of 0.41 eV in the first and third sections. However, the activation energy barrier for the second section shows asymmetry and has a higher barrier attributed to the effect of Al atoms inside the structure. To examine the impact of the position of Al atoms on the activation energy barrier, the atomic site of the Al atoms was relocated closer to the diffusion path, as depicted in Figure 3.4.b, and the barrier for Li ionic movement was measured. It was found that the activation energy barrier was lowered from 0.91 eV to 0.6 eV. This result demonstrates that the position of the Al atoms significantly affects the shape and value of the barrier energy, which is in agreement with previous findings (Kızılaslan et al, 2020).

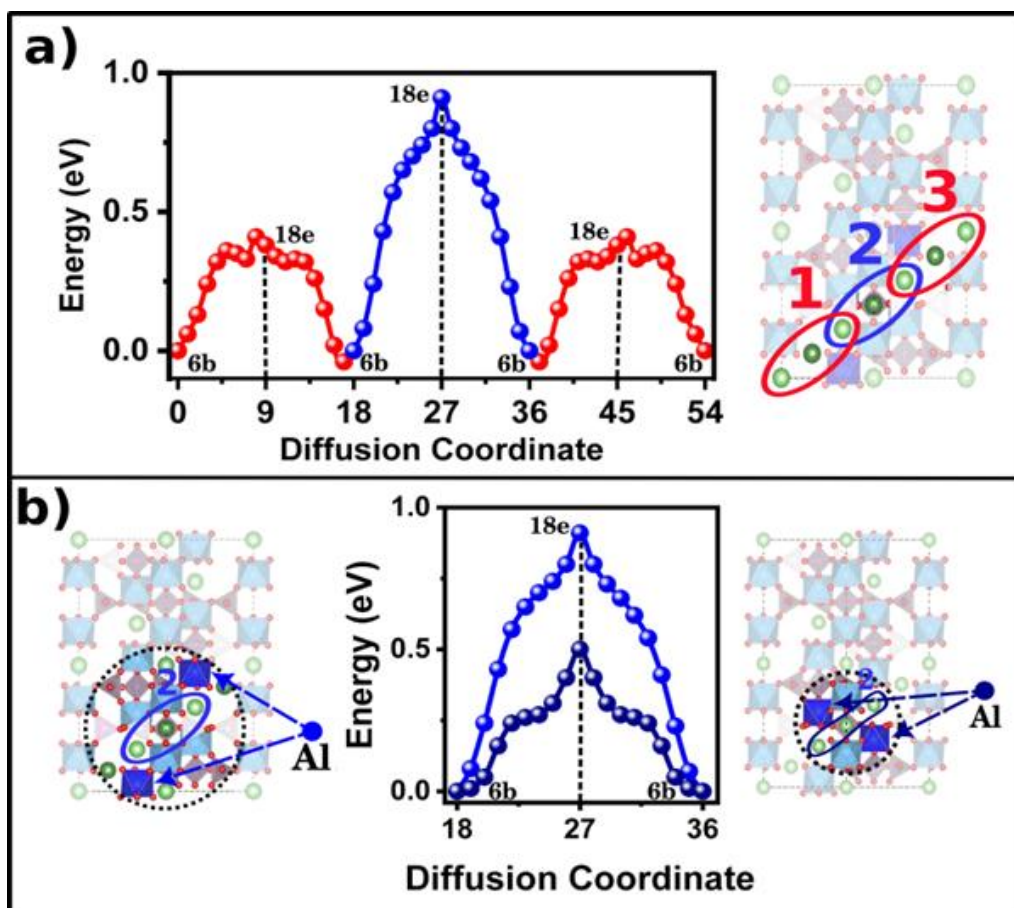


Figure 3.4. (a) Computed activation energy barriers of Li⁺ ion diffusion path along diffusion channels (1., 2., and 3. regions) in bare (LATP). (b) A comparison of the barrier energy in the second region with two different Aluminum (Al) atom positions.

3.1.3. Lithium-ion migration profile for sulfur doped LATP

In this study, we aimed to investigate the effect of sulfur doping on the diffusion profile of lithium ions in (LATP) solid electrolyte. To this end, we performed substitutional doping of oxygen with sulfur atoms, and analyzed the Li-ion diffusion energy barrier. As the atomic environment of the first and third regions in LATP structure is symmetrical, we focused on the diffusion profiles of the first and second regions. Our results revealed that the energy profiles of Li-ion diffusion were greatly influenced by the position of the sulfur atom (S1..S4). The substitution of oxygen with sulfur caused a non-symmetric energy profile along the migration paths, as the substitution only occurred on one side of the diffusion path. Our investigation indicated a significant dependence of the energy profile on the sulfur sites in LATP structure. We depicted the Li-ion migration activation energy barrier of S@LATP in the first and second regions in Figure 3.4. and Figure 3.5. Notably, we observed a

substantial decrease in the activation energy barrier when the Li-ion passed through the vicinity of the sulfur atom, as depicted in Figure 3.5. (a-c). We explained this phenomenon by the difference in the electronegativities of oxygen and sulfur. As sulfur has a lower electronegativity than oxygen, it pulls electrons less, resulting in less partial negative charge around sulfur atoms. Consequently, the Coulombic attraction between sulfur and lithium ions is smaller, allowing lithium ions to move more freely and reducing the activation energy barrier. However, we did not observe a meaningful change in the activation energy barrier in the S4 structure due to the screening effect of the Al atom. When the sulfur atom locates behind the Al atom, its effect on Li-ion is obscured, as shown in Figure 3.5.d. In the second region, the overall diffusion activation energy barriers were higher than the first region due to the position of the aluminum atoms, as discussed in Figure 3.4.

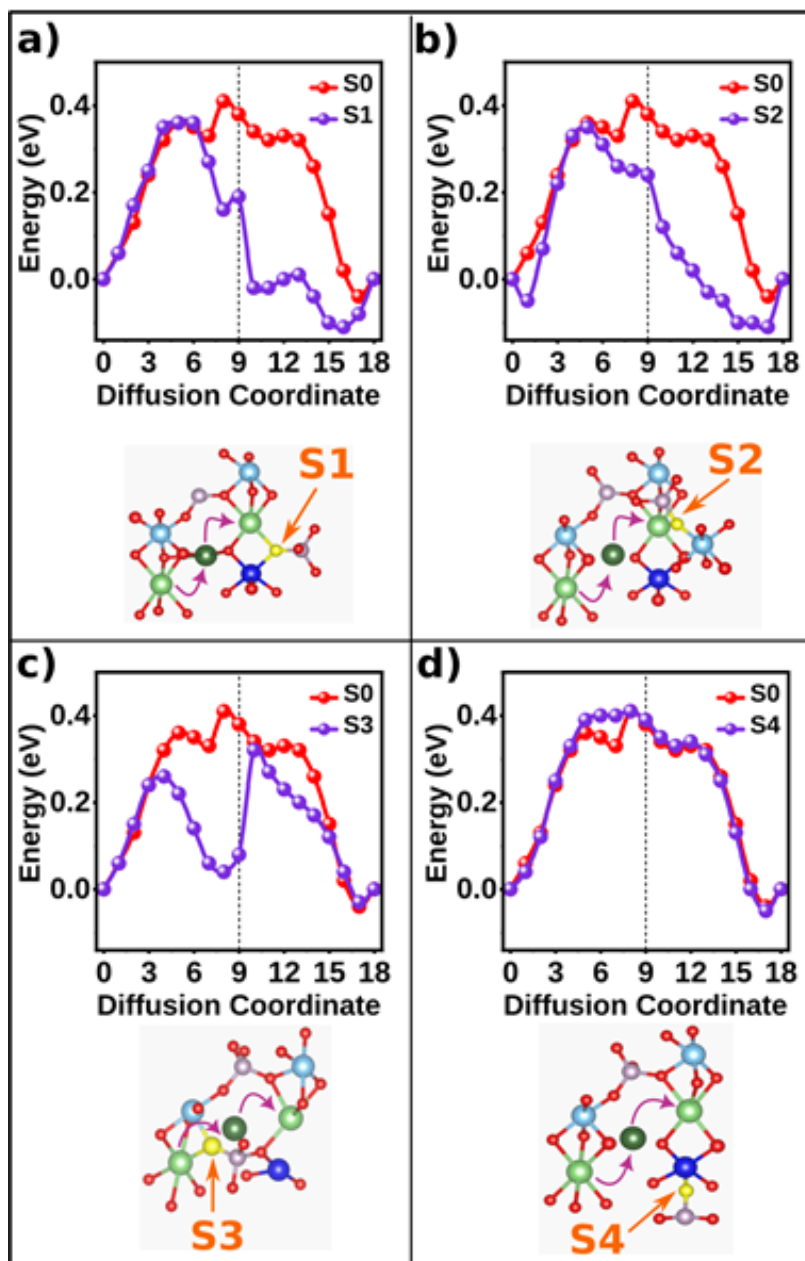


Figure 3.5. Comparison of the energy barriers calculated by NEB for the Li⁺ diffusion in the first region. Bare and sulfur doped LATP are shown by red and purple colours respectively.

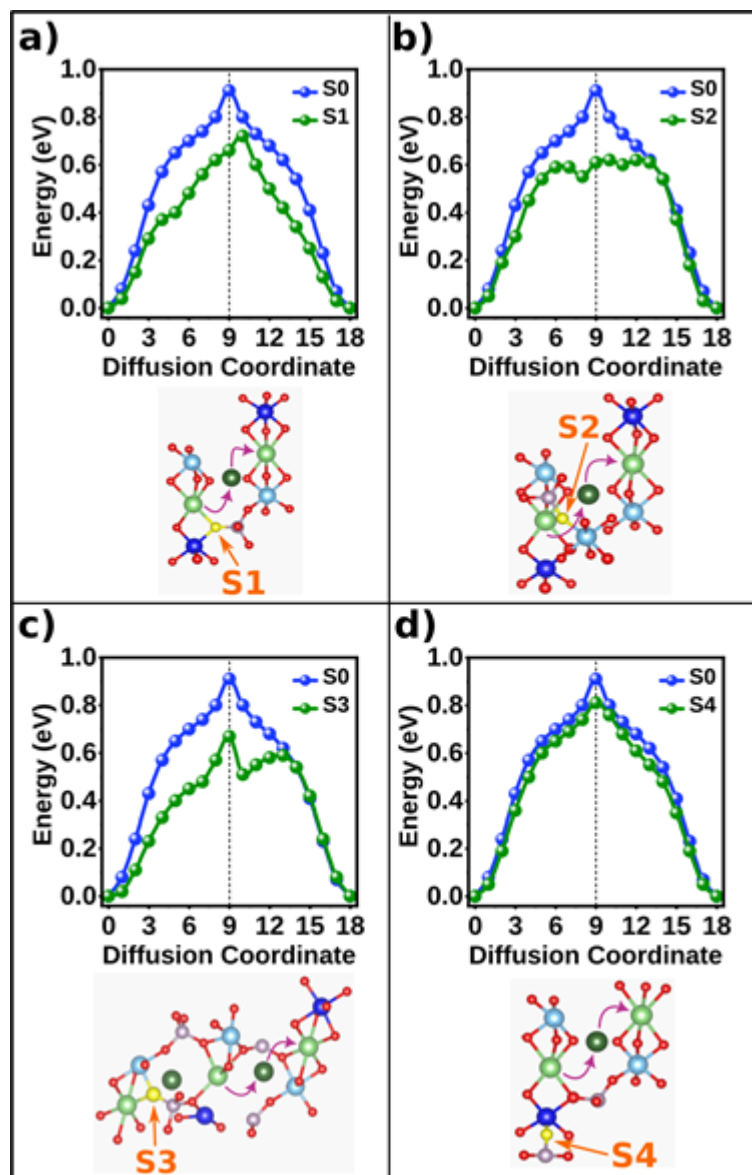


Figure 3.6. Comparison of the energy barriers calculated by NEB for the Li⁺ diffusion in the second region. Bare and sulfur doped LATP are shown by blue and green colours respectively.

3.1.4. Polyhedral volume analysis

In this study, we sought to gain insight into the factors influencing changes in activation energy barriers by examining the alteration in the polyhedral volumes of the atoms near the diffusion path. Our results revealed a clear correlation between the polyhedral volumes and diffusion activation energy barriers. Specifically, we examined the octahedral polygons of LiO₆, where lithium and oxygen atoms occupy the center and corners of the octahedron, respectively, and combined these with the diffusion paths of the first and second regions, as illustrated in Figure 3.7.(a-e). Notably, the path 6b-18e-6b-18e-6b represents the first two regions of the diffusion

path shown in Figure 3.1.b. Further analysis of the relationship between the polyhedral volumes and diffusion activation energy barriers demonstrated that the activation energy barriers decrease in regions where the polyhedral volumes increase. For example, when considering the S1 and S2 atoms, we observed a significant decrease in activation energy barriers in the second (18e) region, where the mobile lithium-ion (18e) moves freely due to the increased Li-O bond lengths. In contrast, for S4, we found no significant variation in polyhedral volumes and similar activation energy barriers along the diffusion path.

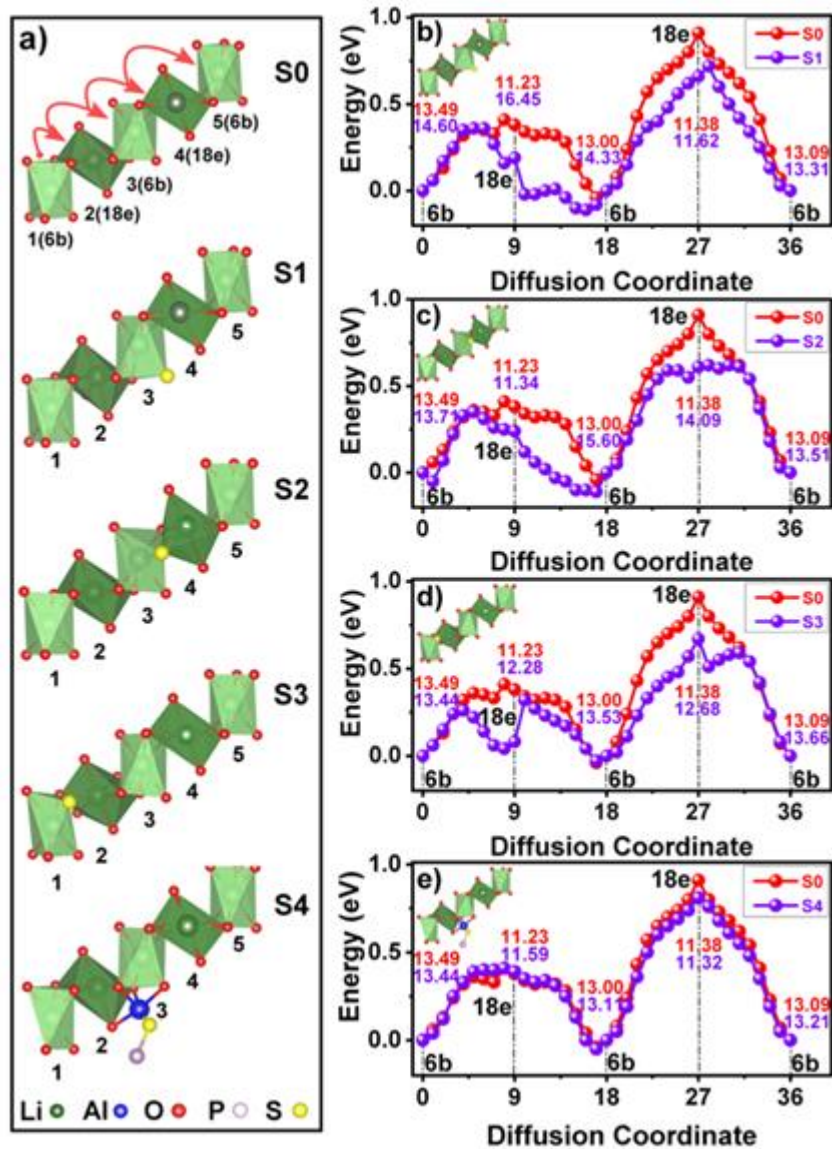


Figure 3.7. (a) The LiO₆ polyhedra in the diffusion path of first and second regions, (b-e) diffusion activation energy barriers along the diffusion paths. Numbers denoted by the red and purple colours are the polyhedral volumes of LiO₆ in the accompanied Wyckoff positions of lithium atoms given in (a).

3.1.5. Electronic state analysis

To investigate the impact of sulfur doping on the electronic state of the electrolyte, we conducted a comprehensive study combining experimental and computational approaches. Solid electrolytes are designed to exhibit insulating properties, thereby preventing potential short circuits within the cell. In the experimental analysis, we recorded the UV-Vis absorbance spectrum to analyze the band gap of the materials.

The band gap was calculated according to the following equation:

$$(\alpha h\nu)^n = K(h\nu - E_g) \quad (3.1)$$

where $h\nu$ is the photoenergy, α is the absorption coefficient, K is a constant relative to the material, and n is either 2 for a direct transition or 1/2 for an indirect transition.

Figure 3.8. (a-b) illustrates the absorbance spectrum and band gap of both bare and sulfur-doped LATP structures. Our findings indicate that the band gap energies for bare and sulfur-doped LATP are 2.35 eV and 2.10 eV, respectively. On the computational side, we utilized the partial density of states (PDOS) to comprehend the role of sulfur doping on the electronic structures of LATP. Bare LATP (S0) exhibited semiconductive behavior, featuring a band gap of 2.30 eV, consistent with previous reports (Tian, 2020; Sohib, 2023). Comparatively, as shown in Figure 3.8.c, sulfur doping leads to a reduction in the band gap. In the most energetically stable configuration, sulfur-doped LATP displays a band gap energy of 1.83 eV. Similar observations of band gap reduction due to sulfur doping have been documented in the literature (Yang, 2020; Shahrokhi., 2020; Xia, 2013). A detailed analysis of the band gap indicates that the conduction band primarily arises from the contribution of Ti-d orbitals, while the valence band originates from the O-p orbitals. The reduction in the band gap can be attributed to the presence of the S-p band within the valence states.

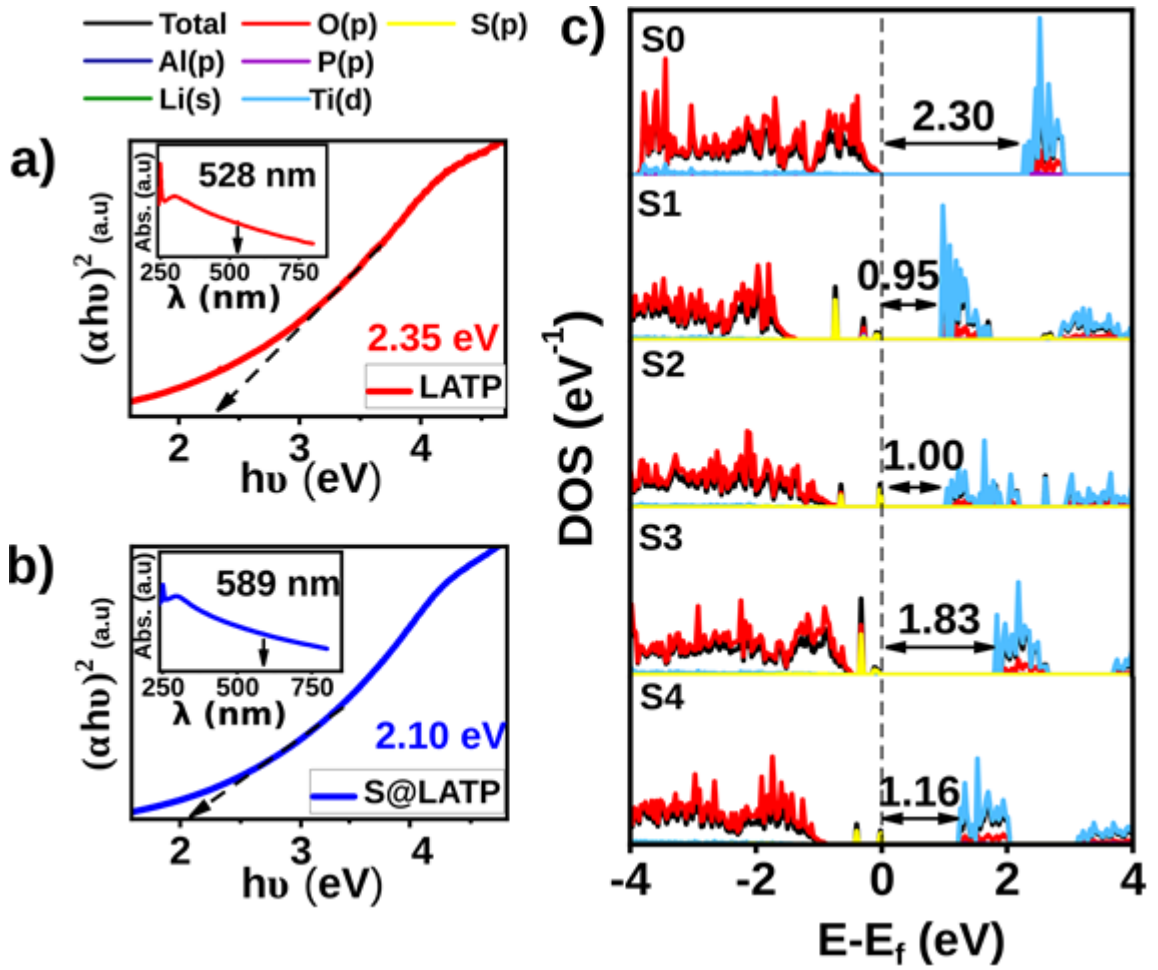


Figure 3.8. $(\alpha h\nu)^2 - h\nu$ curves of the (a) Bare LAMP, (b) S@LAMP and the corresponding absorption spectra in the insets, (c) partial density of states (PDOS) of bare LAMP (S0) and S@LAMP (S1-S4), (d) charge density distributions in bare LAMP and S@LAMP.

Additionally, we conducted a Bader charge distribution analysis, revealing less charge accumulation around sulfur compared to oxygen due to sulfur's lower electronegativity (see table 3.3.). This effect results in a lower net coulombic force on the positively charged lithium ions in sulfur-doped compositions, leading to a reduced activation energy barrier for lithium-ion migration.

Table 3.3. Bader charge values for bare LATP (S0) and S@LATP for the first region.

Structure	Li(6b)	Li(18e)	Li(6b)	Al	Ti	P	O/S
S0	0.9	0.9	0.9	2.52	2.03	3.69	-1.53
S1	0.89	0.9	0.9	2.49	-----	3.09	-0.88
S2	0.9	0.9	0.91	-----	1.95	3.18	-0.79
S3	0.89	0.89	0.89	-----	1.96	3.18	-0.75
S4	0.9	0.9	0.9	2.49	-----	3.18	-0.90

To gain a deeper understanding of the alterations in the chemical environment of (LATP) upon sulfur doping, we conducted computations to determine the Core Level Shift (CLS) values for specific atomic orbitals, namely Li (1s), Al (2p), Ti (2p), P (2p), O (1s), and S (2p). These values are enclosed within parentheses. Figure 9.(a-d) displays a graphical representation of the simulated CLS energies, comparing the unmodified LATP (referred to as S0) with sulfur-doped LATP (referred to as S@LATP), considering different positions of sulfur substitution (S1, S2, S3, and S4).

The degree of CLS is found to be influenced by the position of the sulfur-doped atom. For example, in the case of S1 (depicted in Figure 3.9.a), the CLS energy of P-(2p) ranges from -1.64 eV in S1 to 0.10 eV in S3. Notably, the calculated CLS values for P-(2p) at -1.64 eV align well with the X-ray photoelectron spectroscopy (XPS) binding energy shifts reported in prior investigations (Kızılaslan et al, 2020).

The shift towards lower CL energy in the S/O substitution can be attributed to an increase in the electron density on the P atom (illustrated in Figure 3.9.e), which consequently reduces the attractive electrostatic potential surrounding P (Sohib et al, 2023). This observation is in accordance with the decrease in the Bader charge of the P atom from 3.69 to 3.09 in S0 and S1, respectively (refer to Table 3.3.). Similarly, a negative shift in Ti-(2p) CL energy was observed in S3, with a corresponding decrease in the Bader charge from 2.03 to 1.96 for the Ti atom (as indicated in Table 3.3.). On the other hand, the atoms bonded to S atoms in the S2 and S4 cases did not display significant shifts in CL energy.

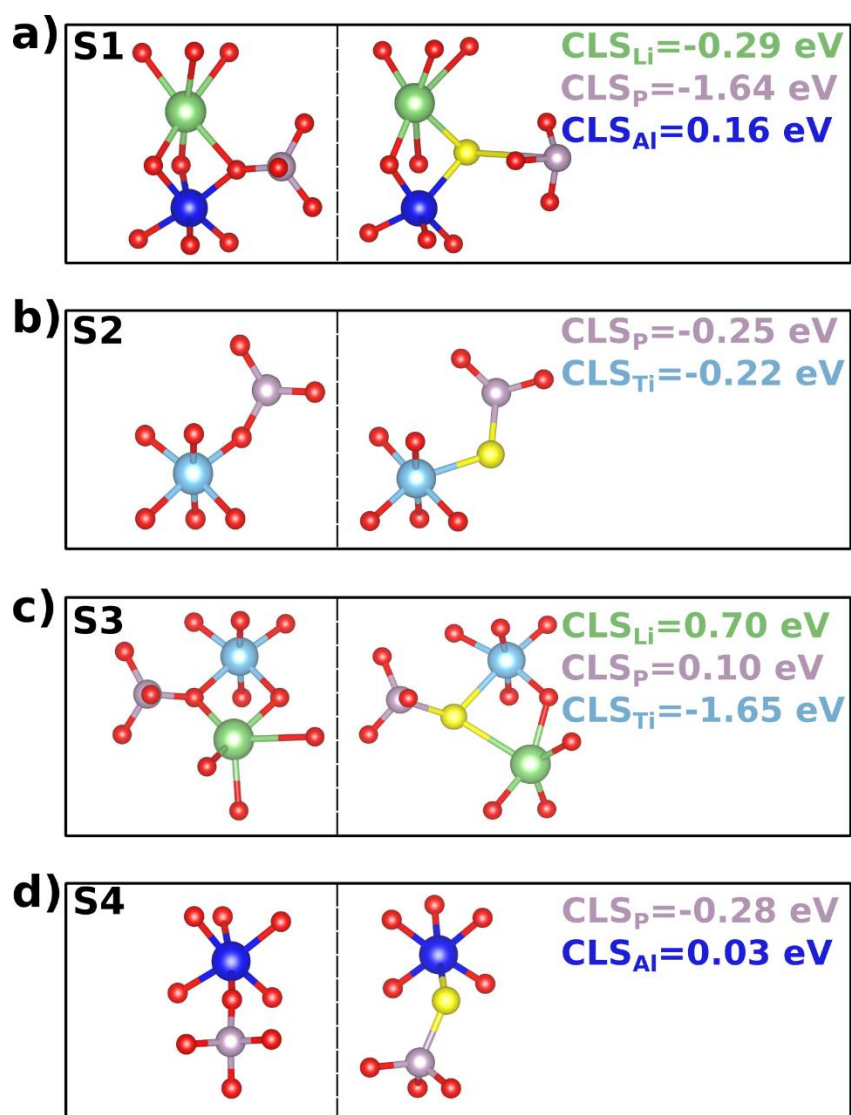


Figure 3.9. (a-d) the core level shift between LATP and S@LATP (S1-S4).

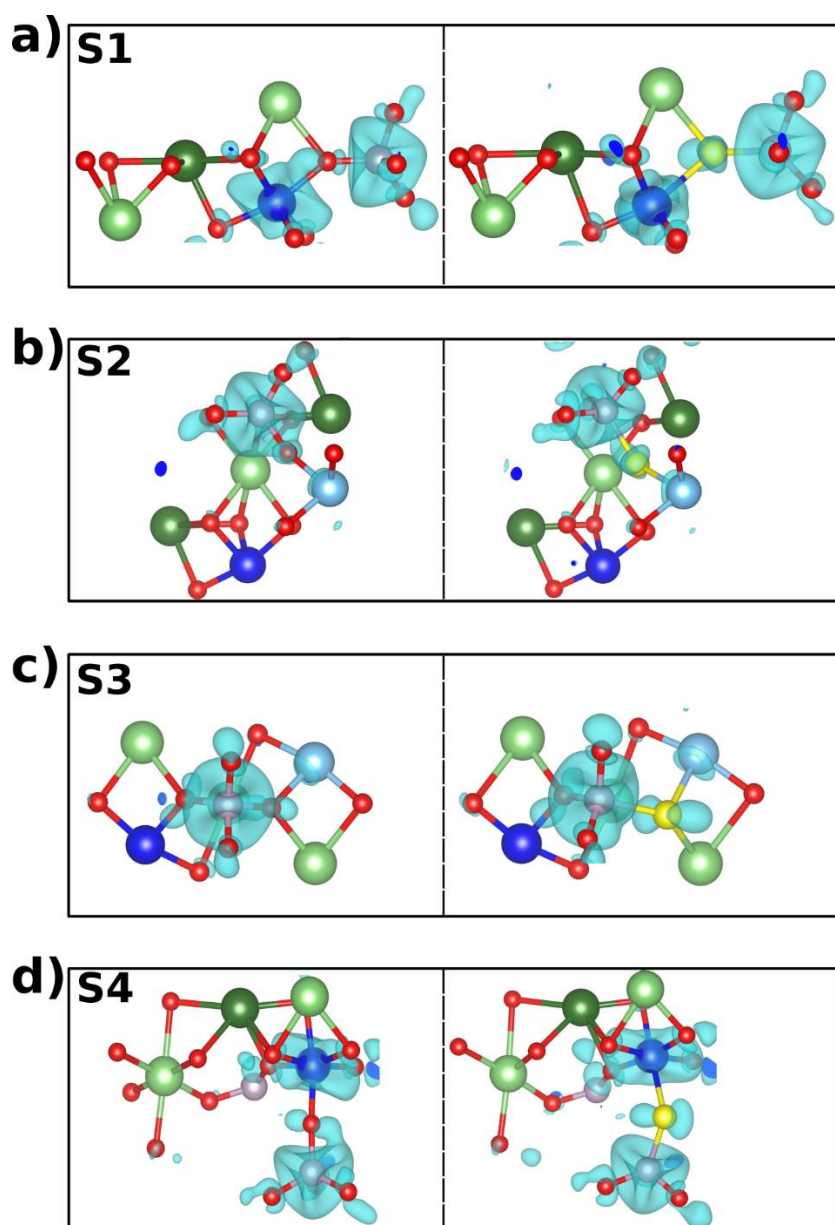


Figure 3.10. (a-d) charge density distributions, between LATP and S@LATP (S1-S4).

3.2. TiMn₂ as a Carbon Free Cathode for Li-O₂ Battery

3.2.1. Bulk and electronic properties

The Laves-phase compounds, characterized by the general formula AB₂, are a highly attractive area of alloys due to their exceptional physical and chemical properties. Typically, the B atom is a transition metal from the 3d, 4d or 5d series, while the A atom is a later member of the 3d series. The B atoms are arranged in a diamond, hexagonal diamond or related structure, with the A atoms forming tetrahedra around the B atoms in the A₂B structure (Nong et al, 2013).

Intermetallic AB₂ compounds can absorb and release large quantities of hydrogen gas, making them highly attractive as negative electrodes in rechargeable batteries due to their reversible absorption and desorption in combination with large storage capacity (Zhu, et al, 2015).

The TiMn₂ compound, which is a C14 type Laves phase, has a hexagonal crystal structure with space group P6₃/mmc, as shown in Figure 3.11.a. The lattice parameters were determined using GGA and found to be a=b=4.724 Å and c=7.84080 Å. The TiMn₂ compound exhibits metallic properties, with a band gap of 0 eV, as shown in Figure 3.11.c. The band structure of TiMnO₃ was characterized using Density of States (DOS) and Projected Density of States (PDOS). The Fermi level was chosen as the reference point, set at 0 eV. In the detailed analysis of the band gap, we find that both Ti and Mn orbitals significantly contribute to the conduction band (CB) and valence band (VB) of the material (Figure 3.11.c).

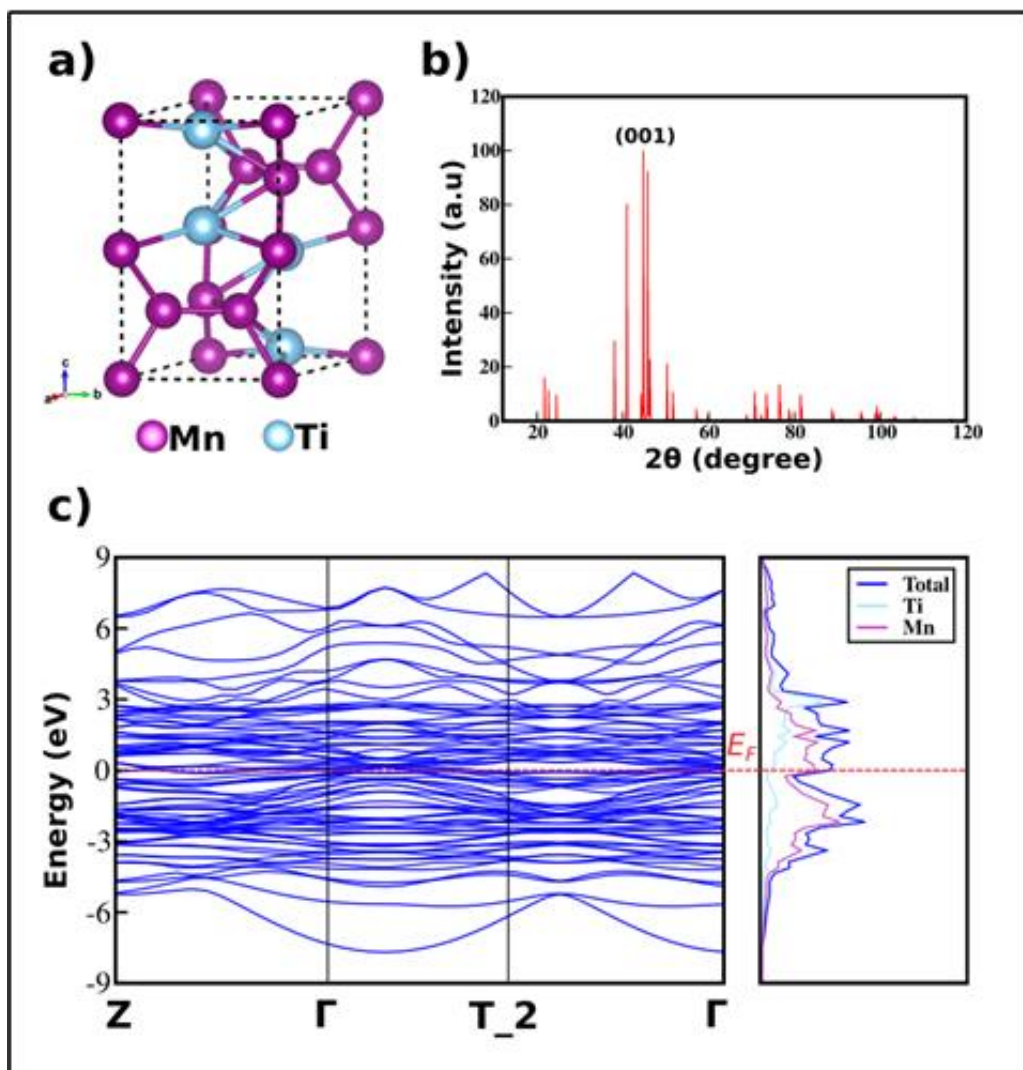


Figure 3.11. a) The crystal structure of TiMn₂, b) Simulated X-ray diffraction (XRD) pattern of TiMn₂ c) Band structure and partial density of states (PDOS) analysis for TiMn₂.

3.2.2. Surface stability of TiMn₂

The simulated XRD pattern of TiMn₂ is displayed in Figure 3.11.b. It is observed that all characteristic peaks, (0 0 1) and (1 1 2) at 44.75° and 45.8°, respectively, exhibit high crystallinity and are indexed to the hexagonal crystal structure of 6₃/mmc space group.

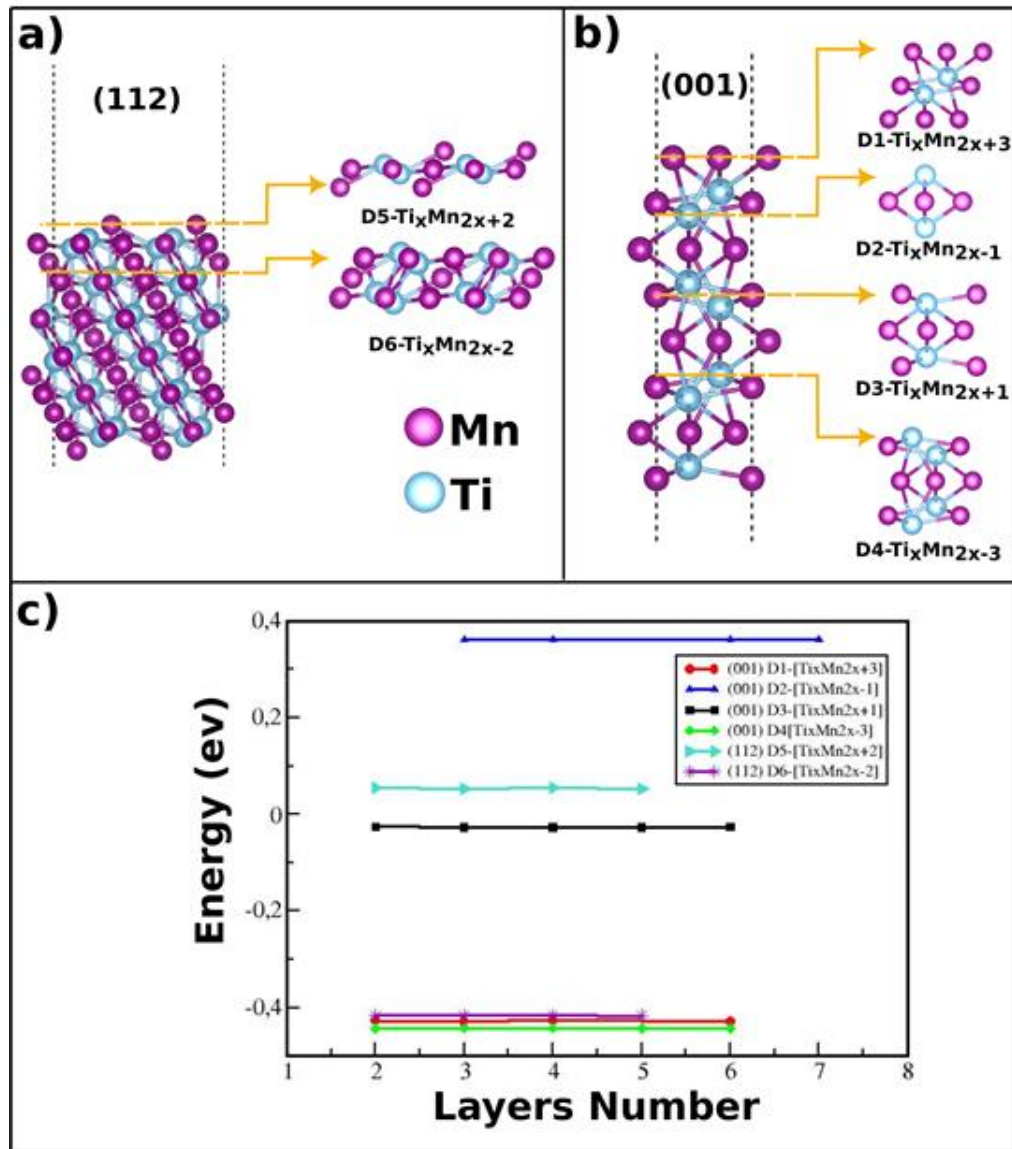


Figure 3.12. a) The (112) surface plane of TiMn₂ with two different terminations, b) the (001) surface plane of TiMn₂ with four different terminations c) Surface energy comparison of all terminations as a function of the number of layers in the TiMn₂ crystal.

For the present study, the supercell models were built by means of periodic repetitions of the hexagonal unit cell exposing two different planes (0 0 1) and (1 1 2). The (0 0 1) model is comprised of four different atomic terminations. We referred to this plane as (D1-D4) as shown in Figure 3.10.b. In the (1 1 2) model, the surface plane was terminated with only two different atomic terminations. We refer to these terminations as (D5 and D6) in the text to follow as illustrated in Figure 3.12.a. The D1 termination had 3 Mn atoms for one unit cell slab. Similarly, the (D2, D3, D4, D5 and D6) termination had (1 Ti, 1 Mn, 1 Ti, 2Mn and 4Ti & 6Mn) atoms respectively.

To figure out which termination has the most stability, surface energy calculations were carried out. Since both (0 0 1) and (1 1 2) plans exhibit an unsymmetric slab, the surface energy was calculated as a function of the atomic layer as suggested by Boettger (Boettger, 1994).

$$E_{Surface}(n) = 1/2[E_{slab}(N) - NE_{bulk}] \quad (3.2)$$

For each slab, layers thickness N, pick as the bulk energy E_{bulk} the differential increase in the slab total energy upon the addition of one layer of material. This formula has the obvious merit of using only slab-related quantities, making no reference to separately calculated bulk energies.

The calculated adsorption energy is presented in Figure 3.12.c. Figure 3.12.c. shows (D1, D4 and D6) have a converged stable energy value compared with the other terminations. D4 within (0 0 1) was the most stable termination.

3.2.3. ORR/OER mechanism

According to recent research, depending on the nature of the cathode material, there are two possible paths for the ORR process and the formation of the final product of the discharge process (Li_2O_2): Adsorption of Li (a) or O_2 (b) on the cathode surface initiates the pathway.

To determine which pathway is preferable on the $TiMn_2$ surface, we first calculated the adsorption energies of Li and O at positions A, B, C, and D (as shown in Figure 3.13.a.). Equation (2.23) was used to calculate the adsorption energy of each system. Table 3.4. shows the results of adsorption energy values for Li and O atoms. The results of our study revealed that O atom adsorption occurred at three distinct sites, labeled as A, B, and C, with corresponding adsorption energies of -2.72 eV, -3.33 eV, and -4.87 eV, respectively. On the other hand, Li atom adsorption was adsorped to A, B, and D sites, with associated adsorption energies of -1.27 eV, -1.93 eV, and 2.4 eV, respectively.

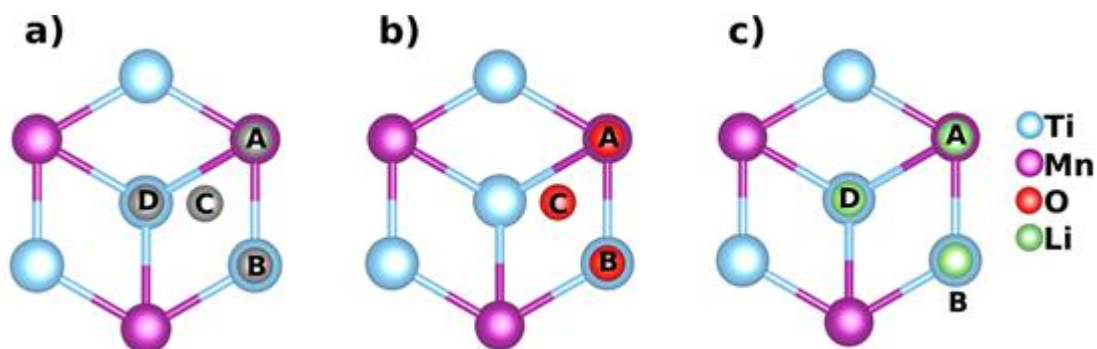


Figure 3.13. Schematic representations of the TiMn_2 (0 0 1)-D4 surface, illustrating (a) all symmetric possible adsorption sites, (b) O atoms adsorption sites, and (c) Li atoms adsorption sites.

According to this result, the formation of Li_2O_2 begins with the adsorption of O_2 molecule. After O_2 adsorption in the first step, the reaction is followed by Li^+ adsorption and LiO_2 intermediate formation on the surface. Finally, with the addition of the second Li atom, the final product (Li_2O_2) is formed as shown in figure 3.14.

The reaction steps are considered as follows:

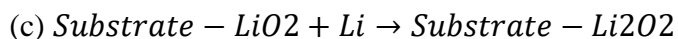
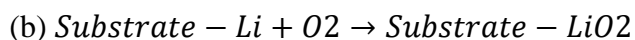
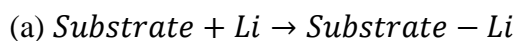


Table 3.4. The adsorption energies of the O and Li atoms on TiMn_2 (001)-D4 surface at (eV).

Adsorbate position	Eads for O (eV)	Eads for Li (eV)
Ti-top (A)	-2.72	-1.27
Mn-Tip (B)	-3.33	-1.93
Hall (C)	-4.87	----
Hall (D)	---	-2.4

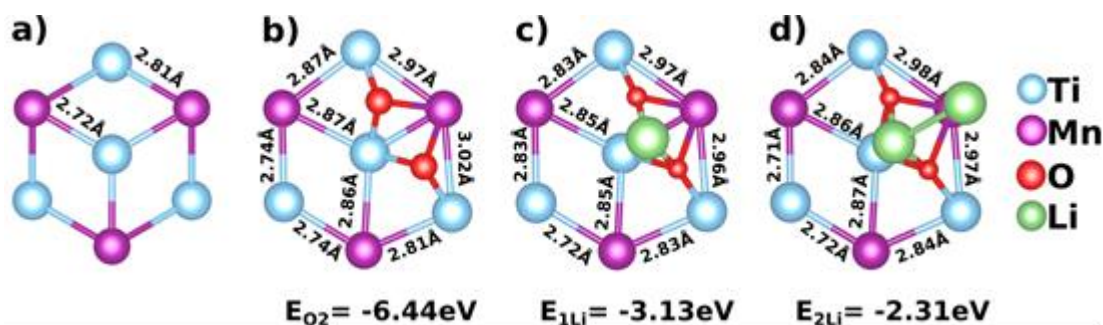


Figure 3.14. Summary of the ORR overpotentials on TiMn_2 (0 0 1)-D4 surface with the adsorption energy for intermediate reacts. (a) the TiMn_2 (0 0 1)-D4 clean surface before reaction. (b) O_2 molecule adsorption (c) first Li atom adsorption (d) second Li atom adsorption.

The ORR mechanism was examined by calculating the Gibbs free energy changes for each step of the ORR using equation (2.25). Regarding our steps of Li_2O_2 formation, the first step of the reaction involves the gas phase, O_2 , so the value of entropy change (ΔS) for O_2 is 0.63 eV at 298 K according to (Hummelshøj et al, 2010). The second and third steps are included solid phases, so the entropy changes of these steps are ignored, and the term ($T\Delta S$) becomes 0. The diagram of the Gibbs free energy changes of the ORR/OER process is shown in Figure 3.15.

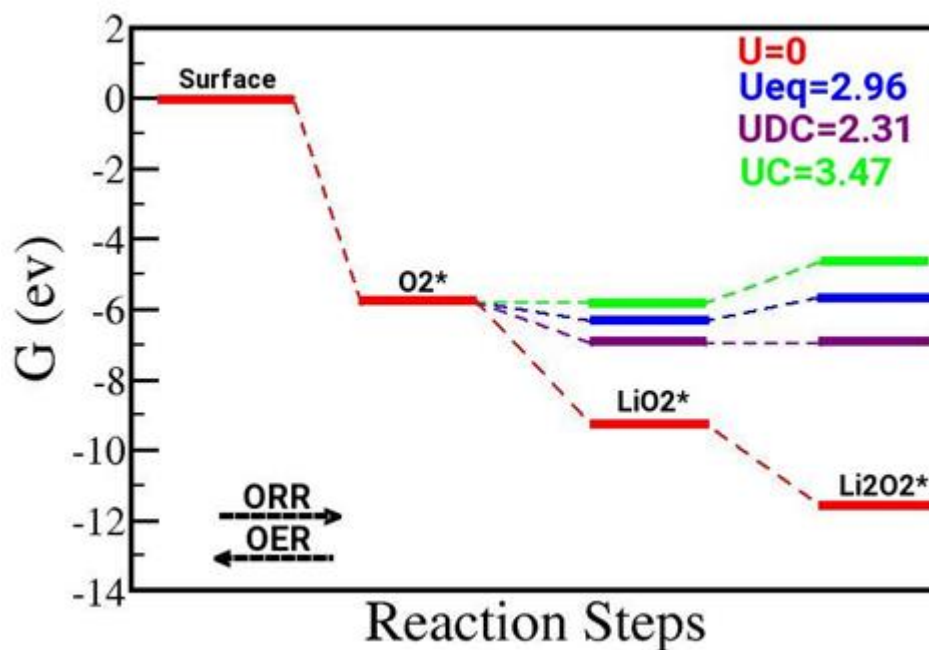


Figure 3.15. The Gibbs free energy diagrams for the ORR/OER on TiMn_2 (0 0 1)-D4 surface.

The overpotential (η) was calculated as the Gibbs free energy changes (ΔG) for the reaction according to the next equation:

$$N = \frac{\Delta G}{e} \quad (3.3)$$

In Figure 3.15., the equilibrium potential (U_{eq}) is depicted, representing the potential at which the spontaneous occurrence of oxygen reduction reaction (ORR) and oxygen evolution reaction (OER) takes place ($\Delta G \leq 0$). The maximum discharge voltage (UDC) and minimum charge voltage (UC) are denoted as UDC and UC, respectively, and they ensure that the thermodynamic free energy of each ORR/OER pathway remains in a downhill direction. Analysis of the free energy diagram reveals that the UDC of 2.31 V and UC of 3.47 V are both positioned within the practical potential range for measuring Li-O₂ battery performance (2-4.5 V).

Moreover, in evaluating catalytic activity and cycle efficiency, the overpotential of oxygen reduction reaction (ORR) and oxygen evolution reaction (OER) plays a crucial role, which is determined by both the practical potential (U_{eq}) and equilibrium potential (UDC) for ORR, and the practical potential (UC) for OER. Specifically, the ORR overpotential (η_{ORR}) is calculated as the difference between U_{eq} and UDC, while the OER overpotential (η_{OER}) is determined as the difference between UC and U_{eq} . A lower value of overpotential generally indicates higher catalytic activity and cycle efficiency.

In our investigation, the calculated ORR overpotential (η_{ORR}) for the TiMn₂ catalyst was found to be 0.65 V, and the OER overpotential (η_{OER}) was measured at 0.51 V. Comparative analysis presented in Table 3.5 indicates that TiMn₂ exhibits notably lower ORR/OER overpotential values compared to other materials. These compelling results suggest that TiMn₂ serves as an active catalyst for the ORR/OER process in nonaqueous Li-O₂ batteries. As a result, the TiMn₂ catalyst demonstrates significant catalytic activity and cycle efficiency during ORR/OER pathways, mainly attributed to its ability to minimize charge and discharge overpotential.

Table 3.5. Comparison of theoretical ORR overpotential (η_{ORR}) and OER overpotential (η_{OER}) in our study with previous works.

Materials	η_{ORR}	η_{OER}	η	Ref.
MoS ₂ /CNTs	0.29	1.05	1.34	(Hu et al, 2018)
CNT	0.97	1.77	2.74	(Hu et al, 2018)
MoO ₃	0.3	0.79	1.09	(Mu et al, 2021)
MoS ₂	0.33	1.06	1.39	(Mu et al, 2021)
NC ₃	0.95	0.37		(Zheng et al, 2019)
MoN	0.19	0.72		(Mu et al, 2021a)
Co ₉ S ₈	0.31	1.06		(G. Wang et al, 2020)
Pt	1.02	1.62		(B. G. Kim et al, 2014)
MnO ₂	0.27	0.33		(Y. Zheng et al, 2015)
Pt	1.02	1.62		(H.-J. Kim et al, 2015)
Pt ₃ Co	1.02	1.13		(H.-J. Kim et al, 2015)
PtCo	0.19	0.2		(H.-J. Kim et al, 2015)
Co	1.77	4.99		(H.-J. Kim et al, 2015)
PtIr	0.11 (0.60)	0.33 (1.16)	0.44 (1.76)	(Zhou et al, 2021)
Pt	0.17(: 1.30)	1.02 (1.52)	1.19 (2.82)	(Zhou et al, 2021)
La _{0.8} Sr _{0.2} VO ₃		1.84	(Sung et al, 2021)
La _{0.8} Sr _{0.2} VO ₄			1.92	
LaMnO ₃ -	1.61	(Y. Zhao et al,
La _{0.8} Sr _{0.2} MnO ₃ -			1.54	2017b)
La _{0.4} Sr _{0.6} MnO ₃			1.47	
TiMn ₂	0.65	0.51	1.16	This Work

3.3. MnO₂ as a Carbon Free Cathode for Li-O₂ Battery

Manganese oxide stands out among various transition metal oxides, capturing considerable interest due to its rich array of chemical compositions and structures found within the Mn:O phase diagram. Notably, alpha-manganese dioxide (α -MnO₂) has garnered significant attention as a cost-effective and environmentally friendly bifunctional electrocatalyst, proficient in facilitating both the oxygen reduction reaction (ORR) and oxygen evolution reaction (OER) (Pandit, 2021; Su et, 2013).

3.3.1. Using DFT+U to predict the bulk properties and band gap

The selection of the exchange-correlation (XC) functional within the density functional theory (DFT) framework significantly impacts the characterization of electron exchange-correlation interactions and, consequently, the redox energetics. It should be noted that an accurate description of redox energetics in transition metal oxides (TMOs) holds substantial importance in fields such as photovoltaics, batteries, and photoelectrocatalysts.

The GGA+U method exhibited limitations in accurately predicting lattice parameters and band gap values for MnO₂. In contrast, Kitchaev et al. (2016) reported that the SCAN functional uniquely provides precise formation energies and properties for all MnO₂ polymorphs, including α -MnO₂. Recent studies demonstrated that the Strongly constrained and appropriately normed (SCAN) exchange-correlation functional, when augmented with a Hubbard U correction determined from experimental oxidation enthalpies, successfully reproduces the ground-state structure, lattice parameters, magnetic moments, and electronic properties of MnO₂ (Long et al, 2020a).

The determination of the Hubbard U parameter for each transition metal (TM) atom is not straightforward and typically relies on the choice of the XC functional, which introduces inherent errors. An alternative approach involves fitting the magnitude of U to either experimentally measured band gaps or lattice parameters (Long et al, 2020b).

In this work, we explore the performance of GGA+U, SCAN, and SCAN+U methods to improve both the geometric properties and band gaps in our model. Furthermore, we validate the optimized values of U by conducting several

transferability checks for each 3d material. Consequently, a SCAN+U framework, incorporating an appropriately determined U, becomes essential for accurately assessing ground-state energies and obtaining qualitatively consistent electronic structures for TMOs.

To investigate the impact of different XC functionals on the lattice parameters and band structure of MnO₂, we consider the well-known variability of MnO₂ band gaps depending on the synthesis method and final product shape (Young et al, 2015). For instance, the band gap values for MnO₂ have been reported as 2.55 eV Ramesh et al. (2016) and ranging from 1.25 to 1.67 eV (Mondal et al, 2018). The lattice parameters exhibit minimal discrepancies, with values of a=b=9.84 Å and c=2.84 Å Mondal et al. (2018), and a=b=9.82 Å and c=8.88 Å (Sunaina et al, 2021). Consequently, we adopt the lattice parameters as a reference for determining the appropriate U value. Figure 3.16. a and b display the crystal structure and band structure using (SCAN+4) method.

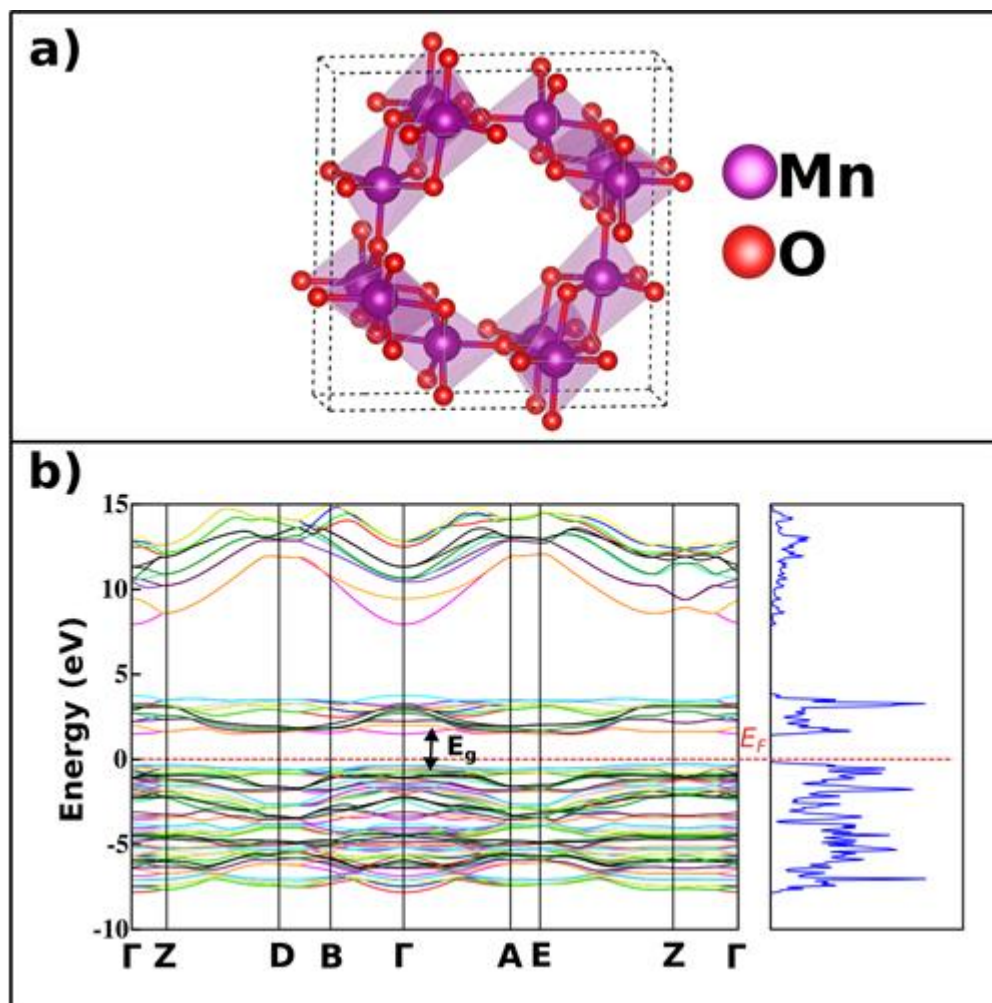


Figure 3.16. a) The crystal structure of MnO₂, b) Band structure and partial density of states (PDOS) analysis.

Table 3.6. The band gap value (in eV) and the lattice constants (a, b and c) for α -MnO₂ bulk structure with three different DFT-based methods GGA+U, SCAN, and SCAN+U.

U Function value	GGA+U		SCAN		SCAN+U	
	Band gap	a-b-c	Band gap	a-b-c	Band gap	a-b-c
2.5	0.67	9.72-9.73-2.83	1.5	9.70-9.70-2.84	1.55	9.73-9.73-2.86
3	0.75	9.88-9.88-2.91			1.49	9.74-9.74-2.87
3.5	0.23	9.62-9.80-2.85			1.35	9.75-9.75-2.87
4	0.33	9.79-9.79-2.84			1.22	9.76-9.76-2.88
4.5	---				0.55	9.58-9.58-2.94

Table 3.6. presents the experimental values alongside the corresponding calculations obtained using the GGA+U, SCAN, and SCAN+U methods for both band gap and lattice parameters. The range of U values considered for the GGA+U and SCAN+U

calculations spans from 2.5 eV to 4.5 eV. Analysis of the band gap results, as presented in Table 3.6., reveals that the GGA+U method, with a U value of 4 eV, achieved complete correspondence with the experimental band gap value. However, it should be noted that the GGA+U method performed successfully in predicting the lattice parameters. On the other hand, the SCAN method exhibited a high degree of accuracy in predicting both the band gap and lattice parameters. Notably, the SCAN+U method, with a U value of 4 eV, demonstrated the most favorable performance in terms of both band gap prediction and lattice parameter estimation.

3.3.2. Surface stability

The determination of the most thermodynamically stable termination for MnO₂-(211) was conducted as detailed in section 3.2.2. In this particular investigation, the construction of supercell models was accomplished through periodic repetition of the hexagonal unit cell in the (211) plane. The (211) model encompasses four distinct atomic terminations, denoted as (Mn, O1, O2, and O3), as visually depicted in Figure 3.17.

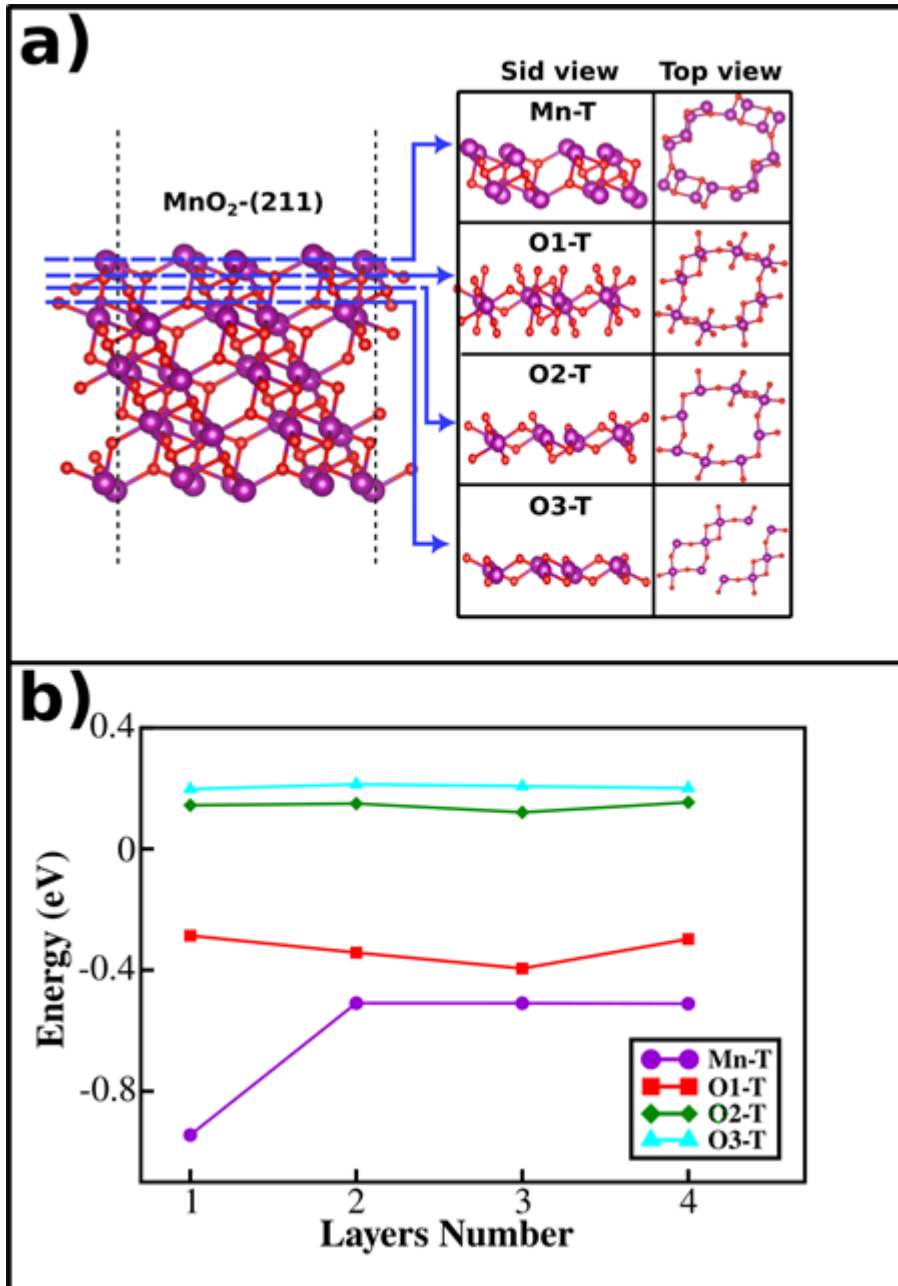


Figure 3.17. The (211) surface plane of MnO₂ with two different four terminations, b) Surface energy comparison of all terminations as a function of the number of layers in the MnO₂ crystal.

Given the asymmetrical nature of the (211) plane, the surface energy was computed as a variable dependent on the atomic layer, as expounded in section 2.2.7. To obtain the bulk energy, E_{bulk} , for each thickness N of slab layers, we selected the differential increment in total energy upon the addition of one layer of material.

The computed adsorption energy is graphically presented in Figure 3.17.b., where it is observed that the (Mn) termination exhibits a stabilized and convergent energy value in comparison to the other terminations.

3.3.3. The effect of DFT+U on the ORR/OER mechanism

In accordance with Section 3.3.1. of this study, our initial focus lies in investigating the surface reactivity of MnO₂-(112) towards the absorption of O and Li atoms. To determine the preferable pathway on the MnO₂ surface, we conducted calculations to evaluate the adsorption energies of Li and O at eight different symmetric positions (as shown in Figure 3.18.). These adsorption energies were computed using equation (2.23). The resulting adsorption energy values for Li and O atoms are presented in Table 3.7. Notably, all adsorption calculations were carried out using the SCAN+U method.

Table 3.7. The adsorption energies of the O and Li atoms on MnO₂ (211)-Mn surface termination at (eV).

Atome Position	Eads-Li (eV)	Eads-O (eV)
1	-0.33	-5.18
2	-1.29	-6.33
3	-0.03	-5.03
4	-1.4	-5.32
5	-1.28	-5.09
6	-0.89	-5.49
7	-1.02	-5.32
8	-1.35	-6.17
9	-2.01	-4.78

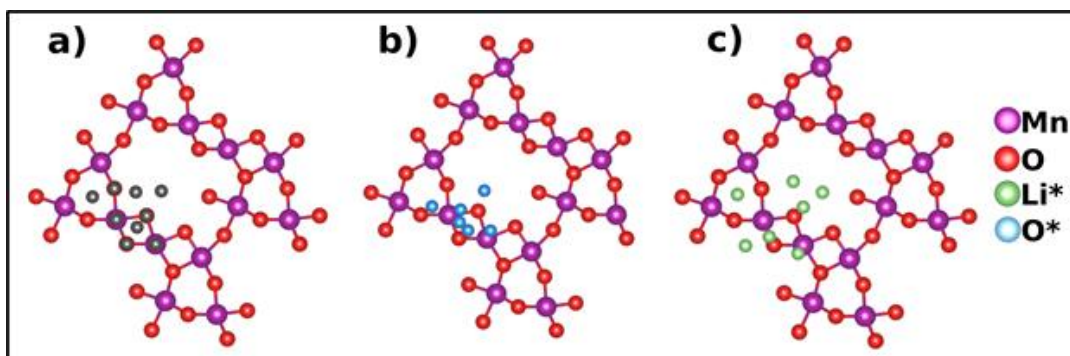


Figure 3.18. Schematic representations of the MnO_2 (211)-Mn surface, illustrating (a) all symmetric possible adsorption sites, (b) O atoms adsorption sites, and (c) Li atoms adsorption sites.

Based on the findings in Table 3.7., the formation of Li_2O_2 initiates with the adsorption of the Li atom. Subsequently, the reaction progresses with O_2 adsorption to form the LiO_2 intermediate on the surface. Finally, upon the addition of the second Li atom, the formation of the final product (Li_2O_2) is accomplished (as depicted in Figure 3.19. for GGA+U method and figure 3.20. for SCAN+U method).

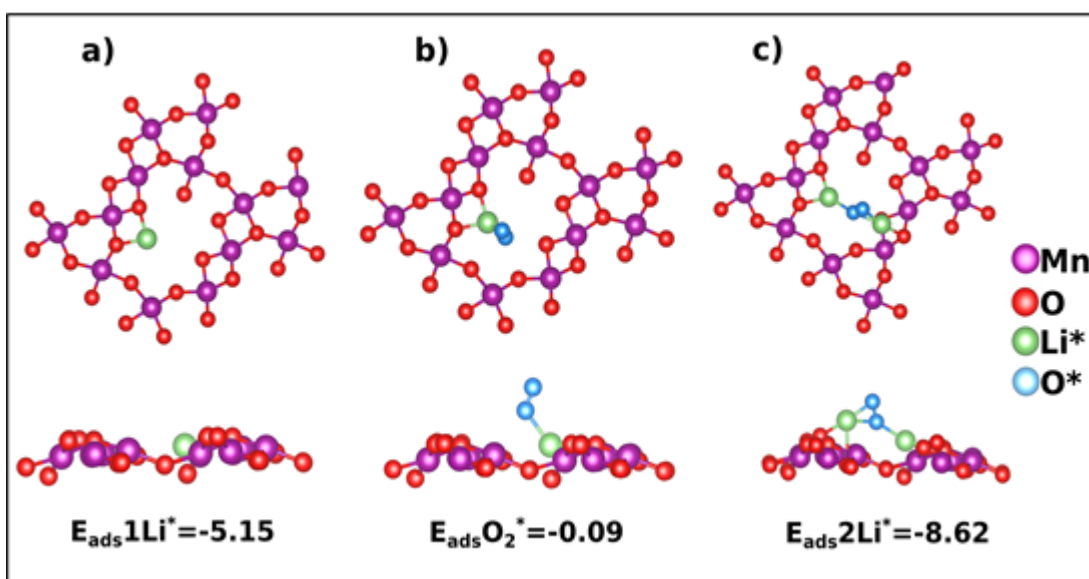


Figure 3.19. Summary of the ORR overpotentials on MnO_2 (211)-Mn surface with the adsorption energy for intermediate reacts using GGA+U method (a) the MnO_2 (211)-Mn clean surface before reaction. b) First Li atom adsorption c) O_2 molecule adsorption d) second Li atom adsorption.

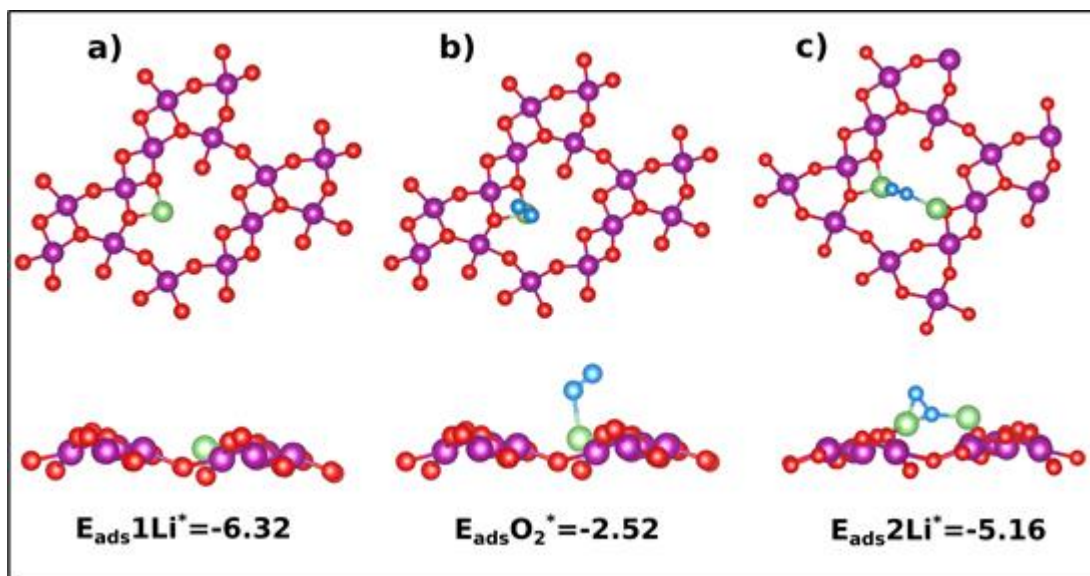


Figure 3.20. Summary of the ORR overpotentials on MnO₂ (211)-Mn surface with the adsorption energy for intermediate reacts using SCAN+U method (a) the MnO₂ (211)-Mn clean surface before reaction. b) First Li atom adsorption c) O₂ molecule adsorption d) second Li atom adsorption.

To study the ORR mechanism, we computed the Gibbs free energy changes for each step of the ORR using equation (2.25).

Regarding the steps involved in the formation of Li₂O₂, the first step entails Li-ion adsorption, for which the entropy change (ΔS) is considered as 0 eV at 298 K for the solid phase. The second step involves the gas phase, O₂, and the entropy change (ΔS) for O₂ is 0.63 eV at 298 K, following the work by (Hummelshøj et al, 2010). The third steps (Li interaction) pertain to solid phases, and thus, the entropy changes for these steps are disregarded, resulting in a value of 0 for the term ($T\Delta S$).

We employed two different DFT methods to calculate the Gibbs free energy for ORR/OER over-reaction.

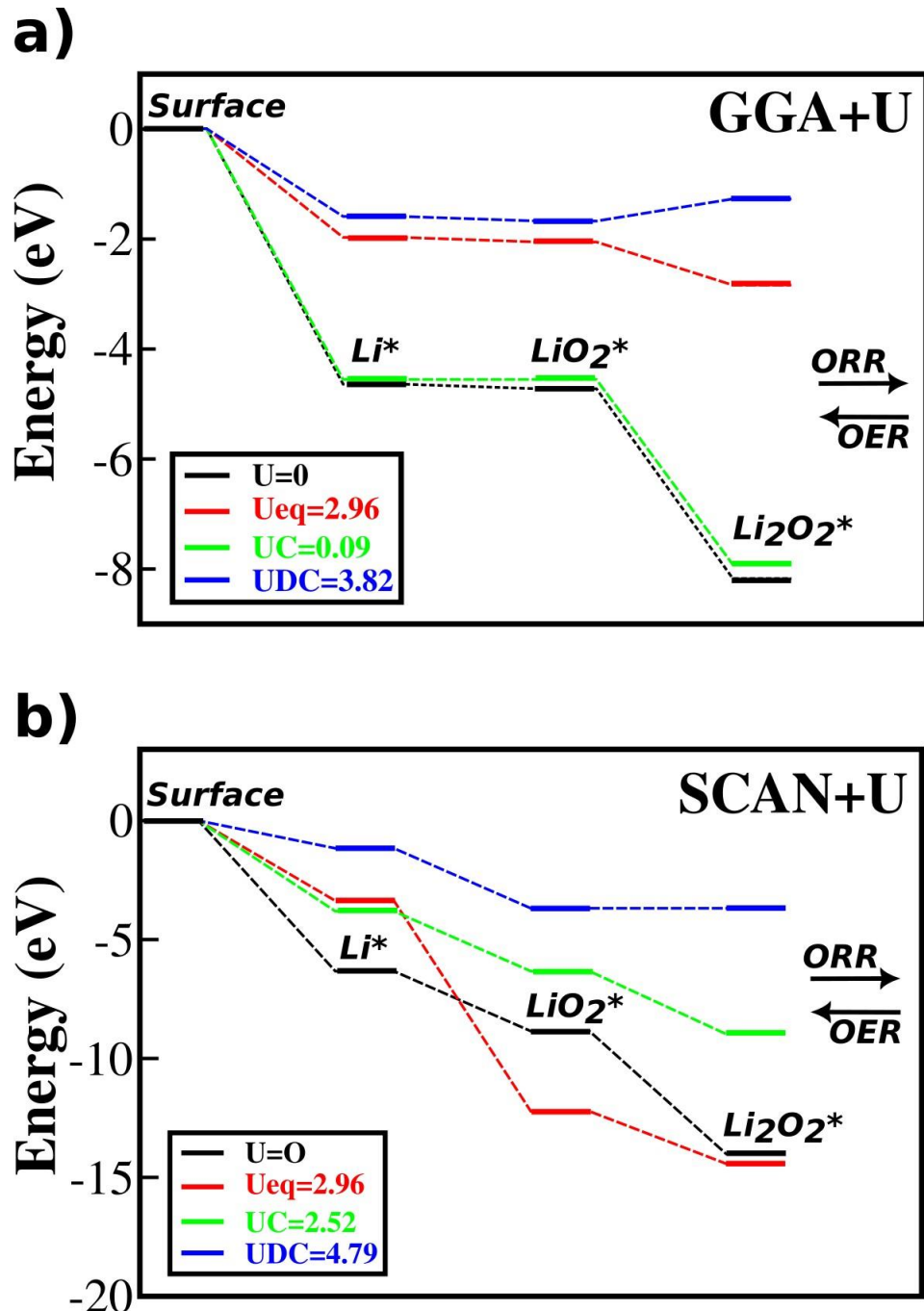


Figure 3.21. The Gibbs free energy diagrams for the ORR/OER on MnO_2 (211)-Mn surface termination using a)GGA+U method, b) SCAN+U method.

The overpotential (η) was determined as the Gibbs free energy changes (ΔG) for the reaction according to equation (3.1), with $N=\Delta G/e$. In Figure 3.21, we depict the equilibrium potential (U_{eq}), which represents the potential at which the spontaneous occurrence of oxygen reduction reaction (ORR) and oxygen evolution reaction (OER) takes place ($\Delta G \leq 0$). The maximum discharge voltage (UDC) and minimum charge voltage (UC) are denoted as UDC and UC, respectively, ensuring that the thermodynamic free energy of each ORR/OER pathway remains in a downhill

direction. Our analysis yielded distinct results. The GGA+U method indicated a maximum discharge voltage (UDC) of 0.09 V and a minimum charge voltage (UC) of 3.82 V. On the other hand, the SCAN+U method resulted in a (UDC) of 2.52 V and a (UC) of 4.79 V. These findings underscore the significance of the computational approach in predicting the discharge and charge voltages and highlight the influence of the chosen method on the calculated thermodynamic free energy values.

Furthermore, the overpotential of ORR/OER, determined by the practical potential and equilibrium potential, is employed to assess the catalytic activity and cycle efficiency. The calculated ORR overpotential (η_{ORR}) is defined as the difference between U_{eq} and UDC, while the OER overpotential (η_{OER}) is defined as the difference between UC and U_{eq} . Generally, a lower overpotential value signifies higher catalytic activity and cycle efficiency.

According to our calculations, the oxygen reduction reaction (ORR) overpotential was found to be 0.86 V, and the oxygen evolution reaction (OER) overpotential was 2.87 V when employing the GGA+U method. Conversely, utilizing the SCAN+U method, the ORR overpotential remained at 0.43 V, while the OER overpotential decreased to 1.83 V.

As a result, our study demonstrates that the choice of computational methods, specifically GGA+U and SCAN+U, significantly influences several key aspects of the system under investigation. Particularly, the magnitude of adsorption values for the reaction intermediates, the mechanisms of discharge and charge processes, the voltage values, and the free energy diagram.

Overall, the study underscores the importance of carefully selecting the appropriate computational method based on the specific objectives and properties of interest, as it can lead to contrasting predictions and interpretations of key electrochemical processes and properties.

4. CONCLUSION

4.1. Sulfur Doped LATP

The LATP-based study investigates the impact of sulfur doping on the stability, lithium-ion migration, and electronic properties of Lithium Aluminum Titanium Phosphate (LATP). We employ DFT-based first-principles calculations to gain deeper insights into the performance enhancement of Sulfur-doped LATP (S@LATP). Four distinct unit cell models (S1, S2, S3, and S4) are constructed to emulate the sulfur doped LATP, with the S3 configuration being identified as the most energetically stable. Subsequently, we explored the Li-ion migration mechanisms along LATP and S@LATP diffusion paths using the NEB method. Activation energy profiles for Li migration are examined for three Wyckoff positions (6b-18e-6b). Our findings reveal that in S1, S2, and S3 configurations, the lithium-ion diffusion activation energy barrier locally diminishes, attributed to enlarged LiO_6 polyhedral volumes within the diffusion path. Additionally, we analyze the electronic structure of both bare LATP and S@LATP. Our developed strategy to enhance the ionic conductivity of oxide-based solid electrolytes can potentially be extended to other oxide systems such as LLZO, LLTO, and LAGP.

4.2. TiMn_2

In conclusion, the TiMn_2 compound, belonging to the C14 type Laves phase, exhibits metallic properties and a hexagonal crystal structure with space group $P6_3/mmc$. Its ability to absorb and release large quantities of hydrogen gas makes it a promising candidate for use as negative electrodes in rechargeable batteries, owing to its reversible absorption and desorption capabilities, along with its substantial storage capacity.

The study delves into the surface stability of TiMn_2 , analyzing different atomic terminations on (0 0 1) and (1 1 2) planes. Surface energy calculations reveal that the termination with Dx within (0 0 1) is the most stable. Moreover, investigations into the ORR/OER mechanism indicate that the formation of Li_2O_2 begins through the

adsorption of Li, followed by O₂ adsorption. The reaction proceeds with Li⁺ adsorption and the formation of a LiO₂ intermediate on the surface, eventually culminating in the creation of the final product, Li₂O₂.

The Gibbs free energy diagram further elucidates the ORR/OER process, and the calculated overpotential values for ORR and OER demonstrate TiMn₂'s catalytic activity and cycle efficiency in nonaqueous Li-O₂ batteries. Notably, TiMn₂ exhibits relatively low ORR/OER overpotential, making it a promising catalyst for these reactions. Consequently, TiMn₂ holds significant potential for enhancing the performance of Li-O₂ batteries, paving the way for further exploration of its applications in energy storage technologies.

4.3. MnO₂

This study focuses on investigating the surface reactivity of MnO₂-(112) towards the adsorption of O and Li atoms. The preferable pathway on the MnO₂ surface is determined by calculating the adsorption energies of Li and O at different symmetric positions. The Li₂O₂ formation begins with the absorption of Li in all considered systems. Further analysis involves studying the discharge process path, which indicates that Li₂O₂ formation initiates with O₂ molecule adsorption, followed by Li⁺ adsorption and LiO₂ intermediate formation. The final product, Li₂O₂, is formed upon adding the second Li atom. The Gibbs free energy changes for each step of the ORR mechanism are computed to study the ORR process.

The study employs two different DFT methods to calculate the Gibbs free energy for ORR/OER over-reaction. The comparison between the methods shows significant differences in the obtained Gibbs free energy values. The overpotential (η) is calculated as the Gibbs free energy changes (ΔG) for the reaction. The free energy diagram of the ORR/OER process is analyzed, and it reveals that the UDC and UC fall within the practical potential range for measuring Li-O₂ battery performance (2-4.5 V). The influence of the first electronic ground state on predicting the free energy diagram and total overpotential value is highlighted.

Overall, the study provides insights into the adsorption behavior of Li and O atoms on the MnO₂ surface and sheds light on the ORR mechanism, which is crucial for advancing the understanding of Li-O₂ battery performance.

REFERENCES

- Ahmed, D. A. A., Bağcı, S., Karaca, E., & Tütüncü, H. M. (2018). *Elastic properties of ABF₃ (A:Ag,K and B:Mg, Zn) perovskites*. 020035. <https://doi.org/10.1063/1.5078907>
- Anisimov, V. I., Zaanen, J., & Andersen, O. K. (1991). Band theory and Mott insulators: Hubbard U instead of Stoner I . *Physical Review B*, *44*(3), 943–954. <https://doi.org/10.1103/PhysRevB.44.943>
- Arbi, K., Mandal, S., Rojo, J. M., & Sanz, J. (2002). Dependence of ionic conductivity on composition of fast ionic conductors $\text{Li}_{1+x}\text{Ti}_{2-x}\text{Al}_x(\text{PO}_4)_3$, $0 \leq x \leq 0.7$. A parallel NMR and electric impedance study. *Chemistry of Materials*, *14*(3), 1091–1097. <https://doi.org/10.1021/cm010528i>
- Åvall, G., Mindemark, J., Brandell, D., & Johansson, P. (2018). Sodium-Ion Battery Electrolytes: Modeling and Simulations. *Advanced Energy Materials*, *8*(17), 1703036. <https://doi.org/10.1002/aenm.201703036>
- Bader, R. F. W. (1991). A quantum theory of molecular structure and its applications. *Chemical Reviews*, *91*(5), 893–928. <https://doi.org/10.1021/cr00005a013>
- Balaish, M., Jung, J., Kim, I., & Ein-Eli, Y. (2020). A Critical Review on Functionalization of Air-Cathodes for Nonaqueous Li–O₂ Batteries. *Advanced Functional Materials*, *30*(18), 1808303. <https://doi.org/10.1002/adfm.201808303>
- Bhalla, A. S., Guo, R., & Roy, R. (2000). The perovskite structure—a review of its role in ceramic science and technology. *Materials Research Innovations*, *4*(1), 3–26. <https://doi.org/10.1007/s100190000062>
- Tanner B. K. (1995). *Introduction to the Physics of Electrons in Solids*. Cambridge University Press.
- Boettger, J. C. (1994). Nonconvergence of surface energies obtained from thin-film calculations. *Physical Review B*, *49*(23), 16798–16800. <https://doi.org/10.1103/PhysRevB.49.16798>
- Chen, X., He, W., Ding, L.-X., Wang, S., & Wang, H. (2019). Enhancing interfacial contact in all solid state batteries with a cathode-supported solid electrolyte membrane framework. *Energy & Environmental Science*, *12*(3), 938–944. <https://doi.org/10.1039/C8EE02617C>
- Cococcioni, M., & de Gironcoli, S. (2005). Linear response approach to the calculation of the effective interaction parameters in the LDA + U method. *Physical Review B*, *71*(3), 035105. <https://doi.org/10.1103/PhysRevB.71.035105>

- Colmenero, F., Fernández, A. M., Cobos, J., & Timón, V. (2019). Periodic DFT Study of the Thermodynamic Properties and Stability of Schoepite and Metaschoepite Mineral Phases. *ACS Earth and Space Chemistry*, 3(1), 17–28. <https://doi.org/10.1021/acsearthspacechem.8b00109>
- DeWees, R., & Wang, H. (2019). Synthesis and Properties of NaSICON-type LATP and LAGP Solid Electrolytes. *ChemSusChem*, 12(16), 3713–3725. <https://doi.org/10.1002/cssc.201900725>
- Dubarry, M., Devie, A., Stein, K., Tun, M., Matsuura, M., & Rocheleau, R. (2017). Battery Energy Storage System battery durability and reliability under electric utility grid operations: Analysis of 3 years of real usage. *Journal of Power Sources*, 338, 65–73. <https://doi.org/10.1016/j.jpowsour.2016.11.034>
- Dudarev, S. L., Botton, G. A., Savrasov, S. Y., Humphreys, C. J., & Sutton, A. P. (1998). Electron-energy-loss spectra and the structural stability of nickel oxide: An LSDA+U study. *Physical Review B*, 57(3), 1505–1509. <https://doi.org/10.1103/PhysRevB.57.1505>
- Elbaz, Y., Furman, D., & Caspary Toroker, M. (2020). Modeling Diffusion in Functional Materials: From Density Functional Theory to Artificial Intelligence. *Advanced Functional Materials*, 30(18), 1900778. <https://doi.org/10.1002/adfm.201900778>
- Ells, A. W., Evans, M. L., Groh, M. F., Morris, A. J., & Marbella, L. E. (2022). Phase Transformations and Phase Segregation during Potassiation of Sn x P y Anodes. *Chemistry of Materials*, 34(16), 7460–7467. <https://doi.org/10.1021/acs.chemmater.2c01570>
- Engel, E., & Dreizler, R. M. (2011). *Density Functional Theory*. Springer Berlin Heidelberg. <https://doi.org/10.1007/978-3-642-14090-7>
- Fromsejer, R., Maribo-Mogensen, B., Kontogeorgis, G. M., & Liang, X. (2023). Evaluating the harmonic approximation for the prediction of thermodynamic formation properties of solids. *Computational Materials Science*, 223, 112152. <https://doi.org/10.1016/j.commatsci.2023.112152>
- Gao, R., Liang, X., Yin, P., Wang, J., Lee, Y. L., Hu, Z., & Liu, X. (2017). An amorphous LiO₂-based Li-O₂ battery with low overpotential and high rate capability. *Nano Energy*, 41, 535–542. <https://doi.org/10.1016/j.nanoen.2017.10.013>
- Goodenough, J. B., & Park, K.-S. (2013). The Li-Ion Rechargeable Battery: A Perspective. *Journal of the American Chemical Society*, 135(4), 1167–1176. <https://doi.org/10.1021/ja3091438>
- Groß, A. (2009). *Theoretical Surface Science*. Springer Berlin Heidelberg. <https://doi.org/10.1007/978-3-540-68969-0>
- Harper, A. F., Evans, M. L., & Morris, A. J. (2020). Computational Investigation of Copper Phosphides as Conversion Anodes for Lithium-Ion Batteries. *Chemistry of Materials*, 32(15), 6629–6639. <https://doi.org/10.1021/acs.chemmater.0c02054>
- He, Q., Yu, B., Li, Z., & Zhao, Y. (2019). Density Functional Theory for Battery Materials. *ENERGY & ENVIRONMENTAL MATERIALS*, 2(4), 264–279. <https://doi.org/10.1002/eem2.12056>

- He, Y., Su, Y., Qin, Y., Ding, L., Li, X., Mei, S., Zhang, Y., Ma, Y., Wei, L., Gu, Y., Peng, Y., & Deng, Z. (2023). Stepping Up the Kinetics of Li–O₂ Batteries by Shrinking Down the Li₂O₂ Granules through Concertedly Enhanced Catalytic Activity and Photoactivity of Se-Doped LaCoO₃. *ACS Applied Materials & Interfaces*, *15*(7), 9285–9295. <https://doi.org/10.1021/acsami.2c19975>
- Henkelman, G., Uberuaga, B. P., & Jónsson, H. (2000). A climbing image nudged elastic band method for finding saddle points and minimum energy paths. *The Journal of Chemical Physics*, *113*(22), 9901–9904. <https://doi.org/10.1063/1.1329672>
- Himmetoglu, B., Floris, A., de Gironcoli, S., & Cococcioni, M. (2014). Hubbard-corrected DFT energy functionals: The LDA+U description of correlated systems. *International Journal of Quantum Chemistry*, *114*(1), 14–49. <https://doi.org/10.1002/qua.24521>
- Hohenberg, P., & Kohn, W. (1964). Inhomogeneous Electron Gas. *Physical Review*, *136*(3B), B864–B871. <https://doi.org/10.1103/PhysRev.136.B864>
- Hu, A., Long, J., Shu, C., Liang, R., & Li, J. (2018). Three-Dimensional Interconnected Network Architecture with Homogeneously Dispersed Carbon Nanotubes and Layered MoS₂ as a Highly Efficient Cathode Catalyst for Lithium–Oxygen Battery. *ACS Applied Materials & Interfaces*, *10*(40), 34077–34086. <https://doi.org/10.1021/acsami.8b06912>
- Huang, H., Xu, R., Feng, Y., Zeng, S., Jiang, Y., Wang, H., Luo, W., & Yu, Y. (2020). Sodium/Potassium-Ion Batteries: Boosting the Rate Capability and Cycle Life by Combining Morphology, Defect and Structure Engineering. *Advanced Materials*, *32*(8), 1904320. <https://doi.org/10.1002/adma.201904320>
- Hummelshøj, J. S., Blomqvist, J., Datta, S., Vegge, T., Rossmeisl, J., Thygesen, K. S., Luntz, A. C., Jacobsen, K. W., & Nørskov, J. K. (2010). Communications: Elementary oxygen electrode reactions in the aprotic Li-air battery. *The Journal of Chemical Physics*, *132*(7), 071101. <https://doi.org/10.1063/1.3298994>
- Kittel, C. (2005). *Introduction to Solid State Physics Charles Kittel*. John Wiley & Sons, Inc.
- Janek, J., & Zeier, W. G. (2016). A solid future for battery development. *Nature Energy*, *1*(9), 16141. <https://doi.org/10.1038/nenergy.2016.141>
- Ji, L., Lin, Z., Alcoutlabi, M., & Zhang, X. (2011). Recent developments in nanostructured anode materials for rechargeable lithium-ion batteries. *Energy & Environmental Science*, *4*(8), 2682. <https://doi.org/10.1039/c0ee00699h>
- Jia, H., Wang, Z., Tawiah, B., Wang, Y., Chan, C.-Y., Fei, B., & Pan, F. (2020). Recent advances in zinc anodes for high-performance aqueous Zn-ion batteries. *Nano Energy*, *70*, 104523. <https://doi.org/10.1016/j.nanoen.2020.104523>

- JÓNSSON, H., MILLS, G., & JACOBSEN, K. W. (1998). Nudged elastic band method for finding minimum energy paths of transitions. *Classical and Quantum Dynamics in Condensed Phase Simulations*, 385–404. https://doi.org/10.1142/9789812839664_0016
- Jungwirth, P. (2010). Density Functional Theory. A Practical Introduction. By David Sholl and Janice A. Steckel. *Angewandte Chemie International Edition*, 49(3), 485–485. <https://doi.org/10.1002/anie.200905551>
- Karuppasamy, K., Prasanna, K., Jothi, V. R., Vikraman, D., Hussain, S., Hwang, J.-H., & Kim, H.-S. (2020). Recent Advances in Nanostructured Transition Metal Carbide- and Nitride-Based Cathode Electrocatalysts for Li–O₂ Batteries (LOBs): A Brief Review. *Nanomaterials*, 10(11), 2106. <https://doi.org/10.3390/nano10112106>
- Kim, B. G., Kim, H.-J., Back, S., Nam, K. W., Jung, Y., Han, Y.-K., & Choi, J. W. (2014). Improved reversibility in lithium-oxygen battery: Understanding elementary reactions and surface charge engineering of metal alloy catalyst. *Scientific Reports*, 4(1), 4225. <https://doi.org/10.1038/srep04225>
- Kim, D. Y., Kim, M., Kim, D. W., Suk, J., Park, O. O., & Kang, Y. (2015). Flexible binder-free graphene paper cathodes for high-performance Li-O₂ batteries. *Carbon*, 93, 625–635. <https://doi.org/10.1016/j.carbon.2015.05.097>
- Kim, H.-J., Jung, S. C., Han, Y.-K., & Oh, S. H. (2015). An atomic-level strategy for the design of a low overpotential catalyst for Li–O₂ batteries. *Nano Energy*, 13, 679–686. <https://doi.org/10.1016/j.nanoen.2015.03.030>
- Kitchaev, D. A., Peng, H., Liu, Y., Sun, J., Perdew, J. P., & Ceder, G. (2016). Energetics of MnO₂ polymorphs in density functional theory. *Physical Review B*, 93(4), 045132. <https://doi.org/10.1103/PhysRevB.93.045132>
- Kızılaslan, A., Kırkbınar, M., Cetinkaya, T., & Akbulut, H. (2020). Sulfur doped Li_{1.3}Al_{0.3}Ti₁(PO₄)₃ solid electrolytes with enhanced ionic conductivity and a reduced activation energy barrier. *Physical Chemistry Chemical Physics*, 22(30), 17221–17228. <https://doi.org/10.1039/D0CP03442H>
- Koch, W., & Holthausen, M. C. (2001). *A Chemist's Guide to Density Functional Theory*. Wiley. <https://doi.org/10.1002/3527600043>
- Kohn, W., & Sham, L. J. (1965). Self-Consistent Equations Including Exchange and Correlation Effects. *Physical Review*, 140(4A), A1133–A1138. <https://doi.org/10.1103/PhysRev.140.A1133>
- Kresse, G., & Furthmüller, J. (1996a). Efficiency of ab-initio total energy calculations for metals and semiconductors using a plane-wave basis set. *Computational Materials Science*, 6(1), 15–50. [https://doi.org/10.1016/0927-0256\(96\)00008-0](https://doi.org/10.1016/0927-0256(96)00008-0)
- Kresse, G., & Furthmüller, J. (1996b). Efficient iterative schemes for *ab initio* total-energy calculations using a plane-wave basis set. *Physical Review B*, 54(16), 11169–11186. <https://doi.org/10.1103/PhysRevB.54.11169>
- Kresse, G., & Hafner, J. (1993). *Ab initio* molecular dynamics for liquid metals. *Physical Review B*, 47(1), 558–561. <https://doi.org/10.1103/PhysRevB.47.558>

- Ladha, D. G. (2019). A review on density functional theory–based study on two-dimensional materials used in batteries. *Materials Today Chemistry*, *11*, 94–111. <https://doi.org/10.1016/j.mtchem.2018.10.006>
- Lee, J. G. (2016). *Computational Materials Science*. CRC Press. <https://doi.org/10.1201/9781315368429>
- Liao, K., Zhang, T., Wang, Y., Li, F., Jian, Z., Yu, H., & Zhou, H. (2015). Nanoporous Ru as a Carbon- and Binder-Free Cathode for Li-O₂ Batteries. *ChemSusChem*, *8*(8), 1429–1434. <https://doi.org/10.1002/cssc.201403371>
- Liechtenstein, A. I., Anisimov, V. I., & Zaanen, J. (1995). Density-functional theory and strong interactions: Orbital ordering in Mott-Hubbard insulators. *Physical Review B*, *52*(8), R5467–R5470. <https://doi.org/10.1103/PhysRevB.52.R5467>
- Liu, T., Vivek, J. P., Zhao, E. W., Lei, J., Garcia-Araez, N., & Grey, C. P. (2020). Current Challenges and Routes Forward for Nonaqueous Lithium–Air Batteries. *Chemical Reviews*, *120*(14), 6558–6625. <https://doi.org/10.1021/acs.chemrev.9b00545>
- Liu, Y., Sun, Q., Zhao, Y., Wang, B., Kaghazchi, P., Adair, K. R., Li, R., Zhang, C., Liu, J., Kuo, L.-Y., Hu, Y., Sham, T.-K., Zhang, L., Yang, R., Lu, S., Song, X., & Sun, X. (2018). Stabilizing the Interface of NASICON Solid Electrolyte against Li Metal with Atomic Layer Deposition. *ACS Applied Materials & Interfaces*, *10*(37), 31240–31248. <https://doi.org/10.1021/acsami.8b06366>
- Long, O. Y., Sai Gautam, G., & Carter, E. A. (2020a). Evaluating optimal U for 3 d transition-metal oxides within the SCAN+ U framework. *Physical Review Materials*, *4*(4), 045401. <https://doi.org/10.1103/PhysRevMaterials.4.045401>
- Long, O. Y., Sai Gautam, G., & Carter, E. A. (2020b). Evaluating optimal U for 3 d transition-metal oxides within the SCAN+ U framework. *Physical Review Materials*, *4*(4), 045401. <https://doi.org/10.1103/PhysRevMaterials.4.045401>
- Lu, S., Huynh, H. L., Lou, F., Guo, K., & Yu, Z. (2021). Single transition metal atom embedded antimonene monolayers as efficient trifunctional electrocatalysts for the HER, OER and ORR: a density functional theory study. *Nanoscale*, *13*(30), 12885–12895. <https://doi.org/10.1039/D1NR02235K>
- Luo, Y., Lu, F., Jin, C., Wang, Y., Yang, R., & Yang, C. (2016). NiCo₂O₄@La_{0.8}Sr_{0.2}MnO₃ core–shell structured nanorods as efficient electrocatalyst for Li O₂ battery with enhanced performances. *Journal of Power Sources*, *319*, 19–26. <https://doi.org/10.1016/j.jpowsour.2016.04.047>
- Ma, L., Yu, T., Tzoganakis, E., Amine, K., Wu, T., Chen, Z., & Lu, J. (2018). Fundamental Understanding and Material Challenges in Rechargeable Nonaqueous Li–O₂ Batteries: Recent Progress and Perspective. *Advanced Energy Materials*, *8*(22), 1800348. <https://doi.org/10.1002/aenm.201800348>
- Mai, N. L., Hoang, N.-H., Do, H. T., Pilz, M., & Trinh, T. T. (2021). Elastic and thermodynamic properties of the major clinker phases of Portland cement: Insights from first principles calculations. *Construction and Building Materials*, *287*, 122873. <https://doi.org/10.1016/j.conbuildmat.2021.122873>

- Manthiram, A., Fu, Y., Chung, S.-H., Zu, C., & Su, Y.-S. (2014). Rechargeable Lithium–Sulfur Batteries. *Chemical Reviews*, *114*(23), 11751–11787. <https://doi.org/10.1021/cr500062v>
- Matz, O., & Calatayud, M. (2017). Periodic DFT Study of Rutile IrO₂: Surface Reactivity and Catechol Adsorption. *The Journal of Physical Chemistry C*, *121*(24), 13135–13143. <https://doi.org/10.1021/acs.jpcc.7b01990>
- Mehri, M., Mousavi-Khoshdel, S. M., & Molaei, M. (2021). First-principle calculations study of pristine, S-, O-, and P-doped g-C₃N₄ as ORR catalysts for Li-O₂ batteries. *Chemical Physics Letters*, *775*, 138614. <https://doi.org/10.1016/j.cplett.2021.138614>
- Momma, K., & Izumi, F. (2011). VESTA 3 for three-dimensional visualization of crystal, volumetric and morphology data. *Journal of Applied Crystallography*, *44*(6), 1272–1276. <https://doi.org/10.1107/S0021889811038970>
- Mondal, D., Paul, B. K., Das, S., Bhattacharya, D., Ghoshal, D., Nandy, P., Das, K., & Das, S. (2018). Synthesis and Property of Copper-Impregnated α -MnO₂ Semiconductor Quantum Dots. *Langmuir*, *34*(43), 12702–12712. <https://doi.org/10.1021/acs.langmuir.8b01745>
- Mu, X., Xia, C., Gao, B., Guo, S., Zhang, X., He, J., Wang, Y., Dong, H., He, P., & Zhou, H. (2021a). Two-dimensional Mo-based compounds for the Li-O₂ batteries: Catalytic performance and electronic structure studies. *Energy Storage Materials*, *41*, 650–655. <https://doi.org/10.1016/j.ensm.2021.06.036>
- Mu, X., Xia, C., Gao, B., Guo, S., Zhang, X., He, J., Wang, Y., Dong, H., He, P., & Zhou, H. (2021b). Two-dimensional Mo-based compounds for the Li-O₂ batteries: Catalytic performance and electronic structure studies. *Energy Storage Materials*, *41*, 650–655. <https://doi.org/10.1016/j.ensm.2021.06.036>
- Nie, H., Xu, C., Zhou, W., Wu, B., Li, X., Liu, T., & Zhang, H. (2016). Free-Standing Thin Webs of Activated Carbon Nanofibers by Electrospinning for Rechargeable Li–O₂ Batteries. *ACS Applied Materials & Interfaces*, *8*(3), 1937–1942. <https://doi.org/10.1021/acsami.5b10088>
- Nolan, M., Iwaszuk, A., Lucid, A. K., Carey, J. J., & Fronzi, M. (2016). Design of Novel Visible Light Active Photocatalyst Materials: Surface Modified TiO₂. *Advanced Materials*, *28*(27), 5425–5446. <https://doi.org/10.1002/adma.201504894>
- Nong, Z.-S., Zhu, J.-C., Cao, Y., Yang, X.-W., Lai, Z.-H., & Liu, Y. (2013). A first-principles study on the structural, elastic and electronic properties of the C14 Laves phase compounds TiX₂ (X=Cr, Mn, Fe). *Physica B: Condensed Matter*, *419*, 11–18. <https://doi.org/10.1016/j.physb.2013.03.012>
- Oura, K., Katayama, M., Zotov, A. V., Lifshits, V. G., & Saranin, A. A. (2003). *Surface Science*. Springer Berlin Heidelberg. <https://doi.org/10.1007/978-3-662-05179-5>

- Pandit, B., Rondiya, S. R., Dzade, N. Y., Shaikh, S. F., Kumar, N., Goda, E. S., Al-Kahtani, A. A., Mane, R. S., Mathur, S., & Salunkhe, R. R. (2021). High Stability and Long Cycle Life of Rechargeable Sodium-Ion Battery Using Manganese Oxide Cathode: A Combined Density Functional Theory (DFT) and Experimental Study. *ACS Applied Materials and Interfaces*, *13*(9), 11433–11441. <https://doi.org/10.1021/acsami.0c21081>
- Perdew, J. P., Burke, K., & Ernzerhof, M. (1996). Generalized Gradient Approximation Made Simple. *Physical Review Letters*, *77*(18), 3865–3868. <https://doi.org/10.1103/PhysRevLett.77.3865>
- Kronig, R. De L. and Penney W. G. (1931). Quantum mechanics of electrons in crystal lattices. Royal Society. <https://doi.org/10.1098/rspa.1931.0019>
- Rahman, Md. A., Wang, X., & Wen, C. (2013). High Energy Density Metal-Air Batteries: A Review. *Journal of The Electrochemical Society*, *160*(10), A1759–A1771. <https://doi.org/10.1149/2.062310jes>
- Ramesh, M., Nagaraja, H. S., Rao, M. P., Anandan, S., & Huang, N. M. (2016). Fabrication, characterization and catalytic activity of α -MnO₂ nanowires for dye degradation of reactive black 5. *Materials Letters*, *172*, 85–89. <https://doi.org/10.1016/j.matlet.2016.02.076>
- Rosenberger, A., Gao, Y., & Stanciu, L. (2015). Field-assisted sintering of Li_{1.3}Al_{0.3}Ti_{1.7}(PO₄)₃ solid-state electrolyte. *Solid State Ionics*, *278*, 217–221. <https://doi.org/10.1016/j.ssi.2015.06.012>
- Roszbach, A., Tietz, F., & Grieshammer, S. (2018). Structural and transport properties of lithium-conducting NASICON materials. *Journal of Power Sources*, *391*(January), 1–9. <https://doi.org/10.1016/j.jpowsour.2018.04.059>
- Sagotra, A. K., Chu, D., & Cazorla, C. (2019). Influence of lattice dynamics on lithium-ion conductivity: A first-principles study. *Physical Review Materials*, *3*(3), 035405. <https://doi.org/10.1103/PhysRevMaterials.3.035405>
- Shahrokhi, M., Raybaud, P., & Le Bahers, T. (2020). On the understanding of the optoelectronic properties of S-doped MoO₃ and O-doped MoS₂ bulk systems: a DFT perspective. *Journal of Materials Chemistry C*, *8*(26), 9064–9074. <https://doi.org/10.1039/D0TC02066D>
- Shi-Qi, Z., & Xiao-Qi, Z. (2002). Universality principle and the development of classical density functional theory. *Chinese Physics*, *11*(10), 1051–1059. <https://doi.org/10.1088/1009-1963/11/10/316>
- Sholl, D. S., & Steckel, J. A. (2009). *Density Functional Theory*. John Wiley & Sons, Inc. <https://doi.org/10.1002/9780470447710>
- Sohib, A., Irham, M. A., Karunawan, J., Santosa, S. P., Floweri, O., & Iskandar, F. (2023). Interface Analysis of LiCl as a Protective Layer of Li_{1.3}Al_{0.3}Ti_{1.7}(PO₄)₃ for Electrochemically Stabilized All-Solid-State Li-Metal Batteries. *ACS Applied Materials & Interfaces*, *15*(13), 16562–16570. <https://doi.org/10.1021/acsami.2c18852>
- Su, D., Ahn, H. J., & Wang, G. (2013). Hydrothermal synthesis of α -MnO₂ and β -MnO₂ nanorods as high capacity cathode materials for sodium ion batteries. *Journal of Materials Chemistry A*, *1*(15), 4845–4850. <https://doi.org/10.1039/c3ta00031a>

- Sun, J., Ruzsinszky, A., & Perdew, J. P. (2015). Strongly Constrained and Appropriately Normed Semilocal Density Functional. *Physical Review Letters*, *115*(3), 036402. <https://doi.org/10.1103/PhysRevLett.115.036402>
- Sunaina, Chand, P., Joshi, A., Lal, S., & Singh, V. (2021). Effect of hydrothermal temperature on structural, optical and electrochemical properties of α -MnO₂ nanostructures for supercapacitor application. *Chemical Physics Letters*, *777*, 138742. <https://doi.org/10.1016/j.cplett.2021.138742>
- Sung, M., Lee, G., & Kim, D. (2021). Kinetic insight into perovskite La_{0.8}Sr_{0.2}VO₃ nanofibers as an efficient electrocatalytic cathode for high-rate Li-O₂ batteries. *InfoMat*, *3*(11), 1295–1310. <https://doi.org/10.1002/inf2.12243>
- Tian, H. K., Jalem, R., Gao, B., Yamamoto, Y., Muto, S., Sakakura, M., Iriyama, Y., & Tateyama, Y. (2020). Electron and Ion Transfer across Interfaces of the NASICON-Type LATP Solid Electrolyte with Electrodes in All-Solid-State Batteries: A Density Functional Theory Study via an Explicit Interface Model. *ACS Applied Materials and Interfaces*, *12*(49), 54752–54762. <https://doi.org/10.1021/acsami.0c16463>
- Tian, X., Wang, T., Fan, L., Wang, Y., Lu, H., & Mu, Y. (2018). A DFT based method for calculating the surface energies of asymmetric MoP facets. *Applied Surface Science*, *427*, 357–362. <https://doi.org/10.1016/j.apsusc.2017.08.172>
- Tunega, D., Benco, L., Haberhauer, G., Gerzabek, M. H., & Lischka, H. (2002). Ab Initio Molecular Dynamics Study of Adsorption Sites on the (001) Surfaces of 1:1 Dioctahedral Clay Minerals. *The Journal of Physical Chemistry B*, *106*(44), 11515–11525. <https://doi.org/10.1021/jp026391g>
- Verma, C., Lgaz, H., Verma, D. K., Ebenso, E. E., Bahadur, I., & Quraishi, M. A. (2018). Molecular dynamics and Monte Carlo simulations as powerful tools for study of interfacial adsorption behavior of corrosion inhibitors in aqueous phase: A review. *Journal of Molecular Liquids*, *260*, 99–120. <https://doi.org/10.1016/j.molliq.2018.03.045>
- Wang, D., Mu, X., He, P., & Zhou, H. (2019). Materials for advanced Li-O₂ batteries: Explorations, challenges and prospects. *Materials Today*, *26*, 87–99. <https://doi.org/10.1016/j.mattod.2019.01.016>
- Wang, G., Li, Y., Shi, L., Qian, R., & Wen, Z. (2020). Realizing the growth of nano-network Li₂O₂ film on defect-rich holey Co₉S₈ nanosheets for Li-O₂ battery. *Chemical Engineering Journal*, *396*, 125228. <https://doi.org/10.1016/j.cej.2020.125228>
- Wang, J., Ma, L., Xu, J., Xu, Y., Sun, K., & Peng, Z. (2021). Oxygen electrochemistry in Li-O₂ batteries probed by in situ surface-enhanced Raman spectroscopy. *SusMat*, *1*(3), 345–358. <https://doi.org/10.1002/sus2.24>
- Wu, F., & Yushin, G. (2017). Conversion cathodes for rechargeable lithium and lithium-ion batteries. *Energy & Environmental Science*, *10*(2), 435–459. <https://doi.org/10.1039/C6EE02326F>

- Xia, C., Jia, Y., Tao, M., & Zhang, Q. (2013). Tuning the band gap of hematite α -Fe₂O₃ by sulfur doping. *Physics Letters A*, 377(31–33), 1943–1947. <https://doi.org/10.1016/j.physleta.2013.05.026>
- Xu, C., Gallant, B. M., Wunderlich, P. U., Lohmann, T., & Greer, J. R. (2015). Three-Dimensional Au Microlattices as Positive Electrodes for Li–O₂ Batteries. *ACS Nano*, 9(6), 5876–5883. <https://doi.org/10.1021/acsnano.5b00443>
- Yang, J., Zhang, Q., Wang, Z., Wang, Z., Kang, L., Qi, M., Chen, M., Liu, W., Gong, W., Lu, W., Shum, P. P., & Wei, L. (2020). Rational Construction of Self-Standing Sulfur-Doped Fe₂O₃ Anodes with Promoted Energy Storage Capability for Wearable Aqueous Rechargeable NiCo-Fe Batteries. *Advanced Energy Materials*, 10(33), 2001064. <https://doi.org/10.1002/aenm.202001064>
- Yang, Y., Bremner, S., Menictas, C., & Kay, M. (2018). Battery energy storage system size determination in renewable energy systems: A review. *Renewable and Sustainable Energy Reviews*, 91, 109–125. <https://doi.org/10.1016/j.rser.2018.03.047>
- Ye, Z., Jiang, Y., Li, L., Wu, F., & Chen, R. (2021). Rational Design of MOF-Based Materials for Next-Generation Rechargeable Batteries. *Nano-Micro Letters*, 13(1), 203. <https://doi.org/10.1007/s40820-021-00726-z>
- Yi, X., Liu, X., Pan, W., Qin, B., Fang, J., Jiang, K., Deng, S., Meng, Y., Leung, D. Y. C., & Wen, Z. (2022). Evolution of Discharge Products on Carbon Nanotube Cathodes in Li–O₂ Batteries Unraveled by Molecular Dynamics and Density Functional Theory. *ACS Catalysis*, 12(9), 5048–5059. <https://doi.org/10.1021/acscatal.2c00409>
- Young, M. J., Holder, A. M., George, S. M., & Musgrave, C. B. (2015). Charge Storage in Cation Incorporated α -MnO₂. *Chemistry of Materials*, 27(4), 1172–1180. <https://doi.org/10.1021/cm503544e>
- Yu, Z. L., Leung, K. K., Yu, H.-Z., & Bizzotto, D. (2017). A non-linear harmonic analysis of potential induced fluorescence modulation of a DNA self assembled monolayer. *Electrochimica Acta*, 245, 386–394. <https://doi.org/10.1016/j.electacta.2017.05.129>
- Zhan, Y., Luo, S., Feng, J., Zhang, L., Liu, X., Qing Wang, & Zhang, Y. (2021). Improved electrocatalytic activity of hexagonal prisms Fe₃O₄ derived from metal-organic framework by covering dendritic-shaped carbon layer in Li–O₂ battery. *Composites Part B: Engineering*, 226, 109354. <https://doi.org/10.1016/j.compositesb.2021.109354>
- Zhang, B., Lin, Z., Dong, H., Wang, L. W., & Pan, F. (2020). Revealing cooperative Li-ion migration in Li_{1+x}: XAl_xTi_{2-x}(PO₄)₃ solid state electrolytes with high Al doping. *Journal of Materials Chemistry A*, 8(1), 342–348. <https://doi.org/10.1039/c9ta09770h>
- Zhang, J., Zhao, Y., Zhao, X., Liu, Z., & Chen, W. (2014). Porous Perovskite LaNiO₃ Nanocubes as Cathode Catalysts for Li-O₂ Batteries with Low Charge Potential. *Scientific Reports*, 4(1), 6005. <https://doi.org/10.1038/srep06005>

- Zhao, Y., Cheng, W., Wu, J., Hu, Z., Liu, F., Wang, L., & Peng, H. (2023). Recent advances in charge mechanism of noble metal-based cathodes for Li-O₂ batteries. *Chinese Chemical Letters*, 34(2), 107413. <https://doi.org/10.1016/j.ccllet.2022.04.011>
- Zhao, Y., Hang, Y., Zhang, Y., Wang, Z., Yao, Y., He, X., Zhang, C., & Zhang, D. (2017a). Strontium-doped perovskite oxide La_{1-x}Sr_xMnO₃ (x = 0, 0.2, 0.6) as a highly efficient electrocatalyst for nonaqueous Li-O₂ batteries. *Electrochimica Acta*, 232, 296–302. <https://doi.org/10.1016/j.electacta.2017.02.155>
- Zhao, Y., Hang, Y., Zhang, Y., Wang, Z., Yao, Y., He, X., Zhang, C., & Zhang, D. (2017b). Strontium-doped perovskite oxide La_{1-x}Sr_xMnO₃ (x = 0, 0.2, 0.6) as a highly efficient electrocatalyst for nonaqueous Li-O₂ batteries. *Electrochimica Acta*, 232, 296–302. <https://doi.org/10.1016/j.electacta.2017.02.155>
- Zhao, Y.-H., Su, H.-Y., Sun, K., Liu, J., & Li, W.-X. (2012). Structural and electronic properties of cobalt carbide Co₂C and its surface stability: Density functional theory study. *Surface Science*, 606(5–6), 598–604. <https://doi.org/10.1016/j.susc.2011.11.025>
- Zheng, F., Dong, H., Ji, Y., & Li, Y. (2019). Computational study on catalytic performance of BC₃ and NC₃ nanosheets as cathode electrocatalysts for nonaqueous Li–O₂ batteries. *Journal of Power Sources*, 436, 226845. <https://doi.org/10.1016/j.jpowsour.2019.226845>
- Zheng, Y., Song, K., Jung, J., Li, C., Heo, Y.-U., Park, M.-S., Cho, M., Kang, Y.-M., & Cho, K. (2015). Critical Descriptor for the Rational Design of Oxide-Based Catalysts in Rechargeable Li–O₂ Batteries: Surface Oxygen Density. *Chemistry of Materials*, 27(9), 3243–3249. <https://doi.org/10.1021/acs.chemmater.5b00056>
- Zhou, Y., Yin, K., Gu, Q., Tao, L., Li, Y., Tan, H., Zhou, J., Zhang, W., Li, H., & Guo, S. (2021). Lewis-Acidic PtIr Multipods Enable High-Performance Li–O₂ Batteries. *Angewandte Chemie International Edition*, 60(51), 26592–26598. <https://doi.org/10.1002/anie.202114067>
- Zhu, J., Dai, L., Yu, Y., Cao, J., & Wang, L. (2015). A direct electrochemical route from oxides to TiMn₂ hydrogen storage alloy. *Chinese Journal of Chemical Engineering*, 23(11), 1865–1870. <https://doi.org/10.1016/j.cjche.2015.08.033>
- Zhu, J., Ren, X., Liu, J., Zhang, W., & Wen, Z. (2015). Unraveling the Catalytic Mechanism of Co₃O₄ for the Oxygen Evolution Reaction in a Li–O₂ Battery. *ACS Catalysis*, 5(1), 73–81. <https://doi.org/10.1021/cs5014442>
- Zuo, E., Dou, X., Chen, Y., Zhu, W., Jiang, G., Mao, A., & Du, J. (2021). Electronic work function, surface energy and electronic properties of binary Mg-Y and Mg-Al alloys: A DFT study. *Surface Science*, 712, 121880. <https://doi.org/10.1016/j.susc.2021.121880>

CURRICULUM VITAE

Name Surname : Doaa Aasef Ahmed AHMED

EDUCATION:

- **Undergraduate** : 2014, Baghdad University, Collage of Science For Women, Physics Department
- **Graduate** : 2019, Sakarya University, Institute of Nature science, Physics

PROFESSIONAL EXPERIENCE AND AWARDS:

- She worked as a YÖS teacher at YediRenk corse between 2019-2021.
- She worked as a proje asistanı at Sakarya University/ Research, Development and Application Center (SARGEM) between 2019-2022.
- She is still working as a Visiting scientist at Hamburg University of Technology/ Advanced Ceramic Institute scince 2022.

PUBLICATIONS, PRESENTATIONS AND PATENTS ON THE THESIS:

- Ahmed, D. A., Kızılaslan, A., Çelik, M., Vonbun-Feldbauer, G. B., & Cetinkaya, T. (2023). Sulfur-doped $\text{Li}_{1.3}\text{Al}_{0.3}\text{Ti}_{1.7}(\text{PO}_4)_3$ as a solid electrolyte for all-solid-state batteries: First-principles calculations. *Electrochimica Acta*, 463, 142872. <https://doi.org/10.1016/j.electacta.2023.142872>.
- International Symposium on Materials for Energy Storage and Conversion mESC-IS Lithium and Oxygen Adsor2022.n at the α - MnO_2 surface (as free carbon cathode for Li-O₂ battery), 2022.

OTHER PUBLICATIONS, PRESENTATIONS AND PATENTS::

- Ahmed, D. A. A., Bağcı, S., Karaca, E., & Tütüncü, H. M. (2018). Elastic properties of ABF_3 (A:Ag,K and B:Mg, Zn) perovskites. 020035. <https://doi.org/10.1063/1.5078907>.